

A NON-AUTONOMOUS BURSTING
MODEL FOR NEURONS

by

Joe Jean-Marc Latulippe

A dissertation submitted in partial fulfillment
of the requirements for the degree

of

Doctor of Philosophy

in

Mathematics

MONTANA STATE UNIVERSITY
Bozeman, Montana

April 2007

©COPYRIGHT

by

Joe Jean-Marc Latulippe

2007

All Rights Reserved

APPROVAL

of a dissertation submitted by

Joe Jean-Marc Latulippe

This dissertation has been read by each member of the dissertation committee and has been found to be satisfactory regarding content, English usage, format, citations, bibliographic style, and consistency, and is ready for submission to the Division of Graduate Education.

Dr. Mark Pernarowski

Approved for the Department of Mathematics

Dr. Kenneth L. Bowers

Approved for the Division of Graduate Education

Dr. Carl A. Fox

STATEMENT OF PERMISSION TO USE

In presenting this dissertation in partial fulfillment of the requirements for a doctoral degree at Montana State University, I agree that the Library shall make it available to borrowers under rules of the Library. I further agree that copying of this dissertation is allowable only for scholarly purposes, consistent with "fair use" as prescribed in the U. S. Copyright Law. Requests for extensive copying or reproduction of this dissertation should be referred to Bell & Howell Information and Learning, 300 North Zeeb Road, Ann Arbor, Michigan 48106, to whom I have granted "the exclusive right to reproduce and distribute my dissertation in and from microform along with the non-exclusive right to reproduce and distribute my abstract in any format in whole or in part."

Joe Jean-Marc Latulippe

April 2007

TABLE OF CONTENTS

LIST OF TABLES	vi
LIST OF FIGURES	vii
1. INTRODUCTION	1
Physiology	6
Existing Models	10
Single Cell Models, Bursting and PIR.....	10
Network Models	17
Outline of Dissertation	21
2. MODEL DEVELOPMENT	25
Synaptic Model.....	25
Plasticity	27
Synaptic Model Formulation.....	30
Single Cell Model	39
3. SUBSYSTEM DERIVATION AND DEFINITION	44
Fast-Subsystem	45
Slow-Subsystem	49
Averaged-Fast-Subsystem	51
Rapid Transitions, Basin of Attraction	54
4. CONSTANT CURRENT PULSES	68
<i>On</i> Response.....	70
<i>Off</i> Response	79
<i>Mixed</i> Response	84
5. MONOTONE SLOWLY DECREASING INPUTS	97
Introduction to <i>Mixed</i> Response	97
Numerical Example	98
Class of Inputs	102
Augmentation of (FULL)	106
Averaged-Fast-Subsystem (AFSa)	109
Slow-Subsystem (SSa)	118
PIR Region.....	120
Trapping Regions	124
Map Composition	138

6. CONCLUSIONS AND SUMMARY	151
Summary	151
Applications	153
Numerical Results	155
Future Work	160
REFERENCES CITED.....	166

LIST OF TABLES

Table	Page
1. A description of the possible net synaptic current responses given a presynaptic input (or visual stimulus). In the second column the bar under each shape represents the duration of a presynaptic input (or visual stimulus).....	38
2. Definition of points needed to describe <i>On</i> response cycles.....	70
3. A description of the possible responses given an <i>On</i> stimulus	78
4. A description of the sufficient conditions on the duration T_2 needed to guarantee a rebound burst (PIR) given an <i>On</i> response resulting from an amplitude \bar{I}_+ and duration T_1	94

LIST OF FIGURES

Figure	Page
1. Shows typical <i>On</i> and <i>Off</i> responses in a retinal ganglion cell. In each figure, the dark spot represents the location(s) of the stimulus. In the right column, the spike train of the cell is shown over the time course of the stimulus amplitude. a) illustrates a typical <i>On</i> response; b) shows a typical <i>Off</i> response; c) shows the <i>Mixed</i> response of a ganglion cell when given two simultaneous stimuli [51]. Here the <i>On</i> part of the receptive field (indicated by + signs) is surrounded by an <i>Off</i> component (indicated by - signs). Since the <i>On</i> part of the receptive field is surrounded by the <i>Off</i> part, this receptive field is often referred to as an “On-Center” receptive field. Some ganglia have “Off-Center” fields where this orientation is reversed.....	4
2. Shows typical <i>On</i> and <i>Off</i> responses for simple cells in the primary visual cortex. In each figure, the dark bar represents the location and shape of the stimulus. In the right column, the spike train of the cell is shown over the time course of the stimulus amplitude. a) illustrates a typical <i>On</i> response; b) shows a typical <i>Off</i> response; c) illustrates a diminished <i>On</i> response when the stimulus bar covers both <i>Plus</i> and <i>Minus</i> regions. The angle θ shown in c) is the orientation angle of the stimulus. In a) the angle θ is said to be in orientation preference for this particular type of receptive field whereas in c) θ is not in orientation preference.....	9
3. Some examples of oscillatory behaviors (including three types of Bursting) with their classifications given	16
4. Shows the effects of synaptic facilitation and depression on the postsynaptic potential as a function of time (adapted from Figure 12.2 in [55]). Each surge in membrane potential corresponds to the effect of a presynaptic spike (4 spikes). Illustrated in a) is the increase in amplitude after each spike (facilitation). Illustrated in b) is the decrease in amplitude after each spike (depression).....	29
5. Shows a response which adapts to a constant current input. This adaptation is a decrease in spike rate as a function of time. The voltage of the membrane potential u is plotted as a function of time t over the constant current pulse.....	30

6. Shows the solution to the linearized synaptic model with a spike train input $i(t)$ (with 15 spikes). In each figure an interpolation (2.10) is superimposed on the true solution (2.9). Two different parameter sets $(\alpha, \lambda, \Delta t)$ were used. a) shows a synaptic channel which is “slow” to activate and “slow” to inactivate corresponding to parameters (1.2,6,0.3). This behavior will be referred to as “slow” On and “slow” Off. b) shows a synaptic channel which is “fast” to activate and “fast” to inactivate corresponding to parameters (0.3,0.8,0.3). This behavior will be referred to as “fast” On and “fast” Off..... 34
7. The k -dependent functions for facilitation and depression, shown in a) and b) respectively 35
8. Shows the solution to the linearized synaptic model with an k -dependent amplitude function $\alpha(k)$ to incorporate the effects of synaptic facilitation and depression. In a) the solution to (2.12) is shown with $\alpha(k) = \arctan(k/3)$ (facilitation), and the parameter set $(\alpha, \lambda, \Delta t)=(1.25, 3, 0.3)$. In b) the solution to (2.12) is shown with $\alpha(k) = -\arctan(k/3) + \pi/2$ (depression), and the parameter set (1.25, 2, 0.3) 35
9. Shows typical *On* and *Off* responses in the model (FULL) with the constant current stimuli $I(t)$ superimposed on each figure. The (FS) parameter set $\lambda_f = (a, \eta, \mu)$ was chosen as $\lambda_f = (0.25, 0.75, 1.5)$ with a current amplitude $\bar{I} = +0.8$ and $\bar{I} = -1.8$ for the *On* and *Off* responses, respectively. In both, the slow parameters $\lambda_s = (\alpha, \beta) = (-1.5, 4)$ and $\epsilon = 0.0025$. In each figure, $t_0 = 500$ and $T = 150$. The numerical traces in this figure were generated using XPPAUT [23]..... 42
10. Fast-subsystem bifurcation diagrams for (3.1)-(3.2). Labeled are the Hopf point γ_{hb} , the homoclinic value γ_{hc} , the right most saddle node bifurcation value γ_+ , and the left most saddle node bifurcation value γ_- . In figure a) the fast parameter set was chosen as $\lambda_f = (a, \eta, \mu) = (0.25, 0.75, 1.5)$. Notice that for this choice of λ_f , (FS) has a region of bistability for $\gamma \in (\gamma_-, \gamma_{hc})$. In figure b) the fast parameter set was chosen as $\lambda_f = (a, \eta, \mu) = (0.25, 0.9, 1.5)$. For this choice of fast parameters, the bifurcation structure does not have a region of bistability 47
11. Fast-subsystem bifurcation diagram for (3.1)-(3.2) with fast parameter set $(a, \eta, \mu) = (0.25, 0.75, 1.5)$. Superimposed on (FS) are the $\dot{\gamma} = 0$ line and a bursting solution. In this figure, the slow parameter set was chosen as $(\alpha, \beta) = (-1, 4)$ 52

- 12. This figure shows $\hat{u}(\gamma)$ for $\gamma \in (\gamma_{hb}, \gamma_{hc})$. Upper and lower branch equilibria S_L , and S_m are also superimposed for reference..... 54

- 13. Shows the stable manifold $\mathcal{W}_S(\bar{u}_m(1.5))$ for two different ranges of u . Illustrated in a) is the phase portrait for (3.28)-(3.29) over a larger nonphysical range of u and v . b) illustrates the stable manifolds $\mathcal{W}_S^+(\bar{u}_m)$ and $\mathcal{W}_S^-(\bar{u}_m)$ for $\gamma \in (\gamma_-, \gamma_{hc})$ for a more realistic modeling range. Also illustrated in b) is the unstable manifold $\mathcal{W}_U(\bar{u}_m(1.5))$ and the periodic orbit (dashed curves). Whenever an initial condition, (u_0, v_0) , for (3.28)-(3.29) is chosen to lie between $\mathcal{W}_S^+(\bar{u}_m)$ and $\mathcal{W}_S^-(\bar{u}_m)$, the trajectories will be attracted to the periodic orbits of the Liénard system. Labeled in these figures are the u -values \bar{u}_l , \bar{u}_m , and \bar{u}_u corresponding to the lower (stable), middle (saddle), and upper (unstable) equilibria of (FS), respectively 58

- 14. This figure shows the two curves $U_{S_l}(\gamma)$ and $U_{S_m}(\gamma)$ for $\gamma_- < \gamma < \gamma_{hc}$. The set $B = \{(u, \gamma) : U_{S_l}(\gamma) < u < U_{S_m}(\gamma), \gamma \in (\gamma_-, \gamma_{hc})\}$ is also labeled 62

- 15. This figure shows four different trajectories of (FULL) (thick lines) when four different initial conditions are chosen. In each case, the dynamics of (FULL) are different and are a result of the location of each initial condition with respect to the basin of attraction of Ω_p in (FS). In each figure, the (FS) bifurcation structure (thin lines) has been included as a reference as well as $\dot{\gamma} = 0$ (dash-dot lines). Also illustrated in each figure is the region B which represents the range of u (for each γ in the bistable range) where \mathcal{B}_p plays a role in the trajectories of (FS) (cf. Figure 14). For the initial condition $(u_0, w_0, \gamma_0) = (-2.5, f(-2.5) - 1.25, 1.25)$, a) shows that the trajectory of (FULL) is attracted to S_L since $(u_0, w_0) = (-2.5, f(-2.5) - 1.25) \in \mathcal{B}_L$. For the initial condition $(u_0, w_0, \gamma_0) = (-3.5, f(-3.5) - 1.25, 1.25)$, b) shows that the trajectory of (FULL) is attracted to Ω_p since $(u_0, w_0) = (-3.5, f(-3.5) - 1.25) \in \mathcal{B}_P$. In c), an initial condition, which has a u_0 -value that lies below U_{S_l} , is used. Even though the trajectory of (FULL) is attracted to S_L when the initial condition $(-4.75, f(-4.5) - 1.25, 1.25)$ is used, it first travels around Ω_p before returning to S_L . Figure d) shows the trajectories of (FULL) when an initial condition that has $\bar{u}_m < u_0 < u_{S_u}$ is used. This figure shows that the trajectory of (FULL) is attracted to Ω_p when the initial condition $(1, f(1) - 1.25, 1.25)$ is used 65

16. Shows an *On* response solution of (FULL) projected onto the fast subsystem diagrams for $\bar{I} = 0$ (thin) and $\bar{I} = 0.8$ (thick). Also shown in this figure is the z -nullcline of (FULL). Diagram b) is a closeup of a) showing relevant transition points and the leading-order times at which transitions occur. Also shown is the new equilibria $\bar{X}(\bar{I})$ of (FULL) which here is close to the saddle node P_- 72
17. This figure shows the response of (FULL) for the stimulus amplitude value $\bar{I} = 1.8$ and various durations. In each figure the black line represents the time duration of the input. In a) $T = 10$ is chosen smaller than T_A , and the response continues to spike after the stimulus is turned off. For a duration value $T = 50 < T_A$, b) shows that the *On* response will occur during the entire duration of the stimulus. Both responses in a) and b) show that for the values (\bar{I}, T) corresponding to region (b) in Figure 19 the *On* response at least occurs for the entire duration of the stimulus. Figure c) shows that the (PSS) found in a) may recur if the duration is large enough. By choosing $T = 268 > T_A$ the stimulus is turned off before the solution goes through the second bursting cycle creating the post stimulus spiking. For the duration $T = 400 > T_A$, d) shows that multiple bursts may occur. Also notice that in d), the cycle has two silent phase durations. The first duration, T_{SP_1} , occurs between the two bursting cycles, and the other T_{SP_2} is the duration between the second burst and the time the pulse is turned off 77
18. Shows an *Off* response solution of (FULL) projected onto the fast subsystem diagrams for $\bar{I} = 0$ (thin) and $\bar{I} = -1.8$ (thick). Also shown in this figure is the z -nullcline of (FULL). Diagram b) shows the relevant transition points and the leading-order time at which these transitions occur 81
19. A categorization for the different responses based on input duration T and amplitude \bar{I} . For negative values of \bar{I} , the threshold values \bar{I}_{lb} , and \bar{I}^- are labeled. The minimum duration T_S for an *Off* response is plotted to provide the lower bound for the region (a) where an *Off* response occurs (PIR). For positive values of \bar{I} , the threshold values \bar{I}^+ , \bar{I}_m , and \bar{I}_{ub} have been plotted. The threshold duration T_A for the *On* responses has been plotted to create the regions (b), (c), and (d). In region (b), spiking will occur at least during the entire duration of the input. In region (c), the spiking will terminate before the input is turned off. In region (d), the response will burst, but depending on the duration T , it may go through more than one bursting cycle 83

20. This figure shows that a rebound burst can occur for amplitude and duration values not discussed in Figure 19. In this figure $\bar{I} = -55$, and $T = 10$. The time duration of the input is given as the black line (thick). Even though a rebound burst occurs, this type of input amplitude is unrealistic when modeling visual neurons. Notice that the resulting initial spike also has an unrealistic amplitude value. Nevertheless, this illustrates that the basins of attraction can play an important role when describing the dynamics of (FULL)..... 85
21. This figure shows a *Mixed* response of (FULL) when given a constant *On* and *Off* current pulse. For the response illustrated in this figure, $\bar{I}_+ = 0.8$, $\bar{I}_- = -1.8$, $T_1 = 50$, and $T_2 = 200$ 86
22. Shows a *Mixed* response solution of (FULL) projected onto the fast-subsystem diagrams for $\bar{I} = 0$ (thin), $\bar{I} = 0.8$ (thick, right most), and $\bar{I} = -1.8$ (thick, left most). Diagram a) shows the relevant transition points for the *On* part of the solution. In a) a rapid transition from the point M_0 to $\Omega_p(0.8)$ occurs at $t = t_0^+$. The solution then travels along the active phase until $t = (t_0 + T_1)^+$, where a rapid transition to the point M_1 occurs. In b) the continuation of the solution illustrated in a) is shown. The solution travels along $S_L(-1.8)$ from M_1 to M_2 . At $t = t_0 + T_1 + T_2$ the stimulus is turned off and a transition from M_2 to $\Omega_P(0)$ occurs. The solution will then travel right and will exit at the homoclinic point where a transition to the point M_3 occurs. This finishes the rebound burst, and the solution will travel along $S_L(0)$ until it reaches the equilibria at M_0 88
23. This figure shows the duration T_{AM} for each \bar{I}_+ in the threshold range. This curve gives the minimum duration for the *On* part that will guarantee $\bar{z}(\bar{I}_+) < z(t_0 + T_1) < z_{hc}(\bar{I}_+)$. Notice that this curve lies below the curve T_A for all \bar{I}_+ . For any pair (\bar{I}_+, T_1) in the regions (c), (e), and (g), lower and upper bound curves for the minimum duration T_{SO} needed to guarantee a rebound burst given an *On* part are given by (4.15), and (4.16) respectively. For any pair (\bar{I}_+, T_1) in the region (f), the upper bound curve for the minimum duration T_{SO} needed to guarantee a rebound burst given an *On* part is given by (4.15) 91

24. Shows the appropriate lower and upper bound curves T_{SX} and T_{SH} for three different values of \bar{I}_+ . In a) the curves were generated for the value $\bar{I}_+ = 0.5$ and $T_{AM} < T_1$. In b) the curves were generated for the value $\bar{I}_+ = 0.8$ and $T_{AM} < T_1$. In c) the curves were generated for the value $\bar{I}_+ = 1.5$. In each of the figures a), b), the bounds are valid only when $T_{AM} < T_1$. In c) these bounds are valid only when $T_{AM} < T_1 < T_A$. In each a), b), and c) the minimum duration for an *Off* response must lie between the two curves. Figure d) shows the upper bound curve T_{SX} when $\bar{I}_+ = 1.5$ and $T_1 < T_{AM}$ 96
25. In this figure, a) shows the general behavior for a “Fast” *On* “Fast” *Off* synaptic input as in (5.1). b) shows the “Slow” *On* “Fast” *Off* behavior described in (5.2). c) shows the sum of the inputs from a) and b) $I(t) = I_+(t) + I_-(t)$ 99
26. This figure shows that each response in Figure 1 can be reproduced using (FULL). In each figure the thick line represents the net synaptic input. In a), an *On* response is shown. By assuming a “slow” to activate and “fast” to inactivate inhibitory synaptic input, b) shows that (FULL) can reproduce the PIR response. In c), the *Mixed* response is reproduced using a synaptic input which is a combination of the excitatory input from a) and the inhibitory input from b)..... 100
27. Two examples which illustrate the types of generic inputs that belong to the class \mathbb{C} 104
28. This figure shows a “generic applicable” input which is the solution to the initial value problem given by equation (5.11). In this case $\bar{I}_{lb} < I_{min} < I_0 < \bar{I}_m$. Also illustrated are the times $t = t_0$ and $t = t_0 + T$ along with the thresholds $I = \bar{I}_{lb}$ and $I = \bar{I}_m$ (as the dash-dot lines) 107
29. This figure shows a caricature of a typical trajectory of (FULLa) projected in the (z, I) -plane. The map $\hat{\Phi}$ describes an active phase transition from an initial point \mathbf{X}_0 to the terminating point \mathbf{X}_{hc} 114

30. Figure a) shows the active phase trajectory of (FULLa) projected on the (z, I) -plane (oscillatory curve) and the trajectory generated by (AFSa) (smooth curve) when $H_2(I) = -\tilde{a}I + \tilde{b}$. Both figures show the same trajectories on two different intervals. In a), $\epsilon = 0.0025$ with $\tilde{a} = 1$, and $\tilde{b} = 1$. Figure b) shows the active phase trajectory of (FULLa) projected on the (z, I) -plane and the trajectory generated by (AFSa) when $\epsilon = 0.0005$ (with $\tilde{a} = 1$, and $\tilde{b} = 1$) is used. Notice that when a smaller ϵ is used, (AFSa) is a “very good” approximation of the projected active phase trajectory 116
31. This figure shows the active phase duration \bar{T}_a as a function of the initial value I_0 . The duration was computed for two parameter sets: $(\tilde{a}, \tilde{b})_1 = (1, -1.3)$ and $(\tilde{a}, \tilde{b})_2 = (5, -6.5)$. Since the value \tilde{a} corresponds to the decay rate of the input, notice that when \tilde{a} is smaller, the active phase duration is longer 118
32. This figure shows the z -null curve for (SSa) along with the Γ_- and the Γ_{hc} curves. Also shown is the $z_- = 1$ curve (vertical curve) and the threshold values; $\bar{I}_m, \bar{I}^+, \bar{I}^-, I_{min}$, and \bar{I}_{lb} . Also labeled is the position of the equilibria of (SSa). These curves will play an important role when describing the trajectories of (SSa) 121
33. This figure shows a sketch of the region Ω_{PIR} defined by $z_{hb}(0) < z < z_-(0)$ and $\bar{I}_{lb} < I < \bar{I}^-$. Also illustrated in this figure are the z -nullcline for (SSa) along with the Γ_- curve. Three different paths are labeled (a), (b), and (c) with the terminal point labeled by P_a, P_b , and P_c respectively. Of these, only P_c will exhibit PIR. The exit set Ω_e is also illustrated 123
34. This figure shows a sketch of the trapping region Ω_{SSa} . Shown as the thin striped box is the exit set Ω_e . The small arrows show the direction field along each edge of Ω_{SSa} . Note that no trajectories can cross the I_{min} line at the bottom. Also shown in this figure is a trajectory $\tilde{\gamma}_X$ with starting and terminating points \mathbf{X}_s and \mathbf{X}_T , respectively. The point P^- is also shown where the trajectory crosses the threshold value- \bar{I}^- 126
35. This figure shows a sketch of the trapping region Ω_{Ts} for two cases. In a), $I_{min} < I_\gamma$, and in b), $I_\gamma < I_{min}$. Shown in each figure as the thin striped box is the exit set Ω_e and the Γ_{hc} curve. Initial conditions for the silent phase portion of the *Mixed* response will lie on Γ_{hc} in both cases. For the parameter pairs $(\tilde{a}, \tilde{b})_1$ and $(\tilde{a}, \tilde{b})_2$ used in Figure 31, case a) applies..... 128

- 36. This figure shows a sketch of the trapping region Ω_{T_s} (for the case in Figure 35a)) with the normal vector and the appropriate direction field along Γ_{hc} 130
- 37. This figure shows the region $\Omega_{(\tilde{a}, \tilde{b})}$ 133
- 38. This figure shows the silent phase trajectory of (FULLa) projected on the (z, I) -plane and the trajectory generated by (SSa) (curve which starts at $\mathbf{X}_s \in \Gamma_{hc}$) when $H_2(I) = -\tilde{a}I + \tilde{b}$. In both figures $\epsilon = 0.0005$ was chosen to show how well (SSa) approximates the projection of (FULLa) in the silent phase in the limit $\epsilon \rightarrow 0^+$. Figure a) shows a trajectory when $(\tilde{a}, \tilde{b})_1 = (1, -1.3)$ is used. Notice that this trajectory satisfies the conditions of Lemma 5 and the trajectory does not cross Γ_{hc} . Figure b) shows the trajectory when $(\tilde{a}, \tilde{b})_2 = (5, -6.5)$ is used. When this pair is used, the conditions of Lemma 5 are not satisfied and the trajectory proceeds below Γ_{hc} . Also notice that in this case, a transition to Ω_{PIR} still occurs due to Lemma 4. In both cases the point $\mathbf{X}_T \in \Omega_{PIR}$ (not labeled in figure)..... 134
- 39. This figure shows the minimum duration \bar{T}_s needed in the silent phase to guarantee PIR as a function of the initial value $z_s \in \Gamma_{hc}$ for the two parameter pairs $(\tilde{a}, \tilde{b})_1$ and $(\tilde{a}, \tilde{b})_2$ 135
- 40. This figure shows the *Off* response silent phase trajectory of (SSa) for two different pairs (\tilde{a}, \tilde{b}) . In both figures the initial condition is $\mathbf{X}_s = (\bar{z}(0), 0)$. In *a*), $(\tilde{a}, \tilde{b})_1 = (1, -1.3)$ and in *b*) $(\tilde{a}, \tilde{b})_2 = (5, -6.5)$. Notice that in both figures, the duration \bar{T}_s has been given, and that a PIR response is guaranteed to occur since the point $\mathbf{X}_T \in \Omega_{PIR}$ 136
- 41. This figure shows two *Off* responses for two different (\tilde{a}, \tilde{b}) -pairs. In each, the initial condition was chosen to be $(z_0, I_0) = (\bar{z}(0), 0)$. In *a*), $(\tilde{a}, \tilde{b})_1 = (1, -1.3)$ are used with a duration T large enough to elicit PIR. Figure *b*) shows the same experiment for $(\tilde{a}, \tilde{b})_2 = (5, -6.5)$. 138
- 42. This figure shows the *On* burst cycle in the *Mixed* response along with the silent phase transition 141
- 43. This figure shows the PIR burst cycle in the *Mixed* response 142
- 44. This figure shows the dependence of the response on the input duration. In *a*), $(\tilde{a}, \tilde{b})_1 = (1, -1.3)$ are used with an insufficient duration T to elicit PIR. Figure *b*) shows the same simulation for $(\tilde{a}, \tilde{b})_2 = (5, -6.5)$.. 144

45. This figure shows *Mixed* responses for two different (\tilde{a}, \tilde{b}) -pairs. In *a*), $(\tilde{a}, \tilde{b})_1 = (1, -1.3)$ are used with a duration T large enough to elicit PIR. Figure *b*) shows the same experiment for $(\tilde{a}, \tilde{b})_2 = (5, -6.5)$ 145
46. This figure shows the trajectory of (FULLa) projected on the (z, I) -plane and the trajectory generated by the subsystems (AFSa) and (SSa) when $H_2(I) = -\tilde{a}I + \tilde{b}$. In both figures $\epsilon = 0.0025$ and as a result a visual difference between the projected solution and the leading order solutions exists. Figure *a*) shows a trajectory when $(\tilde{a}, \tilde{b})_1 = (1, -1.3)$ is used. Notice that this trajectory satisfies the conditions of Lemma 5 and the trajectory does not cross Γ_{hc} . Figure *b*) shows the trajectory when $(\tilde{a}, \tilde{b})_2 = (5, -6.5)$ is used. When this pair is used, the conditions of Lemma 5 are not satisfied and the trajectory proceeds below Γ_{hc} . In both cases the duration $T > \bar{T}_m$ and the point $\mathbf{X}_T \in \Omega_{PIR}$, and as such a *Mixed* response is produced..... 147
47. This figure shows the role of \tilde{a} on both the active phase and silent phase durations. In *a*), the active phase duration \bar{T}_a plotted as a function of \tilde{a} , for $\tilde{a} \in (0.1, 10)$. In *b*) the silent phase duration \bar{T}_s is plotted against \tilde{a} . Notice that when \tilde{a} is smaller, both the active phase and the silent phase durations are longer 148
48. This figure shows two different delayed *On* responses for synaptic inputs with slowly activating excitatory inputs. In *a*) a single burst is shown while *b*) shows multiple bursts 157
49. This figure shows the *Off* response silent phase trajectory of (SSa) for two different pairs (\tilde{a}, \tilde{b}) . In both figures the initial condition is $\mathbf{X}_s = (\bar{z}(0), 0)$. In *a*), $(\tilde{a}, \tilde{b})_1 = (1, -1.3)$ and in *b*) $(\tilde{a}, \tilde{b})_2 = (5, -6.5)$ 157
50. This figure shows the response of (FULL) when a sinusoidal input is used. In *a*) the amplitude $I_1 = 0.5$ and in *b*) $I_1 = 1$. Notice that the location of the burst cycles occur at slightly different locations relating to the peaks of the inputs 159
51. This figure shows three different bursting patterns when three different amplitudes are used 161
52. This figure shows the response of (FULL) when a constant current pulse is used but (FS) exhibits a “fast spiking” or beating behavior (instead of bursting) 162

53. This figure shows the response of (FULL) when the parameters of (FS) are chosen to exhibit a “Nearly Parabolic” behavior [59]. In each figure the black line represents the time duration of the input. In a), the fast parameter set $\lambda_f = (0.25, 1.1, 1)$ was used with a stimulus intensity $\bar{I} = 0.5$ and a duration $T = 250$. These parameters were chosen to match experimental results found in [14]. In b) the fast parameter set $\lambda_f = (0.25, 1.15, 1)$ was used with a stimulus intensity $\bar{I} = 0.5$ and a duration $T = 750$. These parameters were chosen to match experimental results found in [76]. The difference between these responses and those in Figure 17 is that these patterns have action potential minima in the bursting patterns which are below their silent phase values. The patterns in Figure 17 have action potential minima which are elevated above the silent phase. Notice that these differences may occur not only in different cells in different layers of the visual system but in different animals (i.e. ferret vs. cat)..... 163

ABSTRACT

Certain mammalian visual neurons exhibit *On* and *Off* responses when given a light stimulus. In addition to these responses, [51] showed that for retinal ganglion cells, the neuron will also exhibit a *Mixed* response when given two simultaneous stimuli in different regions of the cell's receptive field. This *Mixed* response is a nonlinear combination of the *On* and *Off* responses. In this dissertation, a single cell model which can reproduce *On*, *Off*, and *Mixed* responses is developed and examined using leading order analyses and averaging. This model is developed from a current balance equation which includes a non-autonomous input $I(t)$, and consists of three coupled, first-order nonlinear differential equations which describe the dynamics of the membrane potential of the cell. When $I(t)$ is assumed to be a constant current pulse, the *On* and *Off* responses can be reproduced but will depend on both the duration and the amplitude of the input. When $I(t)$ is assumed to be monotone slowly decreasing, the model can reproduce the nonlinear properties for two simultaneous stimuli. In this dissertation, conditions which will guarantee each type of response will be found using the different subsystems of the model.

CHAPTER 1

INTRODUCTION

The primary goal of this dissertation is to develop a phenomenological model capable of reproducing qualitative dynamics which have been observed experimentally in neurons. Generally, neurons will exhibit many different forms of electrical activity. In mammalian sensory systems, for example, certain neurons exhibit *On* and *Off* responses when given appropriate excitatory and inhibitory stimuli. In some instances, such neurons can also exhibit a *Mixed* response where diminished *On* and *Off* responses are both present. For the current study, a phenomenological model which reproduces each of these three responses is developed. The model developed here will be referred to as (FULL). Upon completion of the model development, we will analyze the dynamics and describe the solutions of (FULL) in order to predict under which conditions (FULL) will be guaranteed to reproduce such responses. To do this, a general theory for analyzing the class of models defined by

$$\frac{dx}{dt} = f(x, y) + I(t), \quad x \in \mathbb{R}^M, \quad (1.1)$$

$$\frac{dy}{dt} = \epsilon g(x, y), \quad y \in \mathbb{R}^K, \quad (1.2)$$

will be given, since (FULL) belongs to this class. In (1.1)-(1.2), $I(t)$ is a non-autonomous input, and $\epsilon \ll 1$.

The responses of neurons are characterized by the release of action potentials. Action potentials are large shifts in membrane potential and neurons often “fire” these in brief

bursts of high-frequency discharge. Usually, when these high-frequency discharge patterns occur, the cell is said to be in its active phase. In bursting, the active phase is followed by a dormant phase, or silent phase, where membrane potential changes slowly. It has been shown that bursting behavior is implicated in synaptic plasticity [62] and selective communication between neurons [44]. As such, bursting is an important behavior for the model to reproduce. In (FULL), the multiple time scales between (1.1)-(1.2) play a key role in reproducing bursting phenomenon.

In this study, the physiological goal is to reproduce the *On*, *Off*, and *Mixed* responses and to determine under what types of external stimuli each response will occur. Both Kuffler (1953) [51], and Wang, Liets, and Chalupa (2003) [80] measured all three types of responses in retinal ganglion cells (cf. Figure 1). The *Mixed* response occurred when two point light stimuli were presented simultaneously in different regions of the cell's receptive field. All three types of responses have also been measured in sensory systems other than the visual system. For example, Evans (1992) [24] and He (2002) [34] showed that all three responses occur in auditory neurons as a result of having different acoustic stimuli. Hartings, Temereanca, and Simons (2000) [33] showed that these responses can also occur in sensory neurons in thalamic reticular nucleus of rats. The stimulus in these experiments was vibrissa (whisker) deflection in a specified direction under some duration. With these experiments in mind, it is clear that analyzing a mathematical model which reproduces these responses may foster a greater understanding of neuronal communication in a variety of sensory systems.

Even though the *On*, *Off*, and *Mixed* responses occur in many sensory systems, in this study we will concentrate on visual system cells. Illustrated in Figure 1 are these responses in retinal ganglion cells. In Figure 1a) an *On* response is illustrated. In this case, the activity of the cell immediately increases when a light stimulus is applied to the *Plus* part of its receptive field. On the other hand, Figure 1b) shows an *Off* response. When the stimulus is applied to the *Minus* part of the receptive field, the activity of the cell is increased only when the stimulus is turned off. This type of response will also be referred to as Post Inhibitory Rebound (PIR). Illustrated in Figure 1c) is the *Mixed* response. Notice that when two stimuli are given, the cell produces both an *On* and an *Off* response. One of the goals in this study is to reproduce these responses and to find the necessary conditions that will guarantee such responses.

Mathematically, (FULL) is a non-autonomous bursting model. In this study, a general theory for analyzing (1.1)-(1.2) for specific classes of inputs is given. In the model $I(t)$ represents the net synaptic input the cell receives due to an external stimulus. We will consider only inputs $I(t)$ that are physiologically relevant. It will be shown that constant current pulses and smooth monotone slowly decreasing functions can reproduce *On*, *Off*, and *Mixed* responses. When $I(t)$ belongs to these classes, (FULL) can be analyzed using bifurcation theory and singular perturbation techniques such as the method of averaging.

Some analyses of non-autonomous systems of the form (1.1)-(1.2) already exist. For a constant current pulse input, Othmer and Watanabe (1994) [58], and Xie, Othmer, and Watanabe (1996) [87] have studied harmonic and subharmonic solutions in a two variable

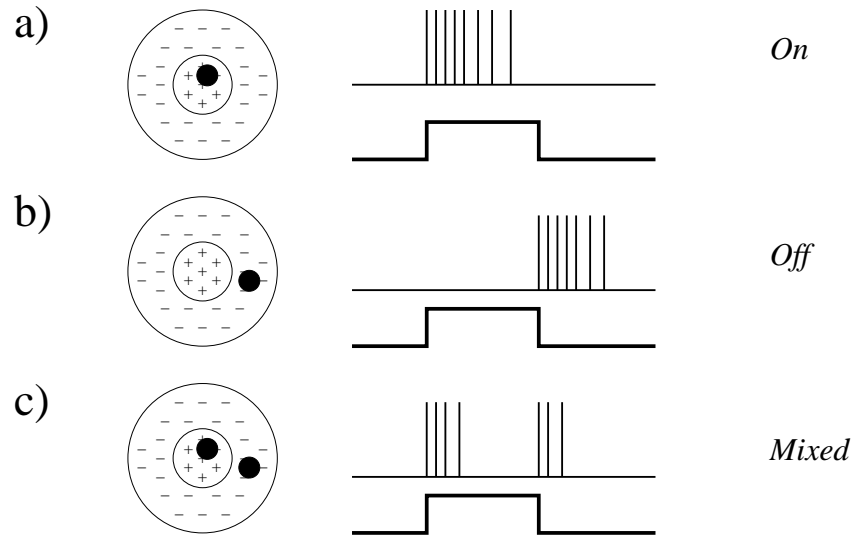


Figure 1. Shows typical *On* and *Off* responses in a retinal ganglion cell. In each figure, the dark spot represents the location(s) of the stimulus. In the right column, the spike train of the cell is shown over the time course of the stimulus amplitude. a) illustrates a typical *On* response; b) shows a typical *Off* response; c) shows the *Mixed* response of a ganglion cell when given two simultaneous stimuli [51]. Here the *On* part of the receptive field (indicated by + signs) is surrounded by an *Off* component (indicated by - signs). Since the *On* part of the receptive field is surrounded by the *Off* part, this receptive field is often referred to as an “On-Center” receptive field. Some ganglia have “Off-Center” fields where this orientation is reversed.

model. Alexander, Doedel, and Othmer (1990) [2] analysed a similar model in which the non-autonomous forcing occurred in the slow variable. There, they mention that it is usually reasonable to consider sinusoidal forcing or step function forcing (constant current pulse). In numerical experiments, they showed that the forced Fitzhugh-Nagumo model (described in a later section) can undergo different types of oscillatory behaviors. In addition, He, Zhang, Yang, and Shi (1999) [35] also investigated the effects of a non-autonomous sinusoidal input on chaotic behavior for a two variable model.

It is important to note that in certain experiments, such as [24, 49, 73], responses were

measured as a consequence of a sinusoidal modulation stimulus. To simulate these experiments (and thus gain a greater understanding of the responses of neurons) a sinusoidal input may be an appropriate form for $I(t)$. Although this may be the case, a complete understanding of the dynamics of (FULL) for such an input is beyond the scope of this study. Here, analyzing (FULL) for the class of smooth monotone slowly decreasing inputs (or just monotone slowly decreasing inputs) provides a starting point for understanding the dynamics of the model with a sinusoidal input.

For the class of monotone “slowly” decreasing inputs $I(t)$, the “slow” rate of decay of $I(t)$ allows (1.1)-(1.2) to be augmented to a higher dimensional autonomous system:

$$\frac{dx}{dt} = f(x, y), \quad x \in \mathbb{R}^M, \quad (1.3)$$

$$\frac{dy}{dt} = \epsilon g(x, y), \quad y \in \mathbb{R}^{K+1}. \quad (1.4)$$

For the analysis presented in this study, $M = 2$ and $K = 1$. Therefore (1.3)-(1.4) is a system of two fast variables and two slow variables. Some analyses of two fast and two slow variable models already exist and can be found in [16, 19, 32, 74, 75]. In this study, the augmented model will be used to reproduce the *Off* and the *Mixed* responses. For such responses, the solution of the augmented model must exhibit PIR upon the release of a stimulus. As such, the goal is to find conditions on the input which will guarantee PIR for the augmented system.

Before the model development is fully described in Chapter 2, some basic physiological background is necessary. Specifically, the fundamental physiology of the visual system is given. Something to keep in mind is that the model can also be used to explain behaviors

in other sensory systems even though this dissertation does not emphasize other systems. For additional background, a description of some existing neuron models will be given. Although the model presented here is a single cell model, network properties and connectivity play a major role in the responses of neurons. Therefore, in addition to examples of single cell neuron models, some network models are presented and discussed briefly. In the description of the physiology and the existing models, the motivation for using a model of the general form (1.1)-(1.2) will also be explained.

Physiology

In the mammalian visual system there are three principal compartments which help process visual information. These three compartments are classified as the retina, the lateral geniculate nucleus (LGN), and the visual cortex. The retina is connected to the LGN via the optic tract, and the LGN is connected to the visual cortex through optic radiations [40]. Due to the complexity of the brain, the exact connectivity and function of these compartments has yet to be fully understood [55]. For example, the function of some cortical neurons whose paths feed back to the LGN has yet to be determined [26, 72, 83]. Recognizing these limitations, the assumption that visual information from the retina travels along visual pathways to the visual cortex in the back of the brain will be used throughout this work. There are two major visual pathways; the information which comes from the left visual field travels along the right pathway, and the information which comes from the right visual field travels along the left pathway. Further information about visual pathways, connectivity and

functions are well described in books such as [40, 55, 64]. These books are the primary sources for the majority of physiology described in this dissertation.

Most individual neurons have a structure comprised of a dendritic tree, an axon, and a soma (nucleus). Neurons are “connected” through synapses located on the dendritic tree and along the axon. A single neuron may receive information (current input) from as few as one other neuron to as many as 100,000 [64]. Information from a neuron travels along its axon in the form of action potentials to a synaptic connection. Once the information reaches the synapse, it can then be transferred to another neuron in its pathway. Thus, visual information travels across many different neurons in different compartments.

The region on the back of the retina (or equivalently visual field) where a light stimulus will cause a cell to release action potentials is called the cell’s *receptive field*. A cell’s receptive field can play an important role in predicting the output of a cell. The receptive field gives a convenient and simple description for the output of a cell when a stimulus is applied [40]. In this section, a description of the receptive fields for cells in each of the three compartments (retina, LGN, and visual cortex) will be given. Often the receptive field is comprised of a *Plus* and a *Minus* region. When a light stimulus is given in the *Plus* region, an *On* response can occur. When a light stimulus is given in the *Minus* region, an *Off* response (or PIR) can occur. Thus, the location of a light stimulus often determines whether a given cell will exhibit an *On* or *Off* response.

As illustrated in Figure 1, retinal ganglion cells have what is normally referred to as a center surround receptive field. If a narrow stimulus is applied to the *Plus* region of

the receptive field of the cell, the activity of the cell immediately increases (cf. Figure 1a). Conversely, as is illustrated in Figure 1b), if a similar stimulus is applied to the *Minus* region of the receptive field, an *Off* response occurs. When the *Plus* region is surrounded by the *Minus* region, the receptive field is called an “On” center receptive field. Conversely, when the *Minus* region is surrounded by the *Plus* region, the receptive field is called an “Off” center receptive field.

Although studies of the receptive fields for LGN cells are still incomplete [55], Hubel and Wiesel [42] showed that certain neurons in the LGN also have “On” and “Off” center surround receptive fields similar in shape to those of the ganglion cells illustrated in Figure 1.

Mapping the receptive field of cells in the visual cortex is an ongoing process. Simple cells in the primary visual cortex (layer V1) are defined by the shape and behavior of their receptive fields. Simple cells also exhibit *On* and *Off* responses but the shapes of their receptive fields frequently differ from LGN and retinal ganglion cells. Typically these cells respond better to bar stimuli of a preferred orientation (cf. Figure 2) [41, 42]. Hubel and Wiesel [42] devised a hypothesis to explain the particularity in the shapes of the receptive field of simple cells. Since LGN cells have center surround receptive fields and many can connect to a single cortical cell, then perhaps the receptive field of a simple cell is an accumulation of the receptive fields of the LGN cells. This hypothesis assumes (1) a feed-forward model where the visual information only travels towards the visual cortex and (2) that the connectivity of cells is related to the shape of their receptive field. Classifying

cells according to their receptive fields is one way to describe how cells interpret visual information. It is worth noting that other cells in the visual cortex have been classified as complex cells. These cells do not have receptive fields which can be classified with *Plus* and *Minus* regions and thus are beyond the scope of this study.

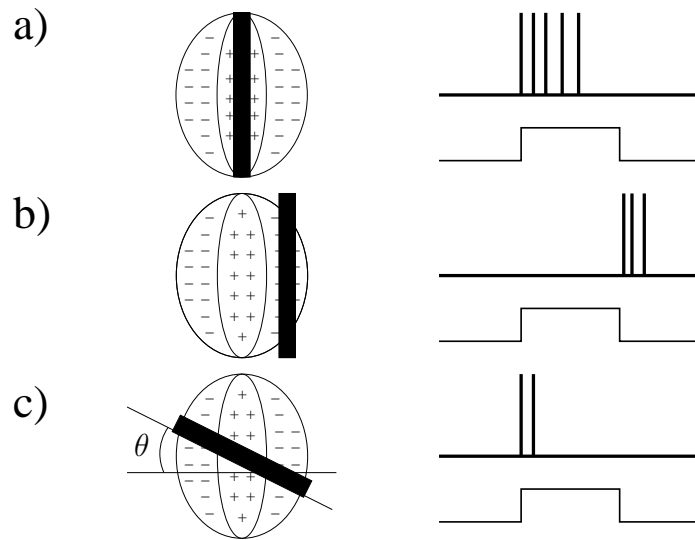


Figure 2. Shows typical *On* and *Off* responses for simple cells in the primary visual cortex. In each figure, the dark bar represents the location and shape of the stimulus. In the right column, the spike train of the cell is shown over the time course of the stimulus amplitude. a) illustrates a typical *On* response; b) shows a typical *Off* response; c) illustrates a diminished *On* response when the stimulus bar covers both *Plus* and *Minus* regions. The angle θ shown in c) is the orientation angle of the stimulus. In a) the angle θ is said to be in orientation preference for this particular type of receptive field whereas in c) θ is not in orientation preference.

The primary interest in this work is in modeling neurons which have receptive fields with *Plus* and *Minus* regions. The examples above show that certain cells (ganglion, LGN, and simple) in each compartment have these types of receptive fields. Although the model

(FULL) simulates visual system cells, in general other sensory neurons will also exhibit these behaviors when given an appropriate stimulus.

Existing Models

Many different mathematical models have been used to model the responses of visual neurons. Most biological models of such systems can be grouped into two classes: biophysical and phenomenological models. Both classes have advantages and disadvantages. Biophysical models attempt to incorporate as many known biological facts and data as necessary to achieve quantitative results. Unfortunately these models are often very complicated and are therefore not amenable to mathematical analysis. On the other hand, phenomenological models attempt to grasp the qualitative features of a biological system. Since phenomenological models are qualitative in nature, these models are often lacking important biological features. The mathematical model presented in this study is phenomenological in nature but contains aspects which can be related to biophysical features and will be defined in greater detail in Chapter 2. In this section descriptions of some existing biophysical and phenomenological models are given. These models have been subdivided into two categories: single cell models and network population models.

Single Cell Models, Bursting and PIR

One of the most important biophysical models of a neuron is the Hodgkin-Huxley model. Hodgkin and Huxley (1952) [39] were the first to develop a quantitative model for the propagation of electrical current along an axon. Their experiments were conducted

on the giant axon of a squid. In these experiments, Hodgkin and Huxley determined that there were two primary ionic currents, sodium and potassium. They also noticed other types of currents, but these currents were relatively small and thus were lumped together into a leak current. One of the most important features of this model is that it was able to reproduce the spiking behavior observed experimentally. Since visual neurons typically generate spikes, this model has been adapted and used to model spiking visual system neurons [4, 7, 11, 17, 30, 38, 81].

In general, a Hodgkin-Huxley type model always has a current balance equation of the form

$$C_m \frac{dV}{dt} = - \sum_x I_x + I(t), \quad (1.5)$$

where V is the (somal) transmembrane voltage, C_m is the total cell capacitance, I_x are ionic currents of type x , and $I(t)$ is the applied current. Typically, the ionic channels are written in terms of voltage gated activation (or inactivation) variables, n_x , as

$$I_x = \bar{g}_x n_x^p (V - V_x) = g_x (V - V_x), \quad (1.6)$$

where the evolution of the gating variable is

$$\frac{dn_x}{dt} = \frac{n_{x\infty}(V) - n_x}{\tau_x(V)}. \quad (1.7)$$

In (1.6), \bar{g}_x is the maximal conductance for a channel of type x , and g_x is the time dependent conductance for that channel; n_x^p describes the probability that a channel of type x is open (p is an integer), and V_x is the Nernst potential. In the Hodgkin-Huxley model [39], the current balance equation included three terms of the type found in (1.6) corresponding

to the sodium, potassium, and leak channels. Experimental data were used to establish the relaxation times $\tau_x(V)$, the voltage dependent conductances, and the current activation (inactivation) functions, $n_{x\infty}$. In general, it is often the case that $\tau_x(V)$ in (1.7) have very different magnitudes for different channels. Models of this type have been used to study the quantitative features of spiking neurons.

Some qualitative behaviors of the Hodgkin-Huxley model can be reproduced using simplified two-variable models. The Fitzhugh-Nagumo [25] model is one such model. An important feature of the Fitzhugh-Nagumo model is that it can reproduce spiking behavior. To do this the model incorporates a fast variable v , and a slow variable w . It can be written in a general form as

$$\frac{dv}{dt} = f(v, w) + I, \quad (1.8)$$

$$\frac{dw}{dt} = \epsilon g(v, w), \quad \epsilon \ll 1 \quad (1.9)$$

where the nullcline $f(v, w) + I = 0$ has a cubic shape in v (with w fixed), $g(v, w) = 0$ intersects $f(v, w) = 0$ at precisely one location, and I represents a constant applied current [45]. For certain values of I , the fixed point of (1.8)-(1.9) is unstable and lies in the middle branch of the cubic $f(v, w) + I = 0$. When this happens, the Fitzhugh-Nagumo model typically has a globally stable periodic orbit. Thus, the solutions of this model can qualitatively reproduce spiking phenomena, such as continuous spiking, found in excitable cells (such as neurons). In addition to the Fitzhugh-Nagumo model, other two-variable models such as Morris and Lecar (1981) [54], and Hindmarsh and Rose (1982) [36] have also been used to study spiking and oscillatory phenomena.

When certain neurons are given a “constant current pulse” $I(t)$ with a specific amplitude and duration they exhibit bursting electrical activity (bursting). For example, *in vivo* recordings illustrated in Brumberg, Nowak, and McCormick (2000) [14] and Wang (1999) [81] show that certain mammalian neurons exhibit short duration bursts when a constant current pulse is used. As previously mentioned, this type of behavior is common in neurons and is an important feature to include in a single cell model. Illustrated in Figure 3 are four different types of oscillatory behaviors (including bursting) and their classifications adapted from [59].

In addition to bursting, certain neurons elicit responses which can exhibit post inhibitory rebound (PIR) (as illustrated Figure 1b) and Figure 2b)). For example, in addition to those already mentioned, *in vitro* recordings of certain thalamocortical cells in rats [18] show an *Off* response similar to those illustrated in Figure 1b) where multiple rebound spikes occur (also referred to as a short post inhibitory rebound burst). Two-variable models like the Fitzhugh-Nagumo model can be made to generate a single post rebound spike, but cannot reproduce any rebound bursts when given a constant current pulse. For these models to generate spikes, the location and stability of the fixed point are important. For example, a constant current pulse changes the location of the fixed point and as a consequence affects its stability. If the pulse causes an unstable fixed point on the middle branch, then the model will spike continuously during the pulse. When the pulse is turn off, either the fixed point becomes stable or remains unstable (this depends on the amplitude of the pulse). In the former, the spiking will cease immediately, but the solution may travel around

the stable orbit once after the pulse. If on the other hand, the fixed point remains unstable, the spiking will continue and will not stop and as such a PIR burst cannot occur. Although the two variable models described above can reproduce some characteristics of neurons, they cannot reproduce other features needed in a single cell model such as bursting and PIR bursts.

Since bursting and PIR are important behaviors to include in a single cell model, two-variable models may not be adequate when modeling single neurons. To include these behaviors (specifically bursting) many authors have incorporated additional variables in their models. Again, with these models, there are two different classifications. Models such as those in [4, 17, 29, 38, 63, 71, 82] are based on biophysical mechanisms, with parameters and model functions derived from experimental data. These mechanisms and parameters are often incorporated into a Hodgkin-Huxley type model, as described above. Other models, such as those in [20, 37, 59], use a polynomial structure and aim at maintaining the important qualitative features of these bursting models.

In these polynomial models, it is often the case that there are two fast variables and one slow variable. For example, the introduction of the “adaptation” variable (slow) in the Hindmarsh-Rose model (1984) [37] allowed the model to generate bursting behavior. The general form of the Hindmarsh-Rose model of a thalamic neuron can be written as

$$u' = v - F(u) + I - z \quad (1.10)$$

$$v' = G(u) - v \quad (1.11)$$

$$z' = \frac{H(u) - z}{\tau}, \quad (1.12)$$

where the functions F , G , and H are polynomials. Usually τ is considered large, making z a slow variable compared to u and v . The Pernarowski polynomial model [59] is similar to the Hindmarsh-Rose model and will be described in greater detail later. The Pernarowski model will be used and expanded on for the majority of the modeling in this dissertation.

The biophysical models and the polynomial models described above can reproduce bursting patterns. Since bursting was first modeled extensively for β -cells, the mathematical mechanisms for bursting were investigated in terms of these models. These investigations led to many different classification schemes based on the different mechanisms. Rinzel (1987) was the first to propose a classification scheme [69]. A good summary of these classifications can be found in [45]. Other classification schemes have been described in [10, 20, 43, 59, 70, 71]. In this dissertation the primary interest is in “square-wave” bursting (cf. Figure 3), also referred to as a type *Ia* [69] or a “fold/homoclinic burster” [43].

A final model to consider is the integrate-and-fire (IF) model, which is often used to model neurons. The basic IF model is:

$$c_m \frac{du}{dt} = u_r - u + I(t), \quad \text{if } u \geq \vartheta \text{ then } u \rightarrow u_r \quad (1.13)$$

where u is the transmembrane voltage, c_m is the membrane capacitance, u_r is the rest potential, and $I(t)$ is the driving current. The driving current is integrated until the membrane potential is driven across the threshold value, ϑ , at which point an action potential is initiated. Once the spike occurs, the potential u is reset to a new value $u_r < \vartheta$, and the process is repeated. Therefore, in these models, spikes are identified with the reset times t_k for the given applied current.

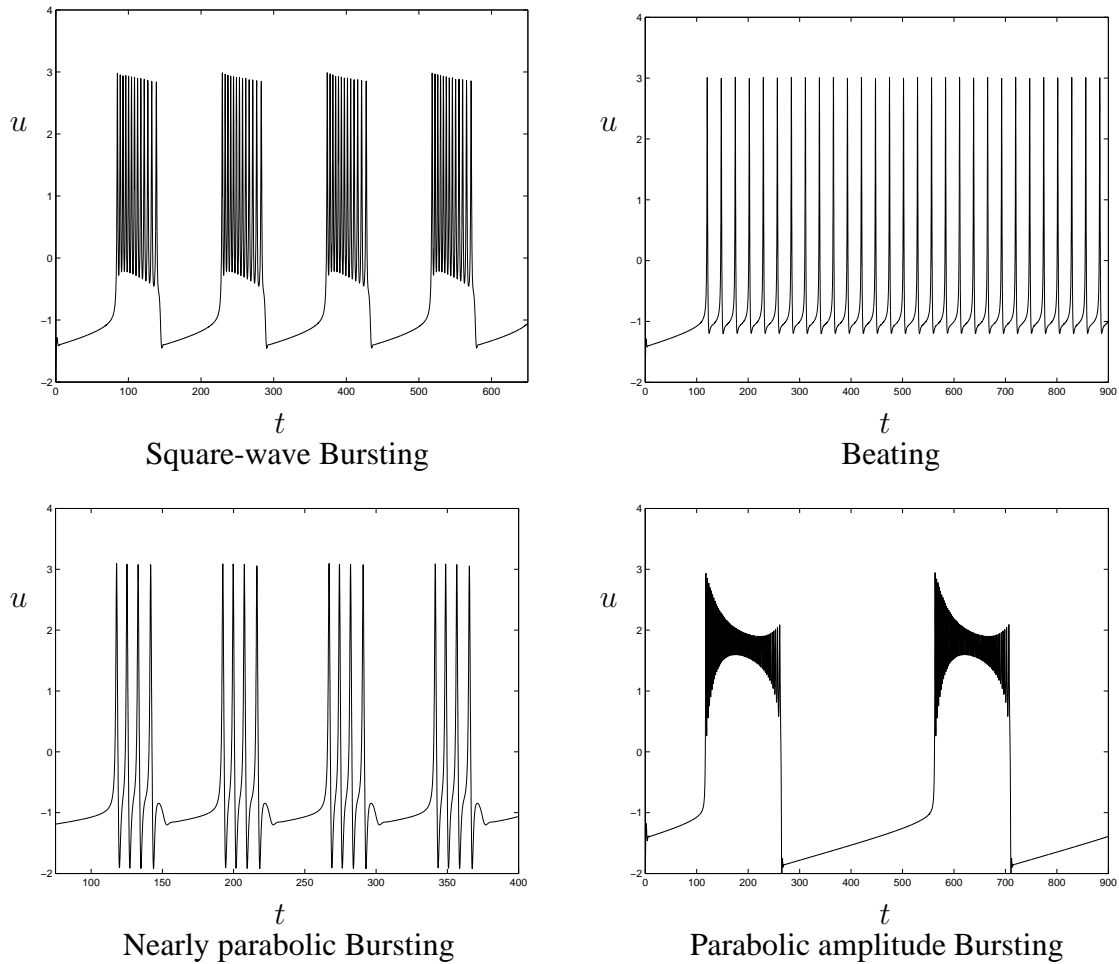


Figure 3. Some examples of oscillatory behaviors (including three types of Bursting) with their classifications given.

One of the most important features of the IF model is its simplicity. Although IF models are simple in nature, like other phenomenological models they often lack important physiological properties. IF models with one equation generally cannot reproduce any bursting or rebound patterns. In order to reproduce these behaviors, many modelers have augmented the basic IF mechanism with other equations. Unfortunately, when such models are expanded, many of the simple mechanisms become more complex and, in turn,

more difficult to analyze. For example, the Integrate-and-Fire-or-Burst (IFB) model [73] includes an equation which accounts for the inactivation of a calcium current. By adding this equation, the model can exhibit some of the important behaviors of neurons such as bursting. In the experiments conducted in [73] a sinusoidal current injection was used to study the responses of thalamocortical relay neurons *in vitro*.

The IF models have also been augmented to include spike adaptation and facilitation (which will be described in greater detail in a Chapter 2). For example, Rauch, LaCamera, Luscher, Senn, and Fusi (2003) [67] showed that an IF model augmented with an additional current (which is included to model the effects of facilitation and adaptation) can predict the mean firing rate of cortical pyramidal cells. Also, Brette and Gerstner (2005) [13] showed that an exponential IF model including adaptation was able to reproduce dynamics such as bursting and PIR. In conclusion, although IF models can be made to include more visual system dynamics (bursting, PIR, etc.), they form a different class of models than those described by (1.1)-(1.2) and therefore will not be discussed further here.

Network Models

When studying the visual system it may be that the importance should not be placed on the single neuron but on network properties. Since neurons are often organized in populations (often referred to as layers), the activity of the cells in a population may or may not affect the activity of cells in other populations. For example, visual neurons in Layer 4 of the primary visual cortex (V1) are separated into ocular dominance columns [42]. The term ocular dominance columns is used to refer to groups of cells (columns) which receive

inputs specifically from a single eye. This suggests that the cell-to-cell connections of the network may be group selective and may determine functionality of the population. Ultimately studies like the one here may contribute to the modeling of network populations and potentially to an understanding of the function(s) of different layers in the cerebrum. Although there is a large history of population models including [1, 3, 15, 27, 28, 46, 56, 57], a description of only a few will be given in this section.

In some studies of neuronal systems authors use Hodgkin-Huxley type models to model the electrical activity in individual cells. For instance, [78] used such a model to examine wave propagation in a two layer network model of a part of the thalamus. The model of each cell in the layer is given by the Hodgkin-Huxley equations of the general form

$$v' = f(v, h) \quad (1.14)$$

$$h' = \epsilon \frac{(h_\infty(v) - h)}{\tau_h(v)}, \quad 0 < \epsilon \ll 1 \quad (1.15)$$

where the terms in $f(v, h)$ are of the form defined in (1.6). In this model, intra- and inter-layer synaptic coupling is modeled in a continuum by using an integral term which weights excitatory and inhibitory synaptic inputs as

$$v_t = f(v, h) - g_{syn}(v - v_{syn}) \int_{-\infty}^{\infty} W(x - y)s(y, t) dy, \quad (1.16)$$

$$h_t = \epsilon \frac{h_\infty(v) - h}{\tau_h(v)}, \quad (1.17)$$

$$s_t = \alpha(1 - s)H(v - \theta) - \epsilon\beta s. \quad (1.18)$$

In this model, s represents the activation (inactivation) of the synaptic coupling between cells in the layer. In (1.16), $W(x - y)$ represents the probability that there is a synaptic

connection between the cells located at position x and y , and $W(x)$ is referred to as the “synaptic footprint”.

Using this model in a two layer simulation one can produce two types of waves: smooth waves and lurching waves. A smooth wave is a wave which propagates with a constant velocity. A lurching wave does not propagate with constant velocity but propagates according to the coupling dynamics of the layer. The lurching wave phenomenon is described as being caused by the post inhibitory rebound properties of the cells in the layer. Thus, PIR can cause interesting dynamics in a network model.

In contrast, in [12], Bressloff and Cowan (2002) have done much analysis on continuum models to explain cortical pattern formation in the visual cortex. Incorporated in their model and analyses are earlier works and results found in [85] and [86]. The model in [12] considers excitatory (E) and inhibitory (I) cells at position $\mathbf{r} \in \mathbb{R}^2$ in layer V1 of the cortex which have certain orientation preference given by θ . Orientation preference is the mechanism illustrated in Figure 2, where the cortical cell has the greatest response when given a stimulus with a certain preferred orientation. The connectivity of cells in the layer plays an important role in the modeling. Such continuum models of V1 have the general form:

$$\begin{aligned} \frac{\partial a_l(\mathbf{r}, \theta, t)}{\partial t} &= -a_l(\mathbf{r}, \theta, t) + h_l(\mathbf{r}, \theta, t) \\ &+ \sum_{m=E,I} \int_{\mathcal{R}^2} \int_0^\pi w_{lm}(\mathbf{r}, \theta | \mathbf{r}', \theta') \sigma [a_m(\mathbf{r}', \theta', t)] \frac{d\theta'}{\pi} d\mathbf{r}', \end{aligned} \quad (1.19)$$

where a_l ($l = E, I$) is the activity of the layer at time t ; h_l is the external stimuli; σ are output functions; and w is the weight of connection from other cells in the layer. The

weight, w , was motivated by experimental observations and is a combination of “local” and “non-local” lateral connections between cells in the network. In [12], the orientation tuning patterns of the visual cortex were explained to be a consequence of Turing instabilities generated by the cell-to-cell coupling.

Large scale IF network models have been used to reproduce simple cell (cf. Figure 2) behavior of cortical cells in V1. A good example of such a model can be found in [84] where cortical architecture and connection strengths were estimated from raw data. Since the basic IF unit is simple, larger network models can be simulated (in [84], 128^2 IF neurons were simulated). The population is divided into excitatory (E) and inhibitory (I) IF point neurons. In the model these populations evolve according to the following coupled system of differential equations

$$\frac{dv_P^j}{dt} = -\lambda v_P^j - g_{PE}^j(t) [v_P^j - V_E] - g_{PI}^j(t) [v_P^j - V_I] \quad (1.20)$$

where $P = E, I$ and the superscript $j = (j_1, j_2)$ indexes the spatial location of the neuron within the cortical layer. Each conductance in (1.20) is time dependent and arises from input forcing from LGN, noise to the layer, and from the cortical network activity of each population (excitatory and inhibitory). The intra-cortical coupling is described by these time dependent conductances. Although these large scale network models can be insightful about the network properties, such network IF models are not amenable to analysis.

In the aforementioned studies, electrical activity of individual cells is highly dependent on the network properties. Regardless of what assumptions are made in a network model, many individual cells in the visual system exhibit stimulus response behaviors like those

illustrated in Figure 1 and Figure 2. Without knowing the precise architecture of a visual system network, such individual cell behavior can be viewed to be merely a consequence of its net synaptic input. From this point of view, $I(t)$ in (1.5) (or in (1.1)) can be interpreted as the net synaptic input resulting from some stimulus given in the cell's receptive field (visual stimulus for visual neurons). This assumption will be used to develop a synaptic model which describes some general types of inputs, $I(t)$, that a cell may receive.

Outline of Dissertation

The current chapter explored background information, existing models, and analyses. In Chapter 2, development of the phenomenological model for the responses of neurons, (FULL), is presented. This model belongs to the class given by (1.1)-(1.2), where a non-autonomous input $I(t)$ is included. Also in Chapter 2, a description of synaptic transmission will be given, leading to a simple two channel Hodgkin-Huxley synaptic model. By incorporating different aspects of plasticity, the synaptic model solutions will be used to generalize the shapes of the input $I(t)$ in the single cell model. These shapes incorporate different activation and inactivation rates, and as a result, the need to analyze the model under such inputs is manifested. The individual cell model is a generalization of the polynomial model developed in [59] and [60] used to study bursting electrical activity. Previous analyses of (FULL) [59, 60] make it easier to predict parameter regions where such behavior occurs.

In Chapter 3, the necessary model definitions that will be used throughout the study

are given. First, the fast and slow subsystems are defined and the dynamics of each are described. Recall that in bursting, the solution travels through both an active and a silent phase. The slow-subsystem will be used to describe the slow flow of solutions along the silent phase. In order to approximate the slow flow of solutions along the active phase, the averaged-fast-subsystem is derived. Using these subsystems, the active phase durations and the silent phase durations are also derived. To reproduce bursting, the fast subsystem of the model must have a region of bistability. In such a region, the basin of attraction of the periodic orbits will play a major role in the description of the numerical traces of the solutions of (FULL). For certain initial conditions, solutions of the model may exhibit behaviors which are not observed in neurons. Examples of these will be given and explained to be a consequence of the basin of attraction of the periodic orbits.

With the model definitions and issues arising from the basin of attraction having been established, in Chapter 4 the model is analyzed under constant current pulses. It will be shown that all of the responses in Figure 1 can be reproduced for certain current pulse inputs. First, the *On* response is reproduced and analyzed, showing that to guarantee an *On* response, certain threshold conditions on the amplitude must be satisfied. Also, the type of *On* response will depend on the duration of the input. Examples of these different types will be given and explored. Second, the *Off* response is reproduced and analyzed, showing that to guarantee such a response, not only are certain threshold conditions necessary, but the duration of the input must be of sufficient length. In addition to these two types of responses, conditions which will guarantee a *Mixed* response are also stated. In this case,

the input will be defined as an *On* and *Off* constant current pulse. The *Mixed* responses will be shown to depend on the thresholds and durations of both the *On* and the *Off* parts of the pulse.

Using some of the results of the analyses for a constant current input, the model is analyzed for a monotone slowly decreasing input $I(t)$ in Chapter 5. First, the class of monotone slowly decreasing inputs is defined. Under such inputs, (FULL) can also reproduce the *Mixed* response. Since ultimately the goal of this study is to predict and describe the solutions of (FULL) when such a non-autonomous input is applied, Chapter 5 gives a general theory for doing this. When inputs from the monotone slowly decreasing input class are used, the model can be augmented to a higher dimensional autonomous system, as previously described. For this augmented model, the averaged-fast-subsystem is redefined. The averaged-fast-subsystem will be analyzed and used to predict the *On* part of the *Mixed* response. It will be shown that under certain conditions, an active phase transition will be guaranteed to occur in finite time. This transition will terminate at a homoclinic bifurcation where a rapid transition to the silent phase of the solution will occur. Once this transition occurs, the flow of the augmented model will be governed by the slow-subsystem of the augmented model. With this in mind, the slow-subsystem will be defined and analyzed. In order to guarantee an *Off* part to the *Mixed* response, the trajectories of the solution must reach a specified target curve. The analyses conducted in Chapter 5 will establish the conditions needed to guarantee a *Mixed* response for a special class of inputs. The two subsystems will then be pieced together to describe the full cycle for a *Mixed* response.

Chapter 6 contains the conclusions of this study and the results of the analyses of (FULL) are compared with selected experimental observations. There, by choosing an input of the appropriate form, the model reproduces many of the behaviors observed experimentally. In addition, although analytical results are lacking, numerous numerical solutions are illustrated. These responses are generated as a result of a sinusoidal input and show that the model (FULL) does reproduce certain experimental responses.

CHAPTER 2

MODEL DEVELOPMENT

Using elements of the physiology described in the introduction, the phenomenological model will be developed in this chapter. First, a simple two channel Hodgkin-Huxley type of synaptic model will be presented. This model will incorporate some aspects of synaptic plasticity and thus a description of plasticity will be given. The solutions of the synaptic model will be used to generalize the shapes of the non-autonomous inputs $I(t)$ in the single cell model. The synaptic input shapes will have a major effect on the types of responses produced by the model. The description of synaptic dynamics is discussed in the following section and implemented in the modeling.

Synaptic Model

In this section we introduce certain background information on some synaptic mechanisms. Synapses are “contacts” between cells where signals can be transmitted. The general description of synaptic transmission has been well developed and explained in texts such as [55] and [64], and will only be summarized here.

There are two main types of synapses, electrical and chemical. In an electrical synapse, current flows directly from the presynaptic cell to the postsynaptic cell to affect its membrane potential. This flow occurs through *connexons*, channels which cluster to form gap

junctions. In a chemical synapse, current from the presynaptic cell causes a release of neurotransmitters which then bind to receptors on the postsynaptic cell. These receptors can affect (or themselves be) ion channels which can open to allow ionic flow into the postsynaptic cell. As in an electrical synapse, this current flow affects the membrane potential of the postsynaptic cell. These changes in membrane potential on the postsynaptic cell are called postsynaptic potentials (PSPs).

Generally, changes in membrane potential will result in the opening or closing of ionic channels. These ionic channels are responsible for the “transmission” of action potentials across a synapse. Terms such as depolarization and hyperpolarization are often used to describe some of the mechanisms which cause changes in membrane potential. Typically, a current flowing from outside the neuron to the inside is represented as a negative current. The term depolarization is used to describe the reduction in the magnitude of the membrane potential towards zero (making the membrane potential less negative). The term hyperpolarization refers to an increase in the magnitude of the membrane potential (making the membrane potential more negative). An ionic channel is said to be *activated* when the probability that the channel will open is increased. Activation results in the opening of more ionic channels creating an increased current flow which then leads to changes in PSPs. Alternately, *inactivation* will cause closing of ionic channels. This terminology will be used in modeling to describe the change in channel dynamics as it relates to an applied current.

For the purposes of this study, a description of synaptic plasticity and how it affects

PSPs will also be given. The PSP at a synapse can be characterized as either excitatory (EPSP) or inhibitory (IPSP). An EPSP will cause an increase in the membrane potential (depolarization) while an IPSP will cause a decrease (hyperpolarization) and will be referred to as excitation and inhibition, respectively.

The synaptic population of a postsynaptic cell can be divided into two populations: excitatory and inhibitory. Excitatory synapses will cause EPSPs and inhibitory synapses will cause IPSPs. The total (or net) synaptic input to the cell will be determined by total inputs from each of these two populations. The current from each PSP at different synapses is integrated at the cell's soma (in the spike initiation zone). When this accumulation reaches a depolarization (or an excitatory) threshold the cell fires a spike. Since EPSPs are excitatory and IPSPs are inhibitory, the net effects from each population can play a significant role in the total change of the cell's membrane potential. For example, if a cell only receives inputs from excitatory synapses then the net synaptic input will be excitatory whereas the net synaptic input will be inhibitory if a cell only receives input from inhibitory synapses. In the following section, a description of how the presynaptic input affects the postsynaptic potential is given.

Plasticity

Synaptic plasticity is a term used to describe a synapse's ability to adapt according to the different types of inputs it receives over a period of time. Usually the time course which affects the adaptability of a synapse occurs on a *short-term* or *long-term* period. For instance, repetitive activity at a synapse can produce alterations in the synaptic efficacy on

both the *short-term* (milliseconds, seconds) and on the *long-term* (hours, days). Since the effects of *long-term* plasticity occur on a much longer time scale than will be explored in the modeling, they will be disregarded in this study. Books such as [47] and [55] provide detailed descriptions of the different types of synaptic plasticity.

When discussing the flow of information across a synapse, questions about the efficacy of the synapse are often asked. For example, given a presynaptic potential what is the probability it will cause a postsynaptic current? Studies such as [5, 6, 48, 68] have shown that synaptic connections are unreliable. Typically, the probability that a postsynaptic potential occurs given a presynaptic potential can vary between 0.1 and 0.9. The probability often depends on the timing and the history of the presynaptic potentials. In addition to unreliability, the amplitudes of PSPs may also have high variability. Koch [47] (p. 327) contends that one explanation for the unreliability of synapses is that it allows each synapse to “adapt” to the dynamic range of synaptic mechanism.

Facilitation and depression are two examples of short-term synaptic plasticity. Facilitation is the mechanism which describes a progressive increase in the amplitude of each postsynaptic potential when a succession of presynaptic potentials (spike train) arrives at the synapse (cf. Figure 4a)). The mechanism for facilitation can be described by an increase in the efficacy of the release and binding of neurotransmitters from the presynaptic to the postsynaptic cell as each spike arrives from a train. Synaptic depression on the other hand can be described by a progressive decrease in the amplitude of postsynaptic potentials (cf. Figure 4b)). In general, the mechanisms which regulate synaptic depression are not well

understood but are often associated with a reduction in the efficacy of the release of neurotransmitters. For a synapse that exhibits both facilitation and depression, the time scale of the effects of facilitation is believed to be slightly faster than that of depression [53]. Thus, such a synapse will have an increase in PSP amplitude initially (due to facilitation) followed by a decrease in PSP amplitude (due to depression).

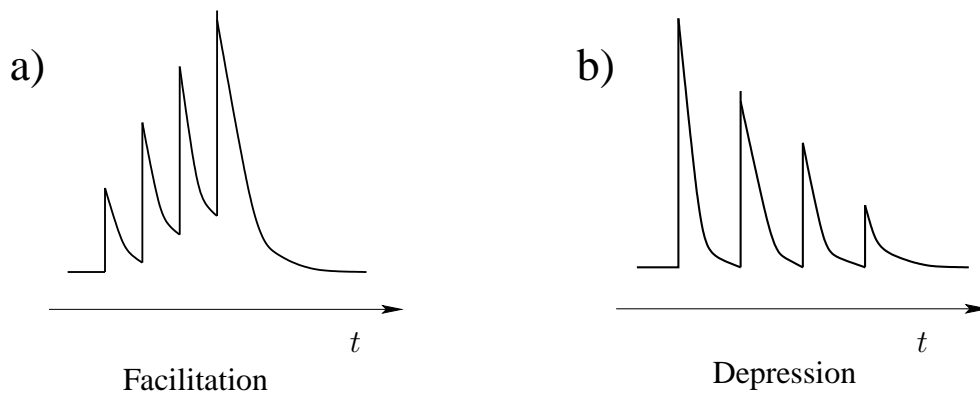


Figure 4. Shows the effects of synaptic facilitation and depression on the postsynaptic potential as a function of time (adapted from Figure 12.2 in [55]). Each surge in membrane potential corresponds to the effect of a presynaptic spike (4 spikes). Illustrated in a) is the increase in amplitude after each spike (facilitation). Illustrated in b) is the decrease in amplitude after each spike (depression).

Another form of plasticity of particular interest is called *spike frequency adaptation*.

When a neuron receives a constant current pulse from an *in vitro* experiment of sufficient duration, certain neurons' responses will "adapt" (cf. Figure 5). Adaptation is the phenomenon which causes a decrease in the spike rate as a function of time, and is also believed to be related to the learning behavior of neurons. This form of desensitization may be related to the transmitter receptors' responses during prolonged or repeated stimulus.

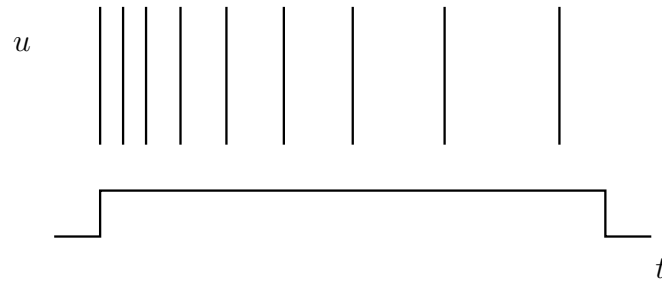


Figure 5. Shows a response which adapts to a constant current input. This adaptation is a decrease in spike rate as a function of time. The voltage of the membrane potential u is plotted as a function of time t over the constant current pulse.

Synaptic Model Formulation

Because of synaptic plasticity alone, the net synaptic input to the soma of a neuron can be difficult to describe. More generally, individual synapses not only have different physiology, but will also behave differently to every presynaptic input. Thus, formulating a model for $I(t)$ in (1.1) can be complicated. In this section, a general description of $I(t)$ is given and a simple Hodgkin-Huxley synaptic model is used to postulate potential “shapes” for the net synaptic input $I(t)$.

For a single synapse located at a position x on the dendritic tree, the current felt at the soma may be modeled as

$$I_{syn} = g_{syn}(t)(V(t) - V_s), \quad (2.1)$$

where g_{syn} is the conductance between the synapse location and the soma and V_s is the local postsynaptic potential. Adopting Rall’s equivalent cylinder approach [65, 66], this conductance depends on the synapse location and the morphology of the dendritic tree, and for simplicity, we assume $g_{syn}(t)$ is constant, i.e., $g_{syn}(t) = \bar{g}_{syn}$. If the distribution of

synapses is idealized as a continuum over the cell's dendritic tree or *synaptic field* Ω_s , the net synaptic current felt at the soma can be modeled by

$$I(t) = \int_{\Omega_s} \rho(\mathbf{x}) \bar{g}_{syn}(\mathbf{x}) (V(t) - V_s(\mathbf{x}, t)) d\mathbf{x}, \quad (2.2)$$

where $\rho(\mathbf{x})$ is the density of synapses at location \mathbf{x} . Since the synapses are divided into excitatory (+) and inhibitory (-) populations, the current $I(t)$ can be split into the net somal currents from each of these populations, i.e.,

$$I(t) = I_+(t) + I_-(t), \quad (2.3)$$

where each of ρ , \bar{g}_{syn} and V_s in (2.2) inherit additional superscripts as in ρ^+ , \bar{g}_{syn}^+ and V_s^+ for the excitatory current, for instance.

In general, the current balance equation for the postsynaptic membrane potential V_s of a synapse with two types of channels can be written as

$$C_m \frac{dV_s}{dt} = -g_r(V_s - V_r) - g_n(V_s - V_n) \quad (2.4)$$

where C_m is the net synaptic capacitance, $g_n(V_s - V_n)$ represents the effects of the neurotransmitter dependent currents, and the effects of all other ionic channels are incorporated in the term $g_r(V_s - V_r)$ (from [45] and [47]). In (2.4), V_r and g_r summarize the resting potential and resting conductance of the transmitter independent channels respectively, V_n is the reversal potential for the transmitter dependent channels with a conductance g_n which is neurotransmitter concentration dependent. For example, acetylcholine (ACh) transmitters cause ACh receptors to open and close according to the concentration of ACh in the

synaptic membrane and thus affects the ionic current. More generally, action potentials at presynaptic cells release neurotransmitters which may bind to some channels at the postsynaptic receiving cell. Since the conductance g_n depends on the concentration of these transmitters, some models assume a time dependent conductance $g_n = g_n(t)$. In the following synaptic model, the term $g_n(V_s - V_n)$ is viewed to be simply a function of time represented by $i(t)$. Thus, for a synapse with (1) a voltage-gated receptor independent channel and (2) a receptor time dependent channel, the evolution of V_s in (2.2) can be modeled by

$$C_s \frac{dV_s}{dt} = -\bar{g}_r n (V_s - V_r) + i(t), \quad (2.5)$$

$$\frac{dn}{dt} = \frac{n_\infty(V_s) - n}{\tau_n}, \quad (2.6)$$

where n is the gating variable for the receptor independent channel, and \bar{g}_r is its maximal conductance. If $i(t) > 0$ the synapse is excitatory whereas if $i(t) < 0$ the synapse is inhibitory. Furthermore, if the time constant τ_n is small, the postsynaptic potential equilibrates very quickly. Such synapses will be referred to as “fast”. Similarly, if τ_n is large, the synapse is “slow” due to a slowly equilibrating PSP.

Since postsynaptic potentials are small in magnitude, a linear approximation of (2.5)-(2.6) about its equilibria $(v^*, n^*) = (V_r, n_\infty(v^*))$ can be used to study changes in PSPs. Letting $v_l = v - v^*$ and $n_l = n - n^*$, the linearized system for (v_l, n_l) is decoupled. The resulting equation for v_l is

$$\frac{dv_l}{dt} = -\lambda v_l + i(t), \quad v_l(0) = 0 \quad (2.7)$$

where v_l is the linearized synaptic potential, and λ is a constant.

Now, consider a solution resulting from N presynaptic action potentials each separated by time Δt . For such an input, the neurotransmitter dependent current can be modeled by

$$i(t) = \alpha \sum_{k=1}^N \delta(t - k\Delta t) \quad (2.8)$$

where $\delta(t)$ is the delta function and $\alpha > 0$ (excitatory) is chosen to be constant.

The solution to (2.7) can be computed using Laplace transforms and is given by

$$v_l(t) = \alpha \sum_{k=1}^N H(t - k\Delta t) e^{-\lambda(t-k\Delta t)} \quad (2.9)$$

where $H(t)$ is the Heaviside function. The solution in (2.9) can be interpolated by:

$$\bar{v}_l(t) = \begin{cases} \frac{\alpha}{e^{-\lambda\Delta t} - 1} (e^{-\lambda t} - 1) & \text{if } t \leq N\Delta t \\ \beta e^{-\lambda t} & \text{if } t > N\Delta t \end{cases} \quad (2.10)$$

where $\beta = \alpha \sum_{k=1}^N e^{\lambda k\Delta t}$, to generalize the behavior of the PSP for this type of model. In Figure 6, the interpolation (2.10) is superimposed on the true solution (2.9) to show two distinct behaviors. Figure 6a) shows a synaptic model which is “slow” to activate and “slow” to inactivate (equilibrates slowly). By varying the model parameters ($\alpha, \lambda, \Delta t$), Figure 6b) shows a synaptic model which is “fast” to activate and “fast” to inactivate (equilibrates quickly).

Notice that the model above does not account for any effects of plasticity. To include plasticity such as facilitation or depression, α could be made k -dependent. To incorporate facilitation in the synaptic model above, $\alpha(k)$ of the form illustrated in Figure 7a) is considered. Similarly, to incorporate the effects of synaptic depression, $\alpha(k)$ is assumed to

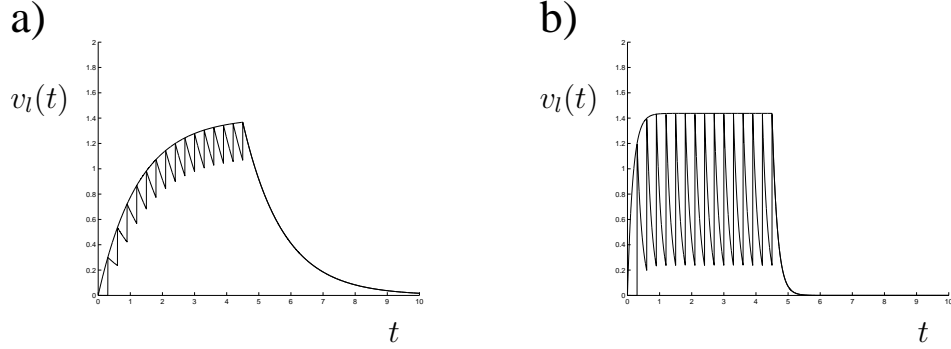


Figure 6. Shows the solution to the linearized synaptic model with a spike train input $i(t)$ (with 15 spikes). In each figure an interpolation (2.10) is superimposed on the true solution (2.9). Two different parameter sets $(\alpha, \lambda, \Delta t)$ were used. a) shows a synaptic channel which is “slow” to activate and “slow” to inactivate corresponding to parameters (1.2,6,0.3). This behavior will be referred to as “slow” On and “slow” Off. b) shows a synaptic channel which is “fast” to activate and “fast” to inactivate corresponding to parameters (0.3,0.8,0.3). This behavior will be referred to as “fast” On and “fast” Off.

have a form similar to that illustrated in Figure 7b). The solution to (2.7) when

$$i(t) = \sum_{k=1}^N \alpha(k) \delta(t - k\Delta t) \quad (2.11)$$

is given by

$$v_l(t) = \sum_{k=1}^N \alpha(k) H(t - k\Delta t) e^{-\lambda(t-k\Delta t)}. \quad (2.12)$$

When $\alpha(k)$ is made to incorporate the effects of facilitation, a solution of (2.12) is illustrated in Figure 8a). Illustrated in Figure 8b) is (2.12) when the effects of depression are considered. The resulting solution illustrated in Figure 8b) is very similar to the result found in Figure 8a) of [79]. In [79], *in vitro* recordings of rat visual neurons were used to illustrate the effects of synaptic depression on PSPs. This fact suggests that the assumptions of the model are reasonable and can be used to explain post-synaptic potentials.

Since $I(t)$ in (2.2) depends linearly on V_s , $I(t)$ will inherit some of the aforementioned

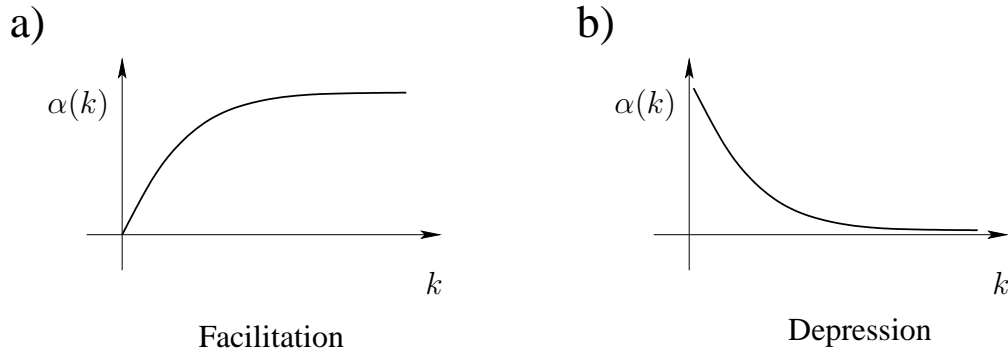


Figure 7. The k -dependent functions for facilitation and depression, shown in a) and b) respectively.

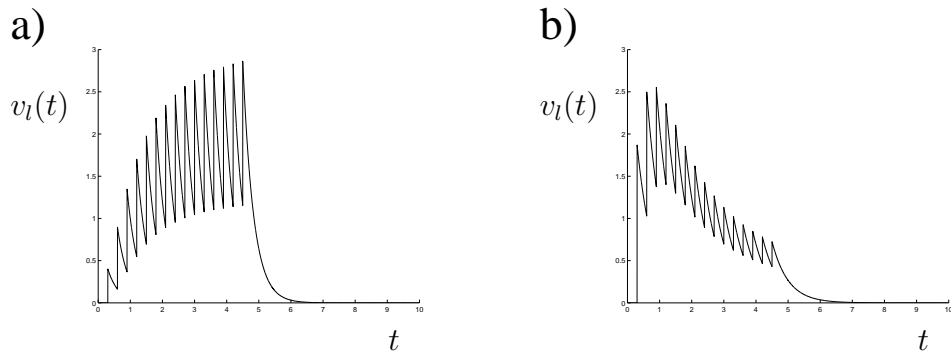


Figure 8. Shows the solution to the linearized synaptic model with an k -dependent amplitude function $\alpha(k)$ to incorporate the effects of synaptic facilitation and depression. In a) the solution to (2.12) is shown with $\alpha(k) = \arctan(k/3)$ (facilitation), and the parameter set $(\alpha, \lambda, \Delta t) = (1.25, 3, 0.3)$. In b) the solution to (2.12) is shown with $\alpha(k) = -\arctan(k/3) + \pi/2$ (depression), and the parameter set $(1.25, 2, 0.3)$.

dynamics of the linearized synaptic model. For instance, were the synaptic input to the cell purely excitatory and $\tau_n \ll 1$, then $I_+(t)$ could have a shape similar to that in Figure 6b).

Alternately, were $\tau_n \gg 1$ for purely inhibitory inputs, $|I_-(t)|$ could have a shape similar to that in Figure 6a). The exact correlation between such excitatory and inhibitory inputs and their respective postsynaptic potentials V_s would in reality depend on dendritic morphology.

However, we will assume that the net synaptic input to the soma will also have these shapes.

The synaptic model described by (2.5)-(2.6) with varying plasticity assumptions, provides a simple way to generate different possible synaptic inputs that may be felt at the soma (as in Figure 6 and Figure 8). However, the synaptic model (2.5)-(2.6) is one of many possible synaptic models. For instance, the addition of other postsynaptic channels could alter the linearized response to inputs such as those in (2.8). Also, since each synapse has a different location \mathbf{x} in the cell's synaptic field Ω_s , the parameters which define (2.5)-(2.6) are most generally functions of \mathbf{x} as well. Moreover, within each of the excitatory and inhibitory synaptic populations all of these parameters can be viewed as constant, with one notable exception. The current $i = i(\mathbf{x}, t)$ is a function of \mathbf{x} since different synapses may have different inputs depending on a given stimulus.

In general, synapses will have many dynamics other than those produced by (2.5)-(2.6) but incorporating them into a model may be difficult. For example, synaptic "spill over" can affect the transmission at other synapses in a neighborhood, but is not fully understood and thus difficult to include in modeling. Plasticity has been shown to play a major role in synaptic dynamics but may also be difficult to incorporate in a model. Even though these issues complicate modeling aspects, they may nevertheless be paramount for a more complete understanding of visual system responses. Models such as ones found in [8, 9], include terms related to the physiology of synapses, and address some aspects of plasticity. Instead of a detailed synaptic model incorporating plasticity and other dynamics to model PSPs, we give a general description of some different types of possible net synaptic inputs.

These different types (shapes) of inputs can incorporate any of the effects of plasticity and other synaptic dynamics such as fast and slow mechanisms.

In Table 1 are some different types of *generalized* net synaptic inputs, $|I(t)|$, which can be incorporated into a single cell model. The general shapes of these inputs have been characterized by their activation and inactivation behaviors. Also included with these shapes are the time courses of a presynaptic stimulus input (or applied current). For example, included in rows 1 and 4 in Table 1 are the dynamics generalized from the interpolation function (2.10) and the time course of a presynaptic current (given by the bar). When facilitation is incorporated into the activation of the synapses as in Figure 8, then the general shape of $I(t)$ may be similar to those found on rows 5-7 in Table 1 (cf. Figure 8a)). Similarly, were the effects of depression incorporated into activation, $I(t)$ may be similar in shape to that illustrated in row 8 of Table 1 (cf. Figure 8b)). Row 7 of Table 1 shows the general shape for a net synaptic current which incorporates both facilitation and depression. Notice that the effects of facilitation are immediate and the effects of depression are felt slightly later.

These general shapes will be used to reproduce the responses illustrated in Figures 1 and 2. For purposes of modeling, “fast” activation or inactivation is idealized with a Heaviside function. In (FULL), a sufficiently large net excitatory synaptic input will be shown to cause the *On* response in Figure 1a). Likewise, a sufficiently large inhibitory input (of sufficient duration) will be shown to cause the *Off* response in Figure 1b) (PIR response).

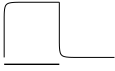
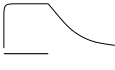
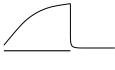
Row	Net Postsynaptic Current $ I(t) $	Plasticity Assumption	General Description
1		None	Fast On, Fast Off
2		None	Fast On, Slow Off
3		None	Slow On, Fast Off
4		None	Slow On, Slow Off
5		Facilitation	Facilitation On, Fast Off
6		Facilitation	Facilitation On, Slow Off
7		Facilitation and Depression	Facilitation and Depression On
8		Depression	Depression On, Fast Off

Table 1. A description of the possible net synaptic current responses given a presynaptic input (or visual stimulus). In the second column the bar under each shape represents the duration of a presynaptic input (or visual stimulus).

Extracellular measurements made on retinal ganglion cells by [51] also reproduce the diminished excitatory and PIR responses when two simultaneous stimuli are presented as illustrated in Figure 1c). To reproduce these nonlinearities, excitatory synapses are assumed to be fast relative to the inhibitory synaptic inputs. This relationship will be explained in further detail in Chapter 5.

Single Cell Model

With the preceding synaptic model development and description of existing models, a three variable phenomenological model is presented. Ideally, a neuron model should have terms which relate to a Hodgkin-Huxley equation of the form (1.5) and include all possible dynamics already described in this study. Realistically, in order to have a model be amenable to analysis, many of the dynamics must be simplified (such as synaptic input). The Pernarowski polynomial model (1994) [59, 60] is such a model and will be a basis for modeling in this study. This model was first used to model bursting pancreatic β -cells and has been adapted here to model neurons (specifically, visual neurons). This model can be made to exhibit bursting and beating (tonic spiking) behaviors; adaptation; and by including synaptic inputs similar in shape as those found in Table 1, can reproduce the responses illustrated in Figures 1 and 2.

The model consists of the following set of differential equations:

$$\frac{du}{dt} = f(u) - w - z + I(t) \quad (2.13)$$

$$\frac{dw}{dt} = g(u) - w \quad (2.14)$$

$$\frac{dz}{dt} = \epsilon(h(u) - z) \quad , \quad 0 < \epsilon \ll 1 \quad , \quad (2.15)$$

where the polynomials f , g and h are defined by

$$f(u) = f_3u^3 + f_2u^2 + f_1u \quad , \quad (2.16)$$

$$g(u) = g_3u^3 + g_2u^2 + g_1u + g_0 \quad , \quad (2.17)$$

$$h(u) = \beta(u - \alpha) \quad (2.18)$$

and the polynomial coefficients of f and g are:

$$f_3 = -\frac{a}{3}, f_2 = a\mu, f_1 = 1 - a(\mu^2 - \eta^2),$$

$$g_3 = f_3 + 1, g_2 = f_2, g_1 = f_1 - 3, g_0 = -3.$$

Here, $\lambda_s = (\alpha, \beta)$ and $\lambda_f = (a, \eta, \mu)$ are the “slow” and “fast” parameters, respectively. In the model (2.13)-(2.15), u is the transmembrane somal voltage, $f(u)$ and w are fast currents (analagous to sodium and potassium currents), z is a slow current (analagous to calcium currents found in [52]), and $I(t)$ is the net synaptic current integrated over the synaptic field. For purposes of reference, equations (2.13)-(2.15) will be referred to as (FULL).

The complicated form of the polynomials f and g is due in part to their derivation from a Liénard form in [60]. In the Liénard form, much work has been done in classifying the various fast-subsystem (FS) ($\epsilon = 0$) bifurcation structures [20, 59] as previously mentioned. This body of work is used here in choosing appropriate “fast” parameter sets $\lambda_f = (a, \eta, \mu)$ so that (FULL) exhibits bursting.

This phenomenological model can be characterized as “Hodgkin-Huxley” in nature. Consider a Hodgkin-Huxley equation with a slow current of the form

$$C_m \frac{dv}{dt} = - \sum_x I_{fx} - \bar{g}_z z (v - v_z) \quad (2.19)$$

where v is the membrane potential, I_{fx} represents fast currents of type x , and $\bar{g}_z z (v - v_z)$ is the slow current. Then, for $v > v_z$, (2.19) can be written as

$$\frac{C_m}{\bar{g}_z (v - v_z)} \frac{dv}{dt} = - \sum_{fx} I_{fx}^* - z \quad (2.20)$$

Defining $u = \ln(v - v_z)$, then using

$$\frac{du}{dt} = \frac{1}{v - v_z} \frac{dv}{dt}, \quad (2.21)$$

equation (2.20) can be written in the form

$$\frac{C_m}{\bar{g}_z} \frac{du}{dt} = - \sum_{fx} I_{fx}^* - z. \quad (2.22)$$

If the membrane potential v , time, and the channel conductance are nondimensionalized, then (2.20) can be written as

$$\frac{du}{d\tau} = - \sum_{fx} I_{fx}^* - z, \quad (2.23)$$

with corresponding equation

$$\frac{dz}{d\tau} = \frac{z_\infty(u) - z}{\tau_z(u)}, \quad (2.24)$$

for the slow channel gating variable. Under this transformation, u retains all the monotonicity properties of the biophysical voltage v . Also, (2.23), like (2.13) is linear in the gating variable z , and when $\tau_z(u)$ in (2.24) is close to a constant it has the same form as (2.15). Thus, (FULL) provides a reasonable model for examining the qualitative behaviors of many Hodgkin-Huxley type models.

Before this model is analyzed, we give numerical solutions of the temporal traces of the “voltage” $u(t)$ which reproduce (for certain stimuli) the behaviors illustrated in Figure 1. For instance, Figure 9 reproduces the *On* and *Off* responses illustrated in Figures 1a)-b). The response in Figure 1c) will be examined in a Chapters 4 and 5. These numerical solutions were computed using an explicit one step Runge-Kutta integration method in XPPAUT [23]. Many of the proceeding figures will also be generated using XPPAUT.

In Figure 9, the net synaptic input current

$$I(t) = \bar{I} (H(t - t_0) - H(t - t_0 - T)) \quad (2.25)$$

is superimposed over the voltage $u(t)$. This type of input corresponds to a constant current pulse which one would generate during *in vitro* experiments. Here, \bar{I} is the current amplitude, t_0 is the starting time of the pulse, T is the duration, and $H(t)$ is the Heaviside function. This constant current pulse also represents an idealized “fast” On and “fast” Off type of net synaptic input (cf. Figure 6 and Row 1 in Table 1). Figure 9a) simulates the experiment where a stimulus is given in the *Plus* part of the cell’s receptive field. Figure 9b) on the other hand, simulates the experiment where a stimulus is given in the *Minus* part of the cell’s receptive field.

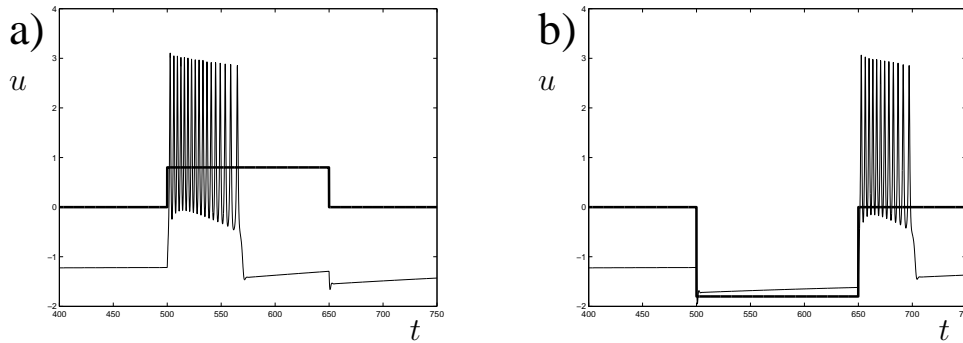


Figure 9. Shows typical *On* and *Off* responses in the model (FULL) with the constant current stimuli $I(t)$ superimposed on each figure. The (FS) parameter set $\lambda_f = (a, \eta, \mu)$ was chosen as $\lambda_f = (0.25, 0.75, 1.5)$ with a current amplitude $\bar{I} = +0.8$ and $\bar{I} = -1.8$ for the *On* and *Off* responses, respectively. In both, the slow parameters $\lambda_s = (\alpha, \beta) = (-1.5, 4)$ and $\epsilon = 0.0025$. In each figure, $t_0 = 500$ and $T = 150$. The numerical traces in this figure were generated using XPPAUT [23].

In order to generate the responses in Figure 9, certain stimuli amplitudes \bar{I} and durations T must be used. To determine such appropriate values for \bar{I} and T , we will present certain model definitions and terminology. These definitions are included in the next chapter and will be used throughout the remainder of this study.

In this chapter, the non-autonomous model (FULL) was developed. To reproduce the responses illustrated in Figure 1, it has been established that PIR and bursting play an important role. These dynamics were incorporated into a single cell phenomenological model by adapting the Pernarowski model and including a synaptic input term. Since the single cell model used in this study incorporates a time-dependent synaptic input, relevant synaptic mechanisms were discussed (such as activation/inactivation, and plasticity). By including these mechanisms, a simple synaptic model was used to postulate various general shapes of net synaptic input to the cell. Lastly, (FULL) was shown to reproduce the *On* and *Off* responses when two distinct synaptic inputs were used.

CHAPTER 3

SUBSYSTEM DERIVATION AND DEFINITION

The main goal of this study is to understand and explain the dynamics of (FULL) when a time dependent input $I(t)$ is used. Since (FULL) is a non-autonomous bursting model, $I(t)$ can play a major role in the evolution of the numerical traces of $u(t)$. In this chapter, we give the basic definitions and terminology needed to describe these traces. For example, the traces illustrated in Figure 9 have been generated by a stimulus $I(t)$ of the form found in (2.25) and will be described in detail in the next chapter. Before a description of these traces is given, the fast-subsystem (FS), the slow-subsystem (SS), and the averaged-fast-subsystem (AFS) are defined. In this chapter (and in the next), the definitions of the subsystems assume a constant current pulse input $I(t)$. When this type of input is incorporated, $I(t)$ can simply be viewed as being constant during the pulse. The rapid transitions (at $t = t_0$ and $t = t_0 + T$) for such a pulse will play an important role in the description of the dynamics of the model. Therefore, for inputs $I(t)$ which have rapid transitions such as those found in rows 1 (activation/inactivation), 2 (activation), 3 (inactivation), 5 (inactivation), and 8 (inactivation) in Table 1, the basin of attraction for the periodic orbits and equilibria of the fast-subsystem will be discussed and defined accordingly. In later analyses, this will be shown to have great impact on the solutions. Most of the following subsystem definitions have been studied extensively and are mainly

included here for completeness.

In addition to understanding the dynamics of (FULL), a goal of this study is to model the responses of neurons. Since (FULL) can generate many types of responses, some will not have physiological meanings. In this regard, there is a distinction between the dynamics of (FULL) and the reasonable parameter or variable ranges when modeling neurons. When applicable, this distinction will be discussed and described. Often, the dynamics of (FULL) will include many behaviors which may be unrealistic for neurons. The understanding of the dynamics is crucial when using (FULL) to model neurons.

Fast-Subsystem

When a constant current pulse is applied, different amplitudes and durations will cause different responses. To understand what types of amplitudes and durations can cause *On* and *Off* responses, it is necessary to understand how the fast-subsystem (FS) of (FULL) depends on the constant \bar{I} in (2.25). Here (FS) is obtained by setting $\epsilon = 0$ in (FULL):

$$\frac{du}{dt} = f(u) - w - z + \bar{I}, \quad (3.1)$$

$$\frac{dw}{dt} = g(u) - w, \quad (3.2)$$

where both z and \bar{I} are treated as parameters. By introducing the bifurcation parameter $\gamma = z - \bar{I}$, the (FS) bifurcation diagram in Figure 10a) is generated. In this figure u is plotted against γ . The *Z*-shaped curve, given by

$$\gamma = G(u) \equiv f(u) - g(u) = -u^3 + 3u + 3, \quad (3.3)$$

is the projection of the equilibria of (3.1)-(3.2) onto the (γ, u) -plane. Note that despite the fact that both f and g depend on the fast parameter set $\lambda_f = (a, \eta, \mu)$, G does not. The solid regions of this curve represent stable equilibria. The dashed region represents unstable equilibria. Also labeled in Figure 10a) are the γ values γ_- and γ_+ corresponding to the lower and upper saddle-node bifurcations, respectively. Using this labeling scheme, notice that the lower and upper saddle-node bifurcations of (FS) will have the coordinates given by $(u_-, G(u_-))$ and $(u_+, G(u_+))$ at γ_- and γ_+ , respectively. On the upper region of the Z-shaped curve, the stability of the equilibria changes at the Hopf bifurcation point labeled $\gamma = \gamma_{hb}$. The periodic orbits emanating from this Hopf point terminate at a homoclinic bifurcation at $\gamma = \gamma_{hc}$. Thus, for $\gamma \in (\gamma_{hb}, \gamma_{hc})$ the (FS) has stable $T_p(\gamma)$ -periodic limit cycles

$$\Omega_p(t, \gamma) = (u, w) = (\Omega_1(t, \gamma), \Omega_2(t, \gamma)). \quad (3.4)$$

Analytical results of the aforementioned bifurcations computed in Figure 10 with XP-PAUT can be found in [59]. For λ_f as chosen in Figure 10a), notice that when $\gamma \in (\gamma_-, \gamma_{hc})$, (FS) has a region of bistability where both a lower branch equilibria and periodic orbits co-exist.

Also found in [59] is a detailed description of the dynamics of (FULL) when the parameters of λ_f are chosen differently. For example, the different oscillatory behaviors illustrated in Figure 3 arise by choosing different values of η and μ . Illustrated in Figure 10b) is the bifurcation diagram when $\eta = 0.9$ and $\mu = 1.5$ (as opposed to $\eta = 0.75$ and $\mu = 1.5$ for Figure 10a)). In this figure the homoclinic bifurcation occurs near (or at)

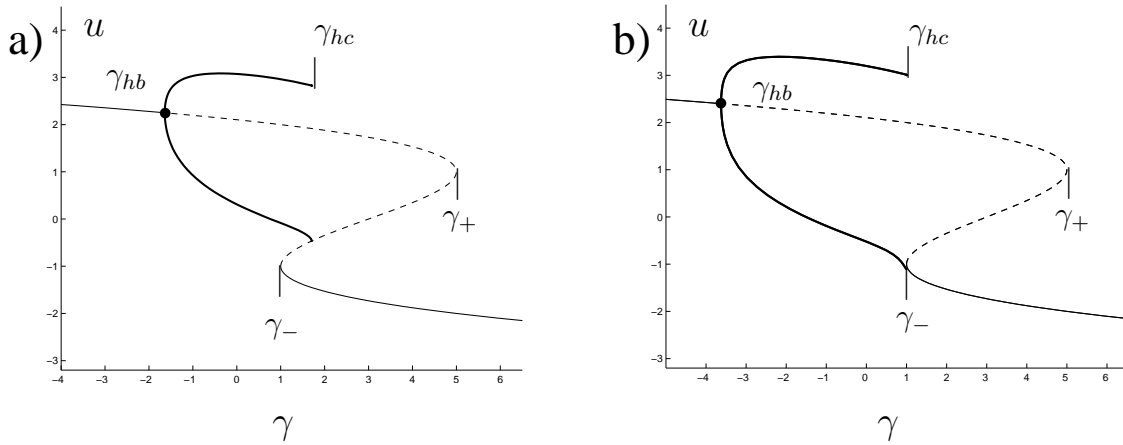


Figure 10. Fast-subsystem bifurcation diagrams for (3.1)-(3.2). Labeled are the Hopf point γ_{hb} , the homoclinic value γ_{hc} , the right most saddle node bifurcation value γ_+ , and the left most saddle node bifurcation value γ_- . In figure a) the fast parameter set was chosen as $\lambda_f = (a, \eta, \mu) = (0.25, 0.75, 1.5)$. Notice that for this choice of λ_f , (FS) has a region of bistability for $\gamma \in (\gamma_-, \gamma_{hc})$. In figure b) the fast parameter set was chosen as $\lambda_f = (a, \eta, \mu) = (0.25, 0.9, 1.5)$. For this choice of fast parameters, the bifurcation structure does not have a region of bistability.

the lower saddle-node bifurcation. Thus, for this choice of fast parameters, (FS) does not have a region of bistability and (FULL) will not undergo a bursting cycle. When the fast subsystem has this type of bifurcation structure, the solution of (FULL) will exhibit beating patterns (fast spiking) as illustrated in Figure 3 (upper right figure).

When modeling neurons that exhibit *On* and *Off* responses as illustrated in Chapter 2, choosing fast parameters so that (FS) has a bifurcation structure which has a region of bistability is important (since the responses are assumed to be short duration bursts). Although bursting is an important feature, many neurons will not burst but will undergo different oscillatory behaviors. For modeling such neurons, it is sometimes possible to alter the fast

parameter set to obtain a (FS) with a desirable bifurcation structure. Since changing the bifurcation structure can be done by simply choosing a different fast parameter set, this gives another reason for choosing this particular set of equations to model visual neurons (or neurons in general). Although other bifurcation structures are important when modeling neurons, most of the modeling and analyses in this study will be based on a fast parameter set λ_f which exhibits square-wave bursting (as in Figure 10a)). This particular choice of λ_f was used to match experimental results illustrated in [14].

For the fast parameter set used to generate the bifurcation diagram illustrated in Figure 10a), recall that the lower branch equilibria of (FS) forms a stable manifold for the fast dynamics. When describing various solutions of (FULL), parts of the solutions of (FULL) will travel near the stable lower branch manifold \mathbb{S}_L of (FS) defined as:

$$\mathbb{S}_L = \{(u, w, \gamma) : \gamma = G(u), w = g(u), u < u_-\}. \quad (3.5)$$

The projection S_L of \mathbb{S}_L onto the (γ, u) -plane is defined as:

$$S_L = \{(u, \gamma) : \gamma = G(u), u < u_-\}. \quad (3.6)$$

Using this projection will make it easier to visualize the trajectories of the solution. Similarly, we define both the middle branch \mathbb{S}_M of (FS) and the upper branch \mathbb{S}_U of (FS) respectively as:

$$\mathbb{S}_M = \{(u, w, \gamma) : \gamma = G(u), w = g(u), u_- < u < u_+\}, \quad (3.7)$$

$$\mathbb{S}_U = \{(u, w, \gamma) : \gamma = G(u), w = g(u), u_+ < u\}, \quad (3.8)$$

with associated projections S_M and S_U .

These manifolds will be needed to discuss solutions of and the location of equilibria of (FULL). For example, a solution which goes through a burst cycle will typically go through an “active phase” and a “silent phase”. During the active phase, solutions of (FULL) travel near the periodic orbits Ω_p of (FS) while in the silent phase they travel near \mathbb{S}_L .

Slow-Subsystem

The slow-subsystem (SS) describes the slow flow of the trajectories of (FULL) along (or near) \mathbb{S}_L . Again (as in (FS)), (SS) is defined in terms of the constant \bar{I} . Using a slow time transformation $\tau = \epsilon t$ in (FULL) gives the following system:

$$\epsilon \frac{du}{d\tau} = f(u) - w - z + \bar{I}, \quad (3.9)$$

$$\epsilon \frac{dw}{d\tau} = g(u) - w, \quad (3.10)$$

$$\frac{dz}{d\tau} = h(u) - z, \quad (3.11)$$

Letting $\epsilon = 0$ and using the substitution $\gamma = z - \bar{I}$, the slow-subsystem (SS) is given by:

$$\gamma = f(u) - w, \quad (3.12)$$

$$w = g(u), \quad (3.13)$$

$$\frac{d\gamma}{d\tau} = h(u) - (\gamma + \bar{I}). \quad (3.14)$$

For the purposes of this study, (SS) is defined as (3.12)-(3.14) for $u < u_-$. Solutions of (SS) give trajectories on \mathbb{S}_L which are the leading order approximations to the silent phase of (FULL).

Notice we combine equations (3.12) and (3.13) to give the following algebraic condition which must be satisfied when the flow remains on \mathbb{S}_L :

$$\gamma = G(u) = -u^3 + 3u + 3. \quad (3.15)$$

Using a trigonometric form of the cubic root formula, the lower branch root $u_{LB}(\gamma)$ can be found as

$$u = u_{LB}(\gamma) = \begin{cases} 2 \cos \left(\frac{1}{3} \arccos \left(\frac{3-\gamma}{2} \right) + \frac{2\pi}{3} \right), & 1 \leq \gamma \leq 5, \\ -2 \cosh \left(\frac{1}{3} \ln \left(\frac{\gamma-3}{2} + \sqrt{\left(\frac{\gamma-3}{2} \right)^2 - 1} \right) \right), & \gamma > 5. \end{cases} \quad (3.16)$$

This allows one to rewrite (3.14) as,

$$\frac{d\gamma}{d\tau} = H_1(\gamma) = h(u_{LB}(\gamma)) - (\gamma + \bar{I}). \quad (3.17)$$

This equation will be used to describe the silent phase and to determine minimum durations of a constant current pulse that will cause an *Off* response.

The evolution of the solution along \mathbb{S}_L is referred to as the silent phase of the cycle. For the purpose of this study, the duration of the silent phase is defined as the time it takes for the solution to travel along \mathbb{S}_L from an entry point γ_{in}^s to an exit point γ_{out}^s . If a solution has more than one burst cycle then it is possible that the solution will travel along \mathbb{S}_L more than once. When this happens, the silent phase durations can simply be indexed by the number of occurrences (cf. Figure 17d)). Since (3.17) gives the leading order evolution of (FULL) along \mathbb{S}_L , it can be used to determine the silent phase duration. Separating and integrating (3.17) over $(\gamma_{in}^s, \gamma_{out}^s)$ gives the silent phase duration

$$T_{SP} = T_{SP}(\gamma_{in}^s, \gamma_{out}^s) = \int_{\gamma_{in}^s}^{\gamma_{out}^s} \frac{d\gamma}{h(u_{LB}(\gamma)) - (\gamma + \bar{I})}. \quad (3.18)$$

This equation will be used to describe the duration T needed when applying a constant current pulse which guarantees an *Off* response (as illustrated in Figure 9b)). Notice that the silent phase duration as defined by (3.18), depends on the values γ_{in}^s and γ_{out}^s . Therefore, the silent phase duration may be different for every pair $(\gamma_{in}^s, \gamma_{out}^s)$.

The parameters which govern (SS) are given by the slow parameter set $\lambda_s = (\alpha, \beta)$. Using the definition of $h(u)$ in (2.18), the nullcline for (2.15), is given by

$$h(u) = z = \gamma + \bar{I}.$$

Illustrated in Figure 11 are (FS) and the $\dot{\gamma} = 0$ line with a bursting solution superimposed (with $\bar{I} = 0$). To illustrate a bursting solution, λ_s was chosen so that $\dot{\gamma} = 0$ intersects (3.3) on S_M , and $\beta > 0$. Notice that when $\beta > 0$, $\dot{\gamma} < 0$ below the nullcline and $\dot{\gamma} > 0$ above the nullcline. In this situation, the solution travels to the right along the periodic orbits. Once the solution reaches the homoclinic point a rapid transition back to S_L occurs. Once on S_L , the solution is below the γ -nullcline and will travel back to the left towards the lower saddle node. Even though a complete description of the cycle is not given here, a detailed description of the solution cycles illustrated in Figure 9 is given in Chapter 4.

Averaged-Fast-Subsystem

In order to describe the traces of the solutions of (FULL) in the active phase, the averaged-fast-subsystem will be used. In this section the averaged-fast-subsystem (AFS) is defined and an outline of how one derives a leading-order value for the active phase duration is given. We incorporate the previous works in [32] and [61], where the method of

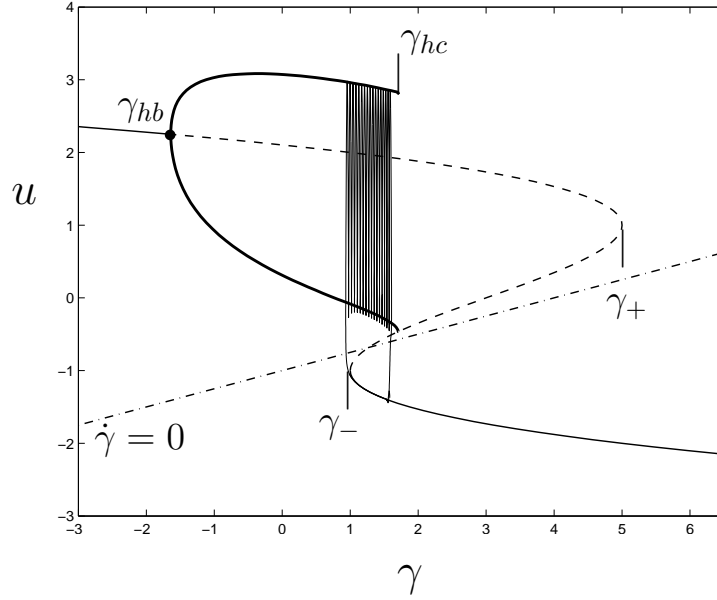


Figure 11. Fast-subsystem bifurcation diagram for (3.1)-(3.2) with fast parameter set $(a, \eta, \mu) = (0.25, 0.75, 1.5)$. Superimposed on (FS) are the $\dot{\gamma} = 0$ line and a bursting solution. In this figure, the slow parameter set was chosen as $(\alpha, \beta) = (-1, 4)$.

averaging has been used to approximate the active phase of bursting cycles. First recall that (FS) has a one-parameter family of $T_p(\gamma)$ -periodic limit cycles $\Omega_p(t, \gamma) = (u, w) = (\Omega_1(t, \gamma), \Omega_2(t, \gamma))$ for $\gamma \in (\gamma_{hb}, \gamma_{hc})$. The averaged-fast-subsystem (AFS) of (FULL) is then obtained by averaging the vector field of the slow variables in t over these limit cycles.

To be more specific, for any function $\psi = \psi(u, w)$ the average is defined as

$$\hat{\psi}(\gamma) \equiv \langle \psi(u, w) \rangle = \frac{1}{T_p(\gamma)} \int_0^{T_p(\gamma)} \psi(\Omega_1(t, \gamma), \Omega_2(t, \gamma)) dt. \quad (3.19)$$

Next, define

$$\gamma(t) = z(t) - \bar{I}$$

where \bar{I} is constant. Then, for $t \in (t_0, t_0 + T)$, (FULL) becomes

$$\frac{du}{dt} = f(u) - w - \gamma \quad (3.20)$$

$$\frac{dw}{dt} = g(u) - w \quad (3.21)$$

$$\frac{d\gamma}{dt} = \epsilon(h(u) - (\gamma + \bar{I})), \quad 0 < \epsilon \ll 1, \quad (3.22)$$

In this form, a duplication of the multiple scales averaging method found in [61] is used to derive the (AFS) of (3.20)-(3.22). The resulting (AFS) is

$$\frac{d\gamma}{d\tau} = \langle h(u) \rangle - (\gamma + \bar{I}) \quad (3.23)$$

where $\tau = \epsilon t$ is a slow time. Given the linearity of $h(u)$ in u , (3.23) can be written as

$$\frac{d\gamma}{d\tau} = h(\hat{u}(\gamma)) - (\gamma + \bar{I}), \quad (3.24)$$

where $\hat{u}(\gamma)$ is defined as

$$\hat{u}(\gamma) \equiv \frac{1}{T_p(\gamma)} \int_0^{T_p(\gamma)} \Omega_1(t, \gamma) dt. \quad (3.25)$$

For initial conditions sufficiently close to Ω_p , the solution of (3.24) is the leading order asymptotic approximation of γ for times $\tau = O(1)$ whenever $\gamma \in (\gamma_{hb}, \gamma_{hc})$. Illustrated in Figure 12 is the numerical computation of the average \hat{u} as a function of γ . The average \hat{u} was computed using AUTO [22].

In order to describe the bursting cycle of the solutions of (FULL), the active phase duration is defined. To be specific, the active phase duration T_A is the leading order time for $\gamma(t)$ to increase from its entry point in the active phase γ_{in}^a to its exit point at γ_{out}^a (for

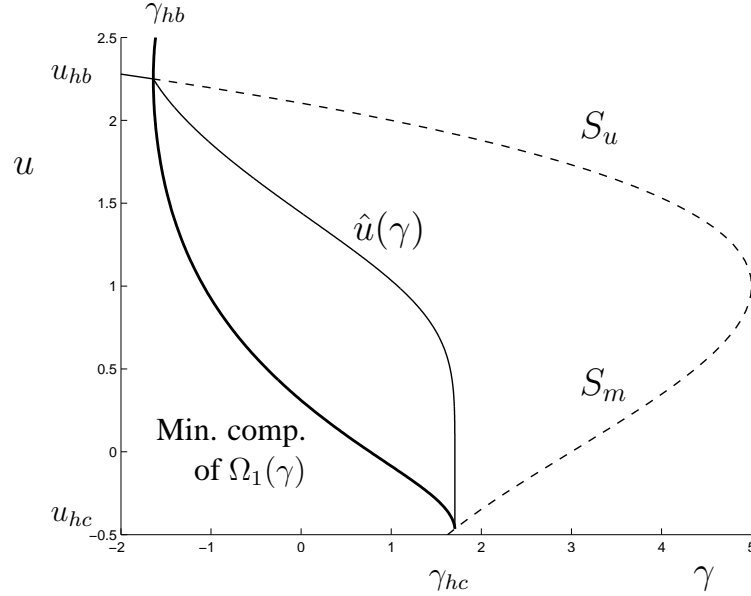


Figure 12. This figure shows $\hat{u}(\gamma)$ for $\gamma \in (\gamma_{hb}, \gamma_{hc})$. Upper and lower branch equilibria S_L , and S_m are also superimposed for reference.

the purposes of this study, it is often the case that $\gamma_{in}^a = \gamma_0$, and $\gamma_{out}^a = \gamma_{hc}$. Thus, in the slow time scale, the active phase duration is found by separating and integrating (3.24):

$$T_A = T_A(\gamma_{in}^a, \gamma_{out}^a) = \int_{\gamma_{in}^a}^{\gamma_{out}^a} \frac{d\gamma}{h(\hat{u}(\gamma)) - (\gamma + \bar{I})}. \quad (3.26)$$

Notice that to compute T_A , the values of \hat{u} illustrated in Figure 12 will be used.

Rapid Transitions, Basin of Attraction

When given a constant current pulse, the bifurcation structure of (FS) will shift rapidly left or right depending on the sign of \bar{I} . When these rapid shifts occur, the trajectories of the solution will also undergo a rapid change. Therefore, it is important to understand where the trajectories go for any initial condition. With this in mind, suppose an initial

condition such as (u_0, w_0, γ_0) is given. For the values of γ_0 which lie in the monostable region of (FS), the solution will undergo a rapid transition to the only stable attractor which occurs for that particular γ -value (either $\mathbb{S}_U, \mathbb{S}_L$, or the periodic orbit on Ω_p). On the other hand, when γ_0 lies in the bistable region, in order to describe the solution in such a case, it is important to know whether the trajectories will be attracted to the stable lower branch \mathbb{S}_L or the stable periodic orbit on Ω_p . In this section, we give the descriptions of the basin of attraction for the equilibria of (FS) which lie on \mathbb{S}_L and the periodic orbit Ω_p . These descriptions are motivated by numerical results, and are explored in this chapter.

Before any numerical tools are used to determine the basins of attraction, we introduce the definitions for the basin of attraction of the equilibria of (FS) and Ω_p . If the trajectories of (FS), starting at (u_0, w_0) , are attracted to a periodic orbit, then the point (u_0, w_0) is said to be in $\mathcal{B}_P(\gamma)$, the basin of attraction of Ω_p . Similarly, if the trajectories of (FS) are attracted to an equilibrium on \mathbb{S}_L , then the initial condition (u_0, w_0) is said to be in $\mathcal{B}_L(\gamma)$, the basin of attraction of the equilibria of (FS) which lie on \mathbb{S}_L . Now that these basins have been defined, a description of how to generate them can be given.

To help describe the basins of attraction, we use the Liénard form of (FULL) derived in [59]. Differentiating (3.20) in t and then eliminating w , equations (3.20) and (3.21) can be written as

$$\ddot{u} + F(u)\dot{u} + G(u, \gamma) = -\epsilon(h(u) - (\gamma + \bar{I})), \quad (3.27)$$

where

$$F(u) = 1 - f'(u),$$

$$G(u, \gamma) = g(u) - f(u) + \gamma.$$

Rewriting (3.27) as a system and letting $\epsilon = 0$, the fast-subsystem in Liénard form is

$$\dot{u} = v, \tag{3.28}$$

$$\dot{v} = -F(u)v - G(u, \gamma). \tag{3.29}$$

When (FS) is rewritten in this form, the equilibria of (FS) always lie on the $v = 0$ axis. This will be useful for determining particular u_0 -values for which the initial condition, (u_0, w_0) , of (FS) is in the basin of attraction \mathcal{B}_P .

In the bistable region $\gamma \in (\gamma_-, \gamma_{hc})$, recall that (FS) will have three equilibria. Let \bar{u}_l , \bar{u}_m , and \bar{u}_u be the lower (stable), middle (saddle), and upper (unstable) equilibria of (FS), respectively. The stability for these points has been established in [59] and is stated here without further analysis. Depicted in Figure 13 is the stable manifold of the middle saddle point \bar{u}_m . Notice that the stable manifold has been divided into a lower and an upper part labeled \mathcal{W}_S^- and \mathcal{W}_S^+ , respectively. To be specific, \mathcal{W}_S^- is defined as the part of the stable manifold which comes into the saddle from below (the $v = 0$ axis) and \mathcal{W}_S^+ is the part which comes into the saddle from above (the $v = 0$ axis). Thus, the stable manifold of the middle saddle \bar{u}_m is the union $\mathcal{W}_S(\bar{u}_m(\gamma)) = \mathcal{W}_S^-(\gamma) \cup \mathcal{W}_S^+(\gamma)$. In Figure 13, $\mathcal{W}_S(\bar{u}_m(\gamma))$ was generated using XPPAUT.

Figure 13a) shows $\mathcal{W}_S(\bar{u}(\gamma))$ for a range of $u \in (-5.5, 7.5)$ when $\gamma = 1.5$. Figure 13b) shows $\mathcal{W}_S(\bar{u}(\gamma))$ for a range of $u \in (-5, 4)$ where $\gamma = 1.5$. In each figure, given any initial condition (u_0, v_0) in the region between \mathcal{W}_S^+ and \mathcal{W}_S^- , the trajectories of the Liénard

system will be attracted to $\Omega_p(\gamma)$. When (FULL) is used to model visual neurons, the variable u represents voltage, and v represents current. Therefore, for modeling purposes the ranges of u and v illustrated in Figure 13a) are unrealistic since membrane voltage has a physiological bound usually described by action potentials and this is represented by the u -range of the periodic orbits. Although Figure 13a) shows that \mathcal{W}_S can wrap around the periodic orbits (illustrated in Figure 13b) as the dashed orbit), when modeling visual neurons only Figure 13b) will be considered. This figure represents a caricature of the typical stable manifold, for values of γ in the bistable region, for a more realistic modeling range of u and v .

Although analytical results are lacking, the numerical results suggest that for $\gamma \in (\gamma_-, \gamma_{hc})$, \mathcal{W}_S will intersect the $v = 0$ line at at least three points. Here, a definition for these points is given and will be used to determine the basins of attraction. The points u_{S_l} , u_{S_m} , and u_{S_u} are the lower u -value, the middle u -value, and the upper u -value where \mathcal{W}_S intersects the line $v = 0$ respectively. These points have been labeled in Figure 13b) (notice that the two upper u -values where \mathcal{W}_S intersects the line $v = 0$ as illustrated in Figure 13a) have been disregarded as unrealistic transmembrane potentials).

In order to determine the basins of attraction, define the sets; $\mathbb{B}_p = \{(u_0, v_0) : u_0 \in (u_{S_l}, u_{S_m}) \cup (\bar{u}_m, u_{S_u}), v_0 = 0\}$ and $\mathbb{B}_L = \{(u_0, v_0) : u_0 \in (-\infty, u_{S_l}) \cup (u_{S_m}, \bar{u}_m), v_0 = 0\}$. We would like to determine the values of u_{S_l} and u_{S_m} for each $\gamma \in (\gamma_-, \gamma_{hc})$. Once these values are determined, whenever $\gamma_0 \in (\gamma_-, \gamma_{hc})$ and $(u_0, v_0) \in \mathbb{B}_p$ is used as an initial condition, the trajectories of (3.28)-(3.29) will be attracted to the periodic orbits

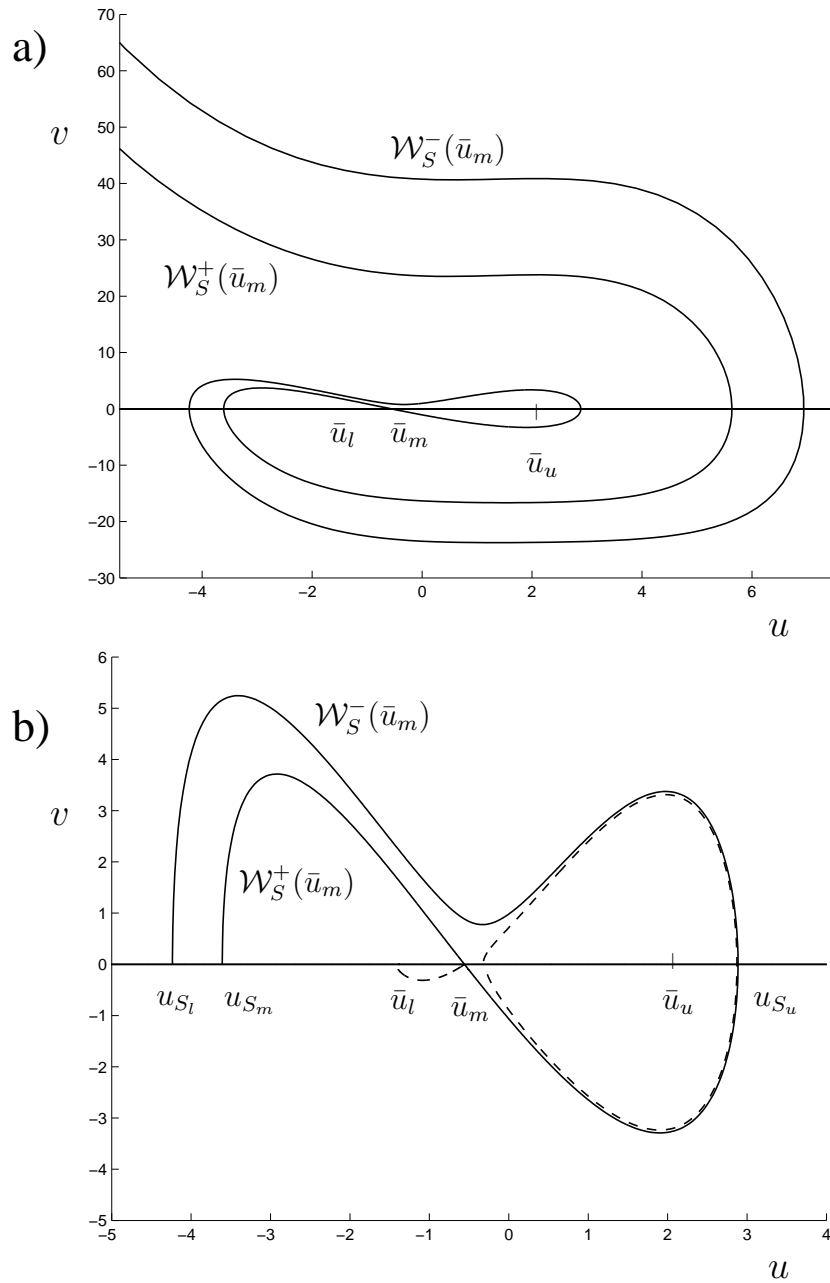


Figure 13. Shows the stable manifold $\mathcal{W}_S(\bar{u}_m(1.5))$ for two different ranges of u . Illustrated in a) is the phase portrait for (3.28)-(3.29) over a larger nonphysical range of u and v . b) illustrates the stable manifolds $\mathcal{W}_S^+(\bar{u}_m)$ and $\mathcal{W}_S^-(\bar{u}_m)$ for $\gamma \in (\gamma_-, \gamma_{hc})$ for a more realistic modeling range. Also illustrated in b) is the unstable manifold $\mathcal{W}_U(\bar{u}_m(1.5))$ and the periodic orbit (dashed curves). Whenever an initial condition, (u_0, v_0) , for (3.28)-(3.29) is chosen to lie between $\mathcal{W}_S^+(\bar{u}_m)$ and $\mathcal{W}_S^-(\bar{u}_m)$, the trajectories will be attracted to the periodic orbits of the Liénard system. Labeled in these figures are the u -values \bar{u}_l , \bar{u}_m , and \bar{u}_u corresponding to the lower (stable), middle (saddle), and upper (unstable) equilibria of (FS), respectively.

of the Liénard system. In contrast, given $\gamma_0 \in (\gamma_-, \gamma_{hc})$, whenever an initial condition $(u_0, v_0) \in \mathbb{B}_L$ is used, the trajectories of (3.28)-(3.29) will be attracted to \bar{u}_l . In order to determine the values u_{S_l} and u_{S_m} , AUTO was used to find numerical solutions for \mathcal{W}_S^+ and \mathcal{W}_S^- for a set of u -values of each γ in the bistable range. To do this, the values u_{S_l} and u_{S_m} were each incorporated into two separate two-point boundary value problems. Each value was then found by solving the boundary value problem for every $\gamma \in (\gamma_-, \gamma_{hc})$. This was done by first solving for \mathcal{W}_S^+ and finding u_{S_m} , then by solving for \mathcal{W}_S^- and finding u_{S_l} . Since both u_{S_m} and u_{S_l} were computed using the same technique, only a description of how u_{S_m} was determined is given here.

To find u_{S_m} , a solution to (3.28)-(3.29) with the following boundary conditions

$$(u(0), v(0)) = (u_{S_m}, 0), \quad (3.30)$$

and

$$\lim_{t \rightarrow \infty} (u(t), v(t)) = (\bar{u}_m, 0), \quad (3.31)$$

must be found. The solution to this problem is the part of \mathcal{W}_S^+ illustrated in Figure 13b), with u_{S_m} as an endpoint.

In order to use AUTO, the boundary condition (3.31) must be on a finite interval. To accommodate this fact, the boundary value problem ((3.28)-(3.29) with boundary conditions (3.30) and (3.31)) was redefined with the following change of variables.

Let $s = \tanh t$, so that $\frac{dt}{ds} = \frac{1}{1-s^2}$ for $-1 < s < 1$. Using this compactification, the

boundary value problem above is redefined as

$$\frac{du}{ds} = \frac{1}{1-s^2}v, \quad (3.32)$$

$$\frac{dv}{ds} = \frac{1}{1-s^2}(-F(u)v - G(u, \gamma)), \quad (3.33)$$

with

$$(u(0), v(0)) = (u_{S_m}, 0), \quad (3.34)$$

and

$$(u(1), v(1)) = (\bar{u}_m, 0). \quad (3.35)$$

To use AUTO to solve this nonautonomous problem, the system must be augmented to turn it into an autonomous system. The augmented system is given by

$$\frac{du}{d\tau} = F_1(u, v, s) = \frac{1}{1-s^2}v, \quad (3.36)$$

$$\frac{dv}{d\tau} = F_2(u, v, s) = \frac{1}{1-s^2}(-F(u)v - G(u, \gamma)), \quad (3.37)$$

$$\frac{ds}{d\tau} = 1, \quad (3.38)$$

with

$$(u(0), v(0), s(0)) = (u_{S_m}, 0, 0) \quad (3.39)$$

and

$$(u(1), v(1), s(1)) = (\bar{u}_m, 0, 1). \quad (3.40)$$

This redefining of the boundary value problem was used instead of using HOMCONT (a subroutine in AUTO) since \mathcal{W}_S^+ from u_{S_m} to \bar{u}_m is neither a homoclinic nor heteroclinic connection. Also note that the vector field of (3.32)-(3.33) appears to be singular in s

as $s \rightarrow 1^-$ (which is carried through to (3.36)-(3.38)). This apparent singularity is not theoretically relevant when computing the stable manifold \mathcal{W}_S , however. For instance, if $(U_s(t), V_s(t))$ is the solution of (3.28)-(3.29) corresponding to \mathcal{W}_S in the t coordinates, $(U_s(t), V_s(t))$ remains bounded as $t \rightarrow \infty$ and approaches the saddle $(\bar{u}_m, 0)$. Thus the associated solution in (3.32)-(3.33), and consequently in (3.36)-(3.38), must be bounded as well as $s \rightarrow 1^-$.

For the system (3.36)-(3.38) with boundary conditions (3.39) and (3.40), an initial solution was computed in XPPAUT. To compute this initial curve, XPPAUT computes the eigenvalues and eigenvectors for \bar{u}_m and uses a shooting method to approximate $\mathcal{W}_S(\bar{u}_m)$. The values of this initial solution were computed for $\gamma = 1.5$, and this data was inserted into AUTO using the command `@fc`. To make sure that AUTO could initialize with this initial solution the endpoints were adjusted to match the boundary values given by (3.39) and (3.40).

First, AUTO was used to compute u_{S_m} for $1.5 < \gamma < \gamma_{hc}$ by solving the autonomous boundary value problem. To do this, both γ and u_{S_m} were treated as free parameters. The resulting curve $U_{S_m} = u_{S_m}(\gamma)$ is illustrated in Figure 14. As previously mentioned, a similar process was used to calculate the curve $U_{S_l} = u_{S_l}(\gamma)$ which is also illustrated in Figure 14. The region for which $U_{S_l}(\gamma) < u_0 < U_{S_m}(\gamma)$ and $\gamma \in (\gamma_-, \gamma_{hc})$ is labeled as region B . Thus, for each $(u_0, \gamma_0) \in B$, the trajectory of the (FS) in Liénard form is attracted to Ω_p for the initial condition $(u_0, v_0) = (u_0, 0)$. Although there are other (u_0, v_0) -pairs which lie between \mathcal{W}_S^+ and \mathcal{W}_S^- , the pairs of the form $(u_0, 0)$ are easy to characterize by

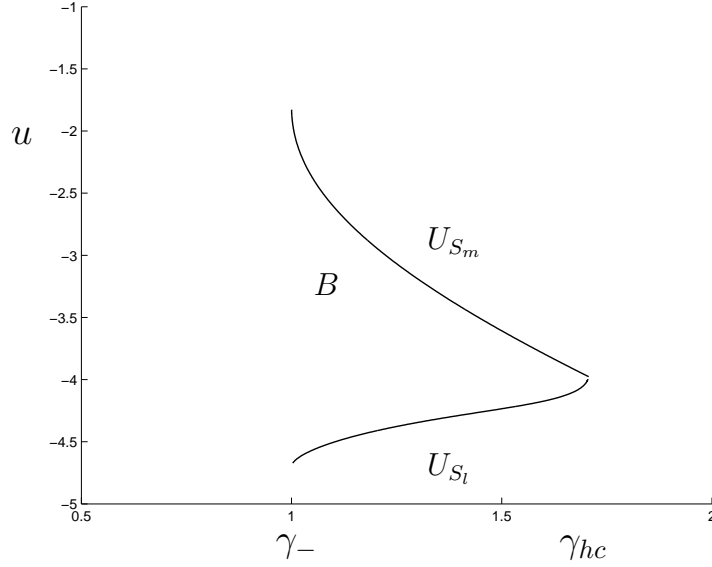


Figure 14. This figure shows the two curves $U_{S_l}(\gamma)$ and $U_{S_m}(\gamma)$ for $\gamma_- < \gamma < \gamma_{hc}$. The set $B = \{(u, \gamma) : U_{S_l}(\gamma) < u < U_{S_m}(\gamma), \gamma \in (\gamma_-, \gamma_{hc})\}$ is also labeled.

the two functions $U_{S_l}(\gamma)$ and $U_{S_m}(\gamma)$. Furthermore, in later simulations of (FULL) where the cell is assumed to be at rest, v_0 is zero.

Recall that one of the goals in this section is to determine what types of initial conditions of (FS) are in \mathcal{B}_p . To do this, note that associated with every initial condition $(u_0, v_0) \in \mathbb{B}_P$ of (3.28)-(3.29) and γ_0 -value is an initial condition (u_0, w_0) of (FS), where $w_0 = f(u_0) - \gamma_0$. With that said, given the initial condition (u_0, w_0) , the trajectories of (FS) will be attracted to the periodic orbits whenever the pair (u_0, γ_0) is in the region B and $w_0 = f(u_0) - \gamma_0$ (for any $\gamma_0 \in (\gamma_-, \gamma_{hc})$). Furthermore, trajectories of (FS) (with initial condition (u_0, w_0)) will also be attracted to Ω_p whenever $u_0 \in (\bar{u}_m, u_{S_u})$ and $w_0 = f(u_0) - \gamma_0$. Therefore, given $\gamma_0 \in (\gamma_-, \gamma_{hc})$, $(u_0, w_0) \in \mathcal{B}_P$ whenever $u_0 \in \{(u_{S_l}, u_{S_m}) \cup (\bar{u}_m, u_{S_u})\}$ and $w_0 = f(u_0) - \gamma_0$. In contrast, the trajectories of (FS) will be attracted to \mathbb{S}_L , whenever

an initial condition (u_0, w_0) with a u_0 -value lies between $u_{S_m}(\gamma_0)$ and $\bar{u}_m(\gamma_0)$ is used. The trajectories of (FS) will also be attracted to S_L when the u_0 -value of the initial condition lies below $u_{S_m}(\gamma_0)$, even though the solution will travel around Ω_p first. In these cases $(u_0, w_0) \in \mathcal{B}_L$ where again $w_0 = f(u_0) - \gamma_0$.

To illustrate these results four examples are shown in Figure 15. Illustrated in this figure are the trajectories of (FULL) when given four different initial conditions. The different responses occur as a result of the basin of attraction of Ω_p in (FS). In Figure 15a), a trajectory of (FULL) with the initial condition

$$(u_0, w_0, \gamma_0) = (u_0, f(u_0) - \gamma_0, \gamma_0), \text{ with } u_{S_m}(\gamma_0) < u_0 < \bar{u}_m(\gamma_0)$$

is shown. In this case $(u_0, \gamma_0) = (-2.5, 1.25)$. As is seen, the trajectory is attracted to S_L since $(u_0, w_0) \in \mathcal{B}_L$. In Figure 15b), a trajectory of (FULL) with the initial condition

$$(u_0, w_0, \gamma_0) = (u_0, f(u_0) - \gamma_0, \gamma_0), \text{ with } (u_0, \gamma_0) \in B$$

is shown. In this case $(u_0, \gamma_0) = (-3.5, 1.25)$. As is seen, the trajectory is attracted to the periodic orbits since $(u_0, w_0) \in \mathcal{B}_P$. In Figure 15c), a trajectory of (FULL) with the initial condition

$$(u_0, w_0, \gamma_0) = (u_0, f(u_0) - \gamma_0, \gamma_0), \text{ with } u_0 < U_{S_l}(\gamma_0)$$

is shown. In this case $(u_0, \gamma_0) = (-4.75, 1.25)$. As is seen, the trajectory is attracted to S_L even though it travels around Ω_p before returning to S_L since $(u_0, w_0) \in \mathcal{B}_L$. Lastly, in Figure 15d), a trajectory of (FULL) with the initial condition

$$(u_0, w_0, \gamma_0) = (u_0, f(u_0) - \gamma_0, \gamma_0), \text{ with } \bar{u}_m(\gamma_0) < u_0 < u_{S_u}(\gamma_0)$$

is shown. In this case $(u_0, \gamma_0) = (1, 1.25)$. As is seen, the trajectory is attracted to the periodic orbits since $(u_0, w_0) \in \mathcal{B}_P$.

Since one of the goals in this dissertation is to predict and describe the solutions of (FULL), understanding the basins of attraction is important. Whenever (FS) shifts rapidly (due to an input such as constant current pulses), the trajectories of the solution of (FULL) will also undergo a rapid change. Thus, knowing which initial conditions in (FS) will cause the solutions to be attracted to Ω_p is key in predicting the responses of (FULL). The numerical results presented in this section give a general description of the location of the basin of attraction for Ω_p (and \mathbb{S}_L) with respect to (FS). As such, it can be used to predict the response of (FULL) when an input incorporates rapid transitions similar to those illustrated in rows 1, 2, 3, 5, and 8 of Table 1.

In this chapter the definitions for (FS), (SS), and (AFS) were given. These definitions were derived in terms of the amplitude \bar{I} , of a constant current pulse. These subsystems were used to compute (1) the active phase duration T_A and (2) the silent phase duration T_{SP} . Both durations will be used in the next chapter to describe the solution cycle of (FULL) when given a constant current pulse. In addition, the basin of attraction for the periodic orbits whenever $\gamma \in (\gamma_-, \gamma_{hc})$ was also discussed. For each $\gamma \in (\gamma_-, \gamma_{hc})$, AUTO was used to compute the values u_{S_l} and u_{S_m} (defined from the Liénard form of (FS)). Based on these computations, it was determined that for an initial condition of (FULL) (in the bistable region) with a u -value between u_{S_l} and u_{S_m} (and appropriate w_0 -value), the trajectories of (FULL) were attracted to the periodic orbits.

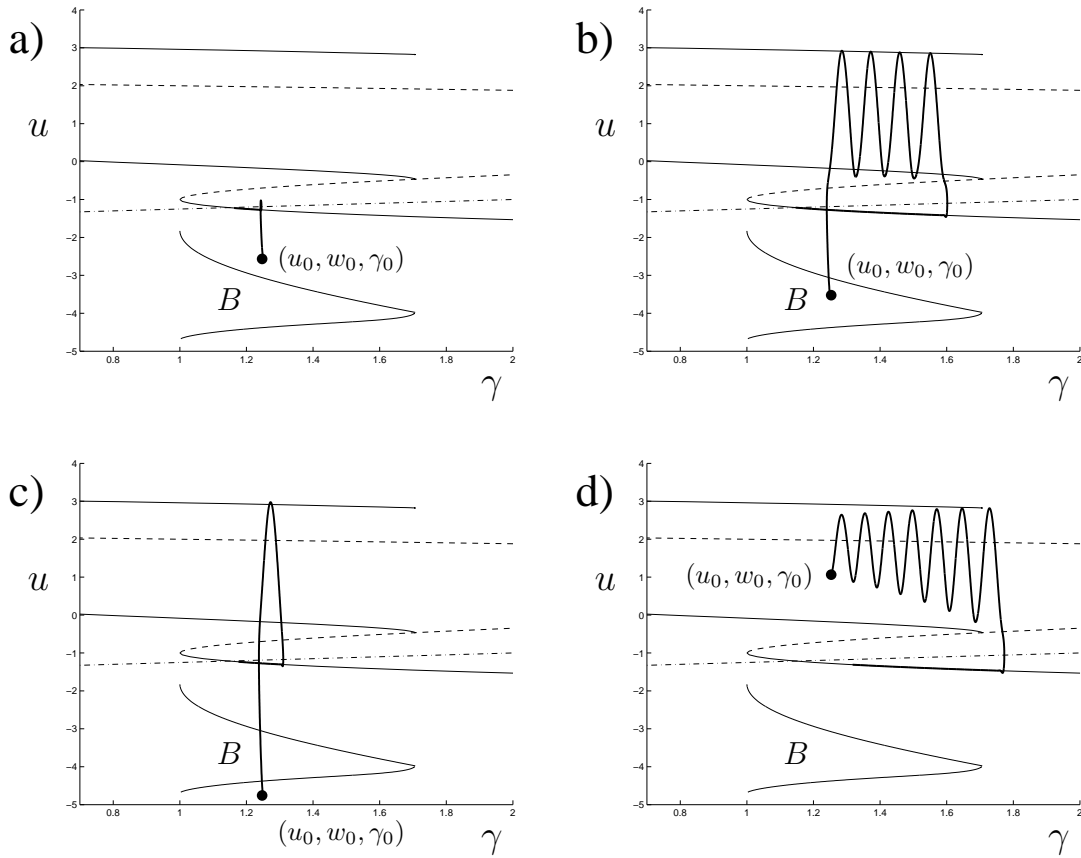


Figure 15. This figure shows four different trajectories of (FULL) (thick lines) when four different initial conditions are chosen. In each case, the dynamics of (FULL) are different and are a result of the location of each initial condition with respect to the basin of attraction of Ω_p in (FS). In each figure, the (FS) bifurcation structure (thin lines) has been included as a reference as well as $\dot{\gamma} = 0$ (dash-dot lines). Also illustrated in each figure is the region B which represents the range of u (for each γ in the bistable range) where \mathcal{B}_p plays a role in the trajectories of (FS) (cf. Figure 14). For the initial condition $(u_0, w_0, \gamma_0) = (-2.5, f(-2.5) - 1.25, 1.25)$, a) shows that the trajectory of (FULL) is attracted to S_L since $(u_0, w_0) = (-2.5, f(-2.5) - 1.25) \in \mathcal{B}_L$. For the initial condition $(u_0, w_0, \gamma_0) = (-3.5, f(-3.5) - 1.25, 1.25)$, b) shows that the trajectory of (FULL) is attracted to Ω_p since $(u_0, w_0) = (-3.5, f(-3.5) - 1.25) \in \mathcal{B}_P$. In c), an initial condition, which has a u_0 -value that lies below U_{S_L} , is used. Even though the trajectory of (FULL) is attracted to S_L when the initial condition $(-4.75, f(-4.5) - 1.25, 1.25)$ is used, it first travels around Ω_p before returning to S_L . Figure d) shows the trajectories of (FULL) when an initial condition that has $\bar{u}_m < u_0 < u_{S_u}$ is used. This figure shows that the trajectory of (FULL) is attracted to Ω_p when the initial condition $(1, f(1) - 1.25, 1.25)$ is used.

When using (FULL) to model neurons it is important to remember that certain dynamics can occur which are unrealistic. Specifically, many issues arise from the study of the basins of attraction. For example, in the preceding description, u was found to have a range above the periodic orbits where an initial condition (of the form $(u_0, 0)$ in the Liénard system) chosen from this range would be between \mathcal{W}_S^+ and \mathcal{W}_S^- (cf. Figure 13a)). For such an initial condition the trajectories of the Liénard system would be attracted to the periodic orbit, and thus there would correspond an initial condition of (FS) which would be in \mathcal{B}_P . If one wanted to calculate this range, similar calculations (using AUTO) can be made as those presented in this chapter. This would enhance the general knowledge for the dynamics of (FULL), but would not provide any additional information for modeling neurons.

To further explain why this range is unrealistic in modeling, recall that u represents the transmembrane somal potential. As such, certain physical limitations on the value of u must be made. For example, membrane potentials are typically in the millivolts range between $-100mV$ and $150mV$ with a typical resting state around $-60mV$. Specifically, for certain pyramidal cells, depolarization can cause action potentials at the soma which can measure close to $150 mV$ [55]. Since each burst cycle represents a series of action potentials, the span between the rest state and the burst height helps determine a plausible range for the potential u . Since (FULL) is a phenomenological model, the rest state u_r and the maximum value u_{max} during a burst cycle are $u_r \approx -1.5$ and $u_{max} \approx 3$. If the larger range of u was incorporated, this would imply membrane potentials of double the maximum ranges observed experimentally. Thus, the range of u , as described in Figure 13b)

would correspond to a more realistic physiological range than Figure 13a). Generally, it is important to keep both the dynamics and realistic variable values in mind when using this model. A few examples of these issues have been included in the following chapter to illustrate many of the possible dynamics of (FULL).

CHAPTER 4

CONSTANT CURRENT PULSES

Having established key definitions in Chapter 3, an analysis of the numerical responses illustrated in Figure 9 can now be given. Recall that both the definitions and the responses presented so far are based on using a constant current pulse. These types of inputs constitute a class, and a description of the solutions of (FULL) when this class of inputs is used will be given in this chapter. To guarantee that either the *On* or the *Off* response can occur, we will show that the amplitude \bar{I} must attain a threshold. In addition to this threshold condition, in order for an *Off* response to occur, the pulse must also be of sufficient duration. In this chapter, the threshold conditions are determined and the necessary durations (for the *On* and *Off* responses) are derived using both the active phase duration T_A and the silent phase duration T_{SP} . These threshold conditions will also help to provide realistic ranges for u when modeling neurons. Some examples that illustrate possible unrealistic neuron dynamics are also included in this chapter. For these examples, the basin of attraction of Ω_p will be important.

Also presented in this chapter is a description of a solution of (FULL) that reproduces the *Mixed* response illustrated in Figure 1c). In order for (FULL) to reproduce this response, a constant *On* and *Off* current pulse is defined and incorporated in the model. In order to guarantee a rebound burst, given an *On* response, a minimum duration for the silent

phase must be attained. By incorporating the analyses from the *On* and *Off* responses, upper and lower bounds for the minimum duration are given. These curves will also depend on the amplitudes and durations of the constant *On* and *Off* current pulse.

Before the solutions illustrated in Figure 9 are described, we present some terminology. First, in order to describe each response we must define and label certain point locations and relevant transitions points. To do this, we adapt a subscript convention for dependent variable values at these points for each of the different responses. For each response, if P_k is the point label, then $P_k(\bar{I}) = (z_k(\bar{I}), u_k(\bar{I}))$ is the point coordinate when the current pulse is applied. Here $k = hb, hc, +, \text{ and } -$, so, for example, $P_-(\bar{I}) = (z_-(\bar{I}), u_-(\bar{I}))$ is the location of the left most saddle-node bifurcation of (FS) when the amplitude of the pulse is \bar{I} . To further describe the cycles, the labels N, F , and M are used for the *On*, *Off*, and *Mixed* response, respectively. The labels N_i, F_i , and M_i for $i = 0, \dots, 3$, will be used to track the numerical traces at important transition points for each type of response. Note that the different labels (N, F , and M) are used to clearly identify the differing cycles for the *On* (N), the *Off* (F), and the *Mixed* (M) responses.

To illustrate how these labels will be used, relevant transition points for the *On* response (cf. Figure 16) are summarized in Table 2. There, when applicable, we summarize the leading-order times at which the points occur. Here t_0 is the time at which the constant current pulse is turned on and T is the duration of the stimulus. In the table, T_A is the leading-order duration of the active phase for the *On* response. Similar descriptions will be used to summarize the transition points for both the *Off* response and the *Mixed* response.

Label	Description	t
P_{hb}	Hopf Point of (FS)	
P_{hc}	Homoclinic point of (FS)	
P_+	Right most saddle node bifurcation of (FS)	
P_-	Left most saddle node bifurcation of (FS)	
N_0	Equilibrium of (FULL) for $I = 0$	$t = t_0$
N_1	Solution coordinate upon release from the active phase	$t = (t_0 + T_A)^+$
N_2	Solution coordinate before the stimulus is turned off	$t = (t_0 + T)^-$
N_3	Solution coordinate after the stimulus is turned off	$t = (t_0 + T)^+$

Table 2. Definition of points needed to describe On response cycles.

Second, the projections of the equilibria $\bar{X}(\bar{I}) = (\bar{u}, \bar{w}, \bar{z})$ of (FULL) which are dependent on the amplitude value \bar{I} will also be labeled where necessary. Given (FULL), \bar{u} is a root of

$$G(u) - h(u) + \bar{I} = 0, \quad (4.1)$$

and depends on \bar{I} . Then, $\bar{w} = g(\bar{u})$, and $\bar{z} = h(\bar{u})$. Initial conditions for all simulations of (FULL) were chosen to be $\bar{X}(0)$, corresponding to the cell at rest.

Given these definitions, a constant stimulus \bar{I} effectively shifts the bifurcation structure of (FS) in z . For example, the Z -shaped curve and Ω_p will shift right for $\bar{I} > 0$, left for $\bar{I} < 0$, and for $k = hb, hc, +$, and $-$,

$$z_k(\bar{I}) = z_k(0) + \bar{I}.$$

Also note that parts of the solutions of (FULL) in these figures travel near the lower branch (stable manifold) $\mathbb{S}_L(\bar{I})$ of (FS) as previously defined (i.e., \mathbb{S}_L in (3.5) with $\gamma = z - \bar{I}$).

On Response

In this section, we consider the dependence of *On* responses such as those illustrated in Figure 9 on both the magnitude $\bar{I} > 0$ and duration T of an input of the form of a constant current pulse. For the solution illustrated in Figure 16, the transitions of $I(t)$ in t between $\bar{I} = 0$ and $\bar{I} = 0.8$ are rapid. As such, a singular approximation of that solution can be described by the slow-subsystem (SS) and the averaged-fast-subsystem (AFS) of (FULL) with transition points being pieced together from the fast-subsystems for $\bar{I} = 0$ and $\bar{I} = 0.8$. In what follows, the relevant subsystems are used to identify regions in the (\bar{I}, T) parameter plane where different *On* responses occur.

Shown in Figure 16 are the bifurcation diagrams of (FS) in z for $\bar{I} = 0$ and $\bar{I} = 0.8$. Superimposed on these diagrams is the *On* response depicted in Figure 9a). Notice that we have labeled the relevant locations of critical transition points of the overall cycles. In Figure 16a), the Hopf point $P_{hb}(0.8) = (z_{hb}(0.8), u_{hb}(0.8))$ and the upper saddle-node point $P_+(0.8) = (z_+(0.8), u_+(0.8))$ of (FS) are labeled. In Figure 16, the z nullcline of (FULL) is shown as the dashed-dot line passing through the lower branch of the Z -curve. Given the definition of $h(u)$ and the values of the slow parameters $\lambda_s = (\alpha, \beta)$ used to generate the responses in Figures 9, recall that $\dot{z} > 0$ above the nullcline and $\dot{z} < 0$ below the nullcline.

For the solution shown in Figure 16 the cell remains in its rest state $\bar{X}(0)$ for $t < t_0$. At $t = t_0^+$, the rapid transition from point N_0 to the active phase depicted can occur only if

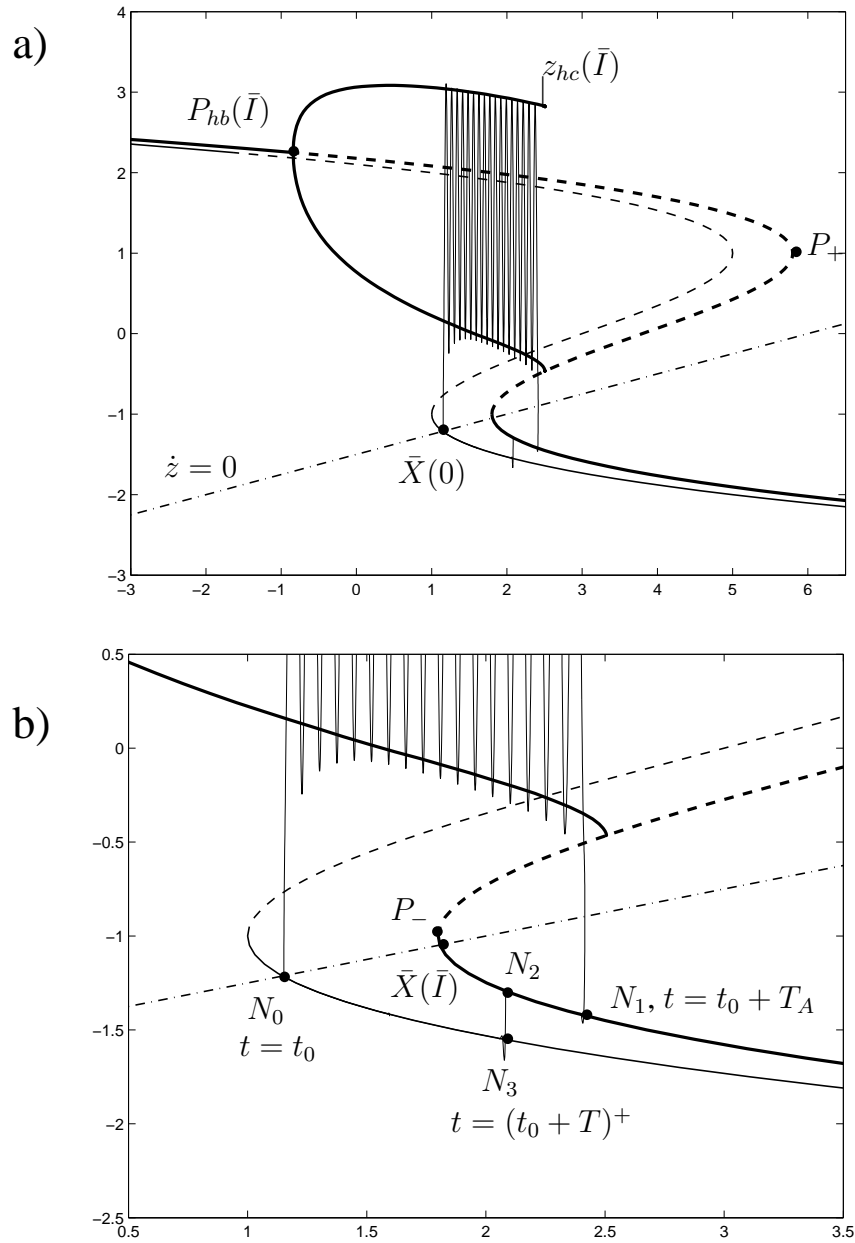


Figure 16. Shows an *On* response solution of (FULL) projected onto the fast subsystem diagrams for $\bar{I} = 0$ (thin) and $\bar{I} = 0.8$ (thick). Also shown in this figure is the z -nullcline of (FULL). Diagram b) is a closeup of a) showing relevant transition points and the leading-order times at which transitions occur. Also shown is the new equilibria $\bar{X}(\bar{I})$ of (FULL) which here is close to the saddle node P_- .

$\bar{I} > \bar{I}^+$ where

$$\bar{I}^+ = \bar{z}(0) - \gamma_-$$

is the current threshold for the *On* response. Since (FS) has periodic orbits only if $z - \bar{I} \in (\gamma_{hb}, \gamma_{hc})$, solutions of (FULL) are then attracted to Ω_p of (FS) provided

$$\bar{I}^+ < \bar{I} < \bar{I}_{hb}, \quad (4.2)$$

where

$$\bar{I}_{hb} \equiv \bar{z}(0) - \gamma_{hb}.$$

If (4.2) is not satisfied then two possibilities can occur. First, in the case when $\bar{I}_{hb} < \bar{I}$, the trajectories will be attracted to S_U and thus will not be initially attracted to Ω_p . Second, if $\bar{I} < \bar{I}^+$, the point N_0 is in the bistable region. Notice that for every amplitude value $0 < \bar{I} < \bar{I}^+$, the value $u_0(\bar{I})$ will lie above U_{S_M} and thus will be in \mathcal{B}_L . In this case the solution will go to S_L and move towards the new equilibria without going through a bursting cycle (cf. Figure 15a). For the response illustrated in Figure 16, $\bar{I} = 0.8$ was chosen to satisfy the conditions (4.2).

When the threshold conditions (4.2) are satisfied, solutions of (FULL) will be attracted to the periodic orbits and will move slowly right since $\dot{z} > 0$ above the z nullcline. For a sufficiently large stimulus duration T , a transition from the active phase back to the lower branch can occur i.e., when the pulse duration is greater than the active phase duration. In this case, T_A is defined as the leading-order time for $z(t)$ to increase from its entry point

$\bar{z}(0)$ in the active phase to the homoclinic point at $z_{hc}(\bar{I})$. Thus,

$$T_A = T_A(\bar{I}) = \int_{\bar{z}(0)-\bar{I}}^{\gamma_{hc}} \frac{d\gamma}{h(\hat{u}(\gamma)) - (\gamma + \bar{I})} \quad , \quad (4.3)$$

where (recall from (3.25))

$$\hat{u}(\gamma) \equiv \frac{1}{T_p(\gamma)} \int_0^{T_p(\gamma)} \Omega_1(t, \gamma) dt,$$

and Ω_1 is the u component of the periodic orbits defined in (3.4). Note that although T_A depends explicitly on \bar{I} , the average \hat{u} does not.

Thus, if $T > T_A$ a (rapid) transition at $z = z_{hc}(\bar{I})$ to $S_L(\bar{I})$ can occur (i.e., Point N_1 on Figure 16b)). When such transitions occur, since the point N_1 is below the z nullcline, the projection of the solution will travel near $S_L(\bar{I})$ and proceed slowly to the left until the stimulus is turned off at $t = (t_0 + T)^+$. Since $I(t) = 0$ for $t > (t_0 + T)$, (FS) shifts rapidly (left) back to its original position and a transition back to $S_L(0)$ can occur (i.e., the rapid transition from point N_2 to point N_3 in Figure 16b)). In this case the point N_2 lies in the monostable range of $S_L(0)$, and the transition from N_2 to N_3 does occur. For all remaining time afterwards the solution is attracted back toward the equilibria $\bar{X}(0)$.

For the model and stimulus parameters used to generate Figure 16 the aforementioned description applies. For other values of (\bar{I}, T) the cycle description may differ, and we include some comments here. For example, in Figure 16 note that $\bar{X}(\bar{I}) \in \mathbb{S}_L(\bar{I})$. However, for \bar{I} sufficiently large, $\bar{X}(\bar{I}) \in \mathbb{S}_M(\bar{I})$. In this event, the solution of (FULL) could burst persistently for T sufficiently large. Indeed, if $\bar{X}(\bar{I})$ intersects the homoclinic point of (FS), chaotic dynamics are possible [77]. As an example, Figure 17d) shows that multiple bursts

are possible if the duration T is sufficiently large. It is therefore of interest to determine those \bar{I} values for which $\bar{X}(\bar{I}) \in \mathbb{S}_L(\bar{I})$, and the values for which $\bar{X}(\bar{I}) \in \mathbb{S}_M(\bar{I})$ and $\bar{z}(\bar{I}) < z_{hc}(\bar{I})$ (to avoid the chaotic dynamic case). The threshold value \bar{I}_m , for which $\bar{X}(\bar{I}) \in \mathbb{S}_L(\bar{I})$ can be obtained by setting $u = u_-(0) = -1$ in (4.1), is:

$$\bar{I}_m = h(u_-) - G(u_-) = -(\beta(1 + \alpha) + 1) . \quad (4.4)$$

The value \bar{I}_{hc} for which $\bar{X}(\bar{I})$ intersects the homoclinic point can be obtained by setting $u = u_{hc}(0)$ in (4.1):

$$\bar{I}_{hc} = h(u_{hc}(0)) - G(u_{hc}(0)) . \quad (4.5)$$

Depending on the fast parameter set λ_f , it is possible that either $\bar{I}_{hb} < \bar{I}_{hc}$, or $\bar{I}_{hc} < \bar{I}_{hb}$. Thus, in order to guarantee a rapid transition to the active phase and assure that $\bar{X}(\bar{I})$ does not intersect the homoclinic point, the stimulus amplitude must be smaller than the upper bound value \bar{I}_{ub} defined as:

$$\bar{I}_{ub} = \text{minimum}(\bar{I}_{hb}, \bar{I}_{hc}) . \quad (4.6)$$

For the fast parameter set λ_f used to generate Figure 16, $\bar{I}_{ub} = \bar{I}_{hc}$.

A second issue to note is that if $\bar{I}^+ < \bar{I} < \bar{I}_{ub}$ and $T < T_A$ then $z(t_0 + T)^+ < z_{hc}(\bar{I})$.

The response under these conditions depends on the value of $z(t_0 + T)^+$. If the duration is too short, $z(t_0 + T)^+$ may be in the γ -range (γ_-, γ_{hc}) where (FULL) is bistable (cf. Figure 10a)). If $z(t_0 + T)^+ \in (\gamma_-, \gamma_{hc})$, then $(u(t_0 + T)^+, w(t_0 + T)^+)$ will either be in \mathcal{B}_P or in \mathcal{B}_L . If $(u(t_0 + T)^+, w(t_0 + T)^+) \in \mathcal{B}_P$, the solution will be attracted to the periodic orbits and will travel to the right until it exits at $z_{hc}(0)$ (then the solution will travel on

$S_L(0)$ towards $\bar{X}(0)$). Thus, the solution may continue to spike even after the stimulus is turned off. The number of these post stimulus spikes (PSS) will depend on the (FS) and the fast parameter set λ_f . An example of this type of response can be found in Figure 17a). For the examples illustrated in Figure 17 the stimulus amplitude was chosen to be $\bar{I} = 1.8$.

On the other hand, if $(u(t_0 + T)^+, w(t_0 + T)^+)$ is in \mathcal{B}_L , then the point N_1 will be on $S_L(0)$ rather than on $S_L(\bar{I})$ (in contrast to the case illustrated in Figure 16). In this case the solution will simply tend back to the equilibria of (FULL) at N_0 without going through the transitions at the points N_2 and N_3 . Under these conditions the response will occur for the entire duration of the stimulus (cf. Figure 17b)). For both of the cases described above, the value of $u(t_0 + T)^+$ cannot be explicitly computed using (AFS) and thus the point $(u(t_0 + T)^+, w(t_0 + T)^+)$ cannot be guaranteed (although it may be possible with other analyses) to be in either \mathcal{B}_P or \mathcal{B}_L . Even though under certain conditions the response may continue to spike upon release, the *On* response (spiking) will at least occur during the entire duration of the stimulus when $\bar{I}^+ < \bar{I} < \bar{I}_{ub}$ and $T < T_A$.

It may also be possible to have (PSS) for a large duration $T > T_A$. If the duration is large enough to allow multiple bursts, then by choosing T properly, the stimulus may turn off before the response can complete the next bursting cycle. Figure 17c) shows an example where the stimulus is turned off before the solution can complete the second cycle. In this case $(u(t_0 + T)^+, w(t_0 + T)^+) \in \mathcal{B}_P$, and results in the presence of PSS upon release of the stimulus.

Many of the dynamics described above and specifically illustrated in Figures 17a) and

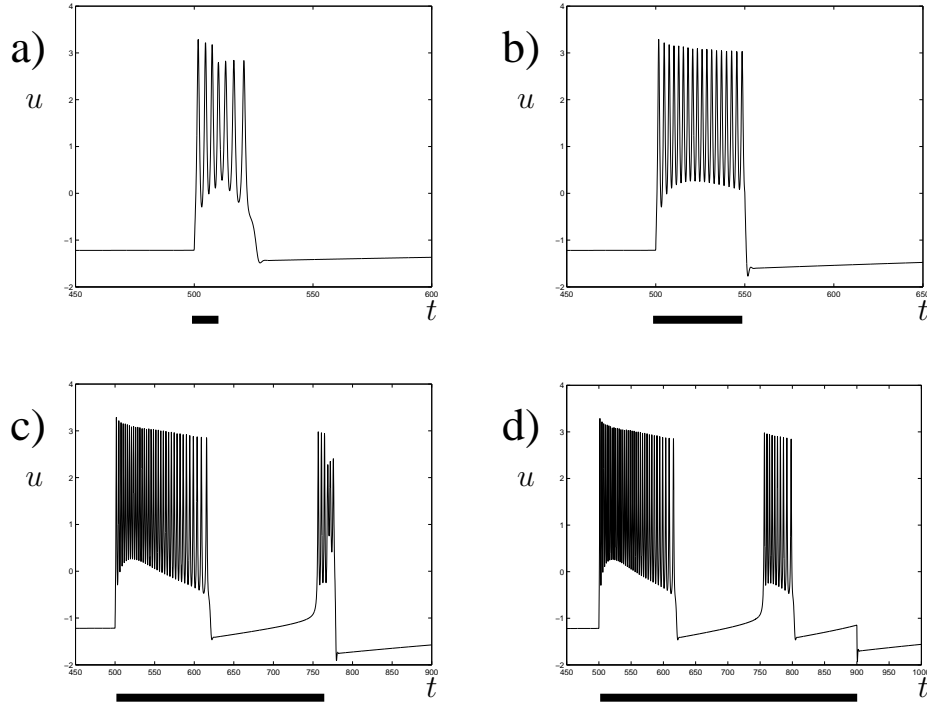


Figure 17. This figure shows the response of (FULL) for the stimulus amplitude value $\bar{I} = 1.8$ and various durations. In each figure the black line represents the time duration of the input. In a) $T = 10$ is chosen smaller than T_A , and the response continues to spike after the stimulus is turned off. For a duration value $T = 50 < T_A$, b) shows that the *On* response will occur during the entire duration of the stimulus. Both responses in a) and b) show that for the values (\bar{I}, T) corresponding to region (b) in Figure 19 the *On* response at least occurs for the entire duration of the stimulus. Figure c) shows that the (PSS) found in a) may recur if the duration is large enough. By choosing $T = 268 > T_A$ the stimulus is turned off before the solution goes through the second bursting cycle creating the post stimulus spiking. For the duration $T = 400 > T_A$, d) shows that multiple bursts may occur. Also notice that in d), the cycle has two silent phase durations. The first duration, T_{SP_1} , occurs between the two bursting cycles, and the other T_{SP_2} is the duration between the second burst and the time the pulse is turned off.

Figures 17c), are examples of dynamics which may be unrealistic when modeling visual neurons. Recall that a constant current pulse can be used to simulate an *in vitro* experiment where current injection is used. When this is the case, neurons do not generally exhibit PSS. If on the other hand, as a result of an *in vivo* experiment, a neuron has a response similar to those in Figure 17a) or c), then perhaps the response comes as a result of the network properties or synaptic plasticity. Therefore, knowing what types of neuronal responses that can occur can help to determine the different dynamics of (FULL) which are applicable when modeling neurons. On the other hand, understanding the dynamics of (FULL) can help determine plausible responses of neurons. To conclude this section, a summary of the preceding results are found in the Table 3. These results are also depicted in Figure 19 for positive values of \bar{I} . In Figure 19, the region (b) corresponds to the first row of Table 3; region (c) corresponds to the second row of Table 3: region (d) corresponds to the third row of Table 3. Thus, the type of *On* response depends on both the synaptic current's amplitude and duration.

Stimulus Conditions	Outcome
$\bar{I}^+ < \bar{I} < \bar{I}_{ub}, T < T_A(\bar{I})$	<i>On</i> response for at least the entire duration of stimulus (cf. Figures 17a) and b))
$\bar{I}^+ < \bar{I} < \bar{I}_m, T > T_A(\bar{I})$	<i>On</i> response always terminates before stimulus terminates (cf. Figure 9a))
$\bar{I}_m < \bar{I} < \bar{I}_{ub}, T > T_A(\bar{I})$	Other dynamics possible (e.g. solutions such as those illustrated in Figures 17c) and d))

Table 3. A description of the possible responses given an *On* stimulus.

Off Response

A similar cycle can be described for the *Off* responses illustrated in Figure 9b). The conditions needed for an *Off* response differ from those of an *On* response in such a way that to guarantee an *Off* response, a sufficiently large duration is needed. Similar to the regions in the (\bar{I}, T) parameter plane where an *On* response can occur, we identify a region in the (\bar{I}, T) parameter plane where an *Off* response can occur. Here again, the transitions of $I(t)$ in t are rapid, therefore the fast dynamics of trajectories of (FULL) can be pieced together from different subsystems.

In Figure 18, the (FS) shown are for $\bar{I} = 0$ and $\bar{I} = -1.8$, and again the cell is assumed to be at its rest state $\bar{X}(0)$ for $t < t_0$. The z nullcline of (FULL) is also shown as the dashed-dot line passing through the lower branch of the Z -curve. Recall, that $\dot{z} > 0$ above the nullcline and $\dot{z} < 0$ below the nullcline.

At $t = t_0^+$ a rapid transition from the point F_0 to the point F_1 on the lower branch $S_L(\bar{I})$ can occur (conditions for this transition are described at the end of this section). Since the point F_1 is below the z nullcline, the projection of the solution will travel near $S_L(\bar{I})$ and proceed slowly to the left until the stimulus is turned off. At $t = (t_0 + T)^+$ a rapid transition to the active phase can occur only if the duration T of the stimulus is sufficiently large and $z(t_0 + T) \in (\gamma_{hb}, \gamma_-)$. This latter restriction can be satisfied only if

$$\bar{I}_{lb} < \bar{I} < \bar{I}^- , \quad (4.7)$$

where \bar{I}_{lb} and \bar{I}^- are certain minimum and maximum thresholds for an *Off* response, respectively. To compute these thresholds first note that for equilibria $\bar{X}(\bar{I})$,

$$\begin{aligned} z - \bar{I} &= G(u) \\ z &= h(u), \end{aligned}$$

from which we deduce

$$\bar{I} = z - G(h^{-1}(z)). \quad (4.8)$$

Using this equation, the maximum threshold is given by $\bar{I}^- \equiv z_- - G(h^{-1}(z_-))$. This condition guarantees that $\bar{z}(\bar{I}) < z_-(0)$. Similarly, the minimum value of \bar{I} which guarantees that $z_{hb}(0) < \bar{z}(\bar{I})$ is given by $\bar{I}_{lb} \equiv z_{hb}(0) - G(h^{-1}(z_{hb}(0)))$.

Moreover, as previously mentioned, a sufficiently large stimulus duration is also needed to have an *Off* response. To determine this duration, we use the silent phase duration T_{SP} . For $\bar{I} < 0$, the leading order approximation of this time is that duration where the solution of (FULL) travels along $S_L(\bar{I})$ from $z = \bar{z}(0)$ to $z = z_-(0)$. Thus, the threshold duration given by

$$T_S = T_S(\bar{I}) = \int_{\bar{z}(0)}^{z_-(0)} \frac{dz}{h(u_{LB}(z - \bar{I})) - z}, \quad (4.9)$$

is defined as the minimum silent phase duration necessary for an *Off* response (or rebound burst).

The value of $T_S(\bar{I})$ in (4.9) is the leading-order value for the minimum duration which assures that the point F_2 (cf. Figure 18b)) is in the monostable region of Ω_p upon release of the stimulus. If $T > T_S$ and (4.7) is satisfied, a rapid transition to the periodic orbits occurs

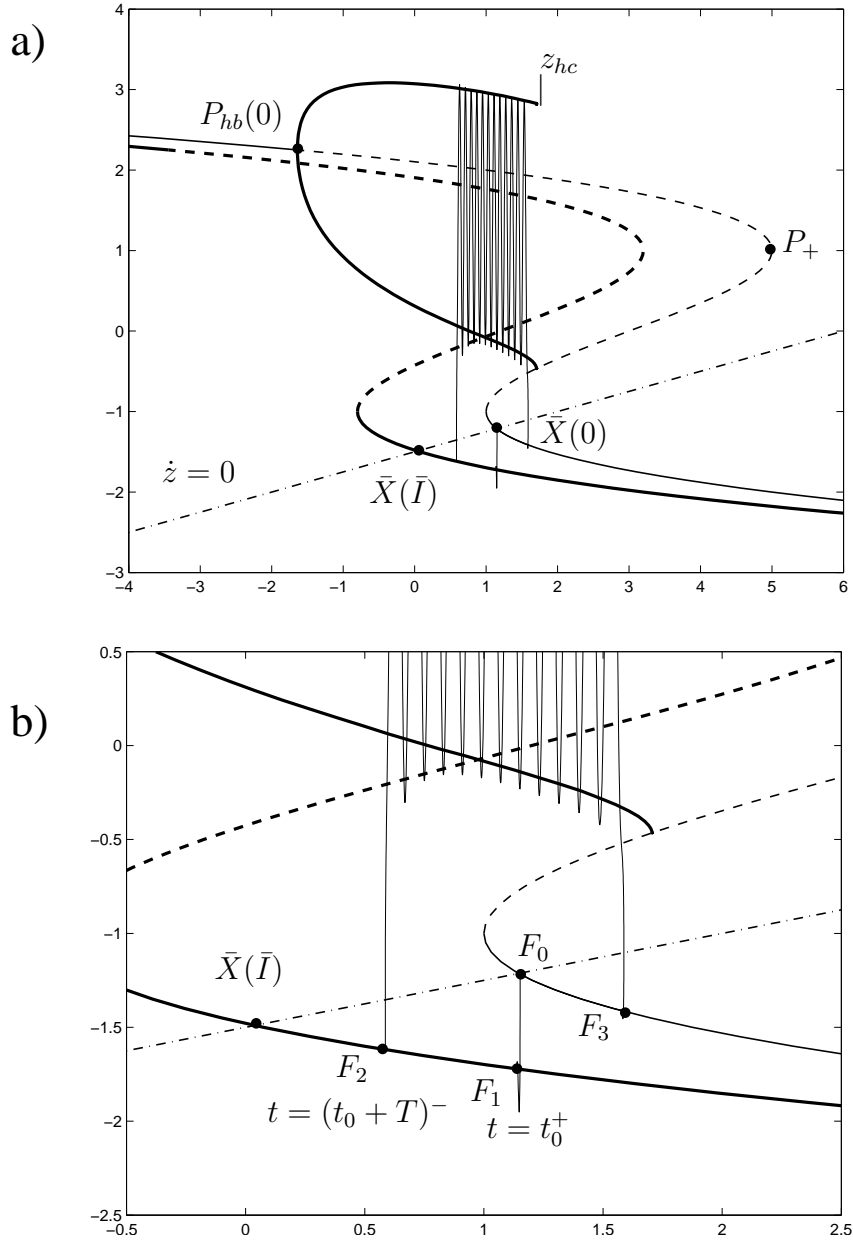


Figure 18. Shows an *Off* response solution of (FULL) projected onto the fast subsystem diagrams for $\bar{I} = 0$ (thin) and $\bar{I} = -1.8$ (thick). Also shown in this figure is the z -nullcline of (FULL). Diagram b) shows the relevant transition points and the leading-order time at which these transitions occur.

at $t = (t_0 + T)^+$. In this case, $z(t)$ will increase slowly until it reaches $z = z_{hc}(0)$, where a transition from the active phase to the point F_3 then occurs. The solution will then tend back to the equilibria of (FULL) at point F_0 , completing the cycle for a rebound burst. The region in the (\bar{I}, T) plane for which these conditions are satisfied for (FULL) is illustrated in Figure 19.

An issue to note with the *Off* response described above relates to the transition that occurs from F_0 to F_1 . This transition will occur whenever $\bar{I} < \bar{I}_b \equiv \gamma_0 - \gamma_{hc}$, since for these values of \bar{I} , F_0 lies in the monostable region of $\mathbb{S}_L(\bar{I})$. On the other hand when $\bar{I}_b < \bar{I} < \bar{I}^-$, at $t = t_0^+$, F_0 may lie in the bistable region of (FS) when $I = \bar{I}$. When this happens, as long as $F_0 \in \mathcal{B}_L$, then the transition from F_0 to F_1 will occur as described above. This condition is guaranteed since \bar{u}_0 lies above the computed curve U_{S_m} (cf. Figure 15) and below $\bar{u}_m(\gamma)$ for all values of $\bar{I} \in (\bar{I}_b, \bar{I}^-)$ and $\gamma \in (\gamma_-, \gamma_{hc})$ (i.e., $(\bar{u}_0, 0) \in \mathbb{B}_L$ defined in Chapter 3). Thus the transition from F_0 to F_1 is guaranteed to occur as described above.

The results of the preceding sections show that when a constant current pulse is used, (FULL) can reproduce both the *On* and *Off* responses. These responses will depend on both the input's amplitude and duration. Figure 19 illustrates parameter regions for \bar{I} and T where these responses can occur. In this figure, the minimum duration to guarantee an *Off* response, T_S , is shown on the left side of the graph as a function of \bar{I} . Thus, for the amplitudes and durations in region (a), an *Off* response is guaranteed to occur. On the right side of this figure, the active phase duration, T_A , is shown as a function of \bar{I} . Also illustrated on the right side of this figure are the regions where certain types of *On* responses

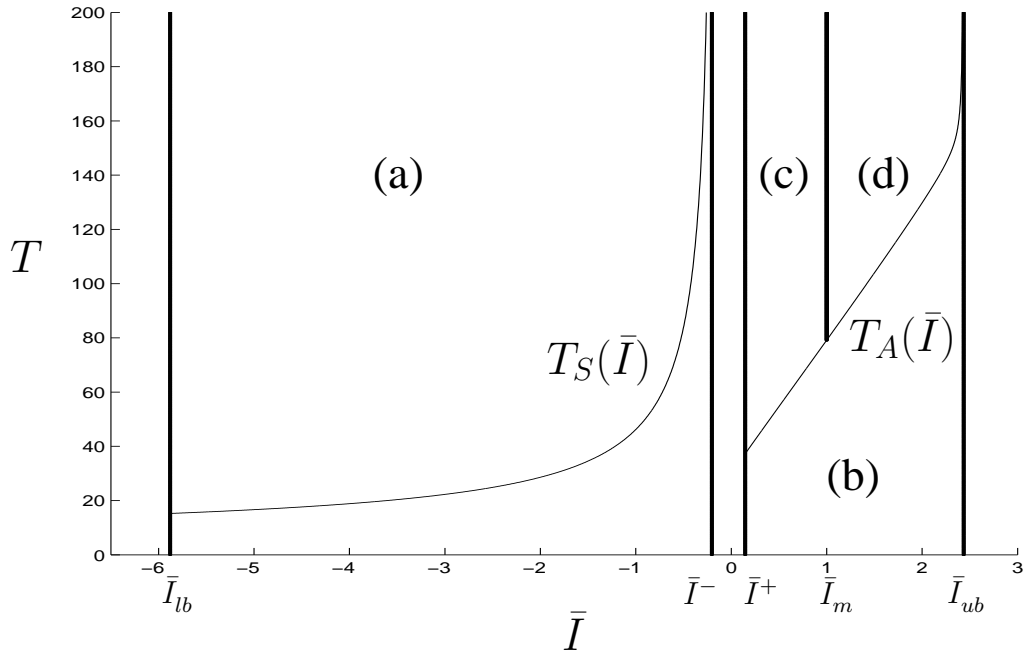


Figure 19. A categorization for the different responses based on input duration T and amplitude \bar{I} . For negative values of \bar{I} , the threshold values \bar{I}_{lb} , and \bar{I}^- are labeled. The minimum duration T_S for an *Off* response is plotted to provide the lower bound for the region (a) where an *Off* response occurs (PIR). For positive values of \bar{I} , the threshold values \bar{I}^+ , \bar{I}_m , and \bar{I}_{ub} have been plotted. The threshold duration T_A for the *On* responses has been plotted to create the regions (b), (c), and (d). In region (b), spiking will occur at least during the entire duration of the input. In region (c), the spiking will terminate before the input is turned off. In region (d), the response will burst, but depending on the duration T , it may go through more than one bursting cycle.

can occur. For the region (b), dynamics such as those illustrated in Figures 17a), and b) are possible. There, the *On* response will occur for the entire duration of the input even though PSS may be present. For the region (c), only one burst cycle is plausible and a response similar to the one illustrated in Figure 9a) can occur. For the region (d), dynamics such as those illustrated in Figures 17c), and d) are possible. In the following paragraph, we

briefly discuss the response of (FULL) when the values (\bar{I}, T) are not in the regions (a)-(d) of Figure 19. Although an example is included there, we will not give further analysis for these regions in this study.

Illustrated in Figure 20 is an example of a numerical solution of (FULL) when the amplitude $\bar{I} = -55$ is used. The response shows that for this amplitude and a duration $T = 10$, a rebound burst occurs. Notice that (1) this amplitude of input is unrealistic when modeling visual neurons, and (2) these conditions are out of the range discussed in Figure 19. When (FULL) is given a constant current pulse with this type of amplitude, the fast-subsystem shifts far to the left. When this occurs, the fast dynamics attract the solution to $S_L(-55)$. Once this transition occurs, the solution will travel along the lower branch until the pulse is turned off. In this example, z -value at $t = (t_0 + T)^+$ (i.e., the point F_2 as illustrated in Figure 18) is to the left of the saddle node point P_- and thus is in the monostable region of Ω_p . Even though a short duration was used, a PIR response can still occur. Due to the dynamics of (FULL), many different types of responses are possible even though they may not all have realistic physiological meanings.

Mixed Response

To reproduce the *Mixed* response illustrated in Figure 1c), we use a combination of the *On* and *Off* responses discussed in this chapter. In this section we describe a numerical example which reproduces the *Mixed* response. This description will be presented in a manner analogous to the previous descriptions for the *On* and *Off* responses.

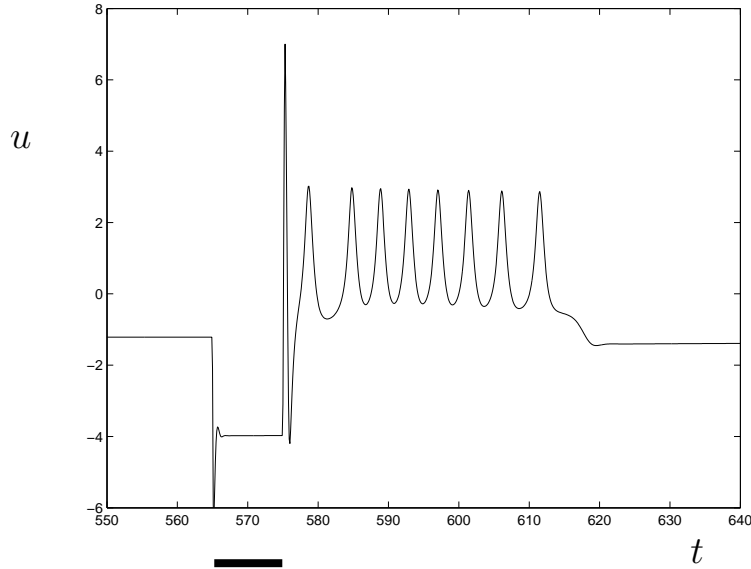


Figure 20. This figure shows that a rebound burst can occur for amplitude and duration values not discussed in Figure 19. In this figure $\bar{I} = -55$, and $T = 10$. The time duration of the input is given as the black line (thick). Even though a rebound burst occurs, this type of input amplitude is unrealistic when modeling visual neurons. Notice that the resulting initial spike also has an unrealistic amplitude value. Nevertheless, this illustrates that the basins of attraction can play an important role when describing the dynamics of (FULL).

In order to reproduce the *Mixed* response the constant current pulse must be altered. Recall that in the *Mixed* response, the cell is given two simultaneous stimuli. To model this, assume that the cell is receiving input from both the excitatory and the inhibitory synapses. Also assume that the stimuli in the *Plus* and *Minus* parts cause the cell to receive inputs from excitatory and inhibitory synapses, respectively. In this case, the input from the excitatory synapses is assumed to be felt immediately but will last only for a duration $T_1 < T$, where T is the total stimulus duration. The input from inhibitory synapses is also assumed to be felt by the cell immediately but lasts until the stimulus is turned off. For convenience, define the duration $T_2 = T - T_1$ to describe the “*Off*” part of the stimulus. To

be specific, define a “constant *On* and *Off* current pulse” as

$$I(t) = \bar{I}_+ (H(t - t_0) - H(t - t_0 - T_1)) + \bar{I}_- (H(t - t_0 - T_1) - H(t - t_0 - T_2)). \quad (4.10)$$

Even though this type of pulse is different from a constant current pulse, it still involves rapid transitions at $t = t_0$, $t = t_0 + T_1$, and $t = t_0 + T_1 + T_2$ similar to those for (2.25).

In Figure 21, the net synaptic current given by (4.10) is superimposed over the voltage $u(t)$. Notice that this reproduces the *Mixed* response illustrated in Figure 1c). In this case $\bar{I}_+ = 0.8$, $\bar{I}_- = -1.8$, $T_1 = 50$, and $T_2 = 200$. Similar to a constant current pulse, to guarantee this type of response, certain thresholds for \bar{I}_+ and \bar{I}_- , and certain durations T_1 and T_2 are needed. Many of the preceding analyses can be implemented to describe these thresholds and durations.

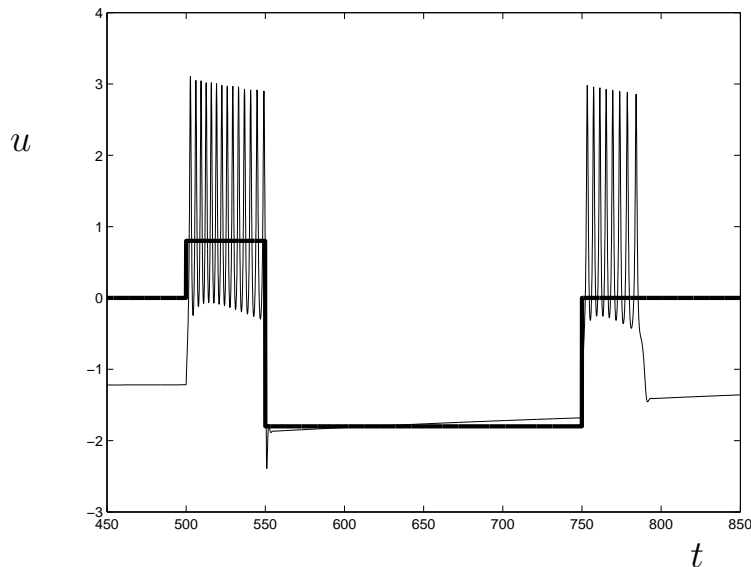


Figure 21. This figure shows a *Mixed* response of (FULL) when given a constant *On* and *Off* current pulse. For the response illustrated in this figure, $\bar{I}_+ = 0.8$, $\bar{I}_- = -1.8$, $T_1 = 50$, and $T_2 = 200$.

For the solution illustrated in Figure 21, the transitions of $I(t)$ in t between $\bar{I} = 0$, $\bar{I}_+ = 0.8$, and $\bar{I}_- = -1.8$ are rapid. Thus, the fast dynamics of the trajectories of (FULL) can be pieced together from the different subsystems in a similar fashion to the *On* and *Off* responses.

Illustrated in Figure 22a) is the first part of the solution (the *On* part), and the second part (the *Off* part) is shown in Figure 22b). Also illustrated in this figure are the bifurcation diagrams of (FS) in z for $\bar{I} = 0$, $\bar{I}_+ = 0.8$, and $\bar{I}_- = -1.8$. To describe this *Mixed* cycle, we use the same subscript convention defined at the beginning of this chapter. Here, the labels $P_k(\bar{I})$ for $k = hb, hc, +$, and $-$, are used to illustrate the critical points of the (FS) for each part of the solution. Also, the points labeled by M_i for $i = 0, 1, 2, 3$, are the critical transition points for the *Mixed* response.

Again, the cell is assumed to initially be at its rest state $\bar{X}(0)$ for $t < t_0$. At $t = t_0^+$ a rapid transition from the point M_0 to the active phase can occur only if $\bar{I}_+ > \bar{I}^+$. In this example the solution then moves right in the active phase until $t = (t_0 + T_1)^+$ where a transition to M_1 occurs. For this particular solution, $T_1 < T_A$, and a rapid transition to M_1 occurs without a transition at the homoclinic bifurcation point. Note that since $T_1 < T_A$ the *On* response occurs during the entire duration T_1 . Also, instead of a transition to $S_L(0)$, as illustrated in Figure 16, a transition to $S_L(-1.8)$ occurs. This describes the first part of the *Mixed* response as illustrated in Figure 22a). Notice that the *On* part will be governed by the same threshold conditions given in Table 3.

The description for the second part of the *Mixed* solution is not very different from the

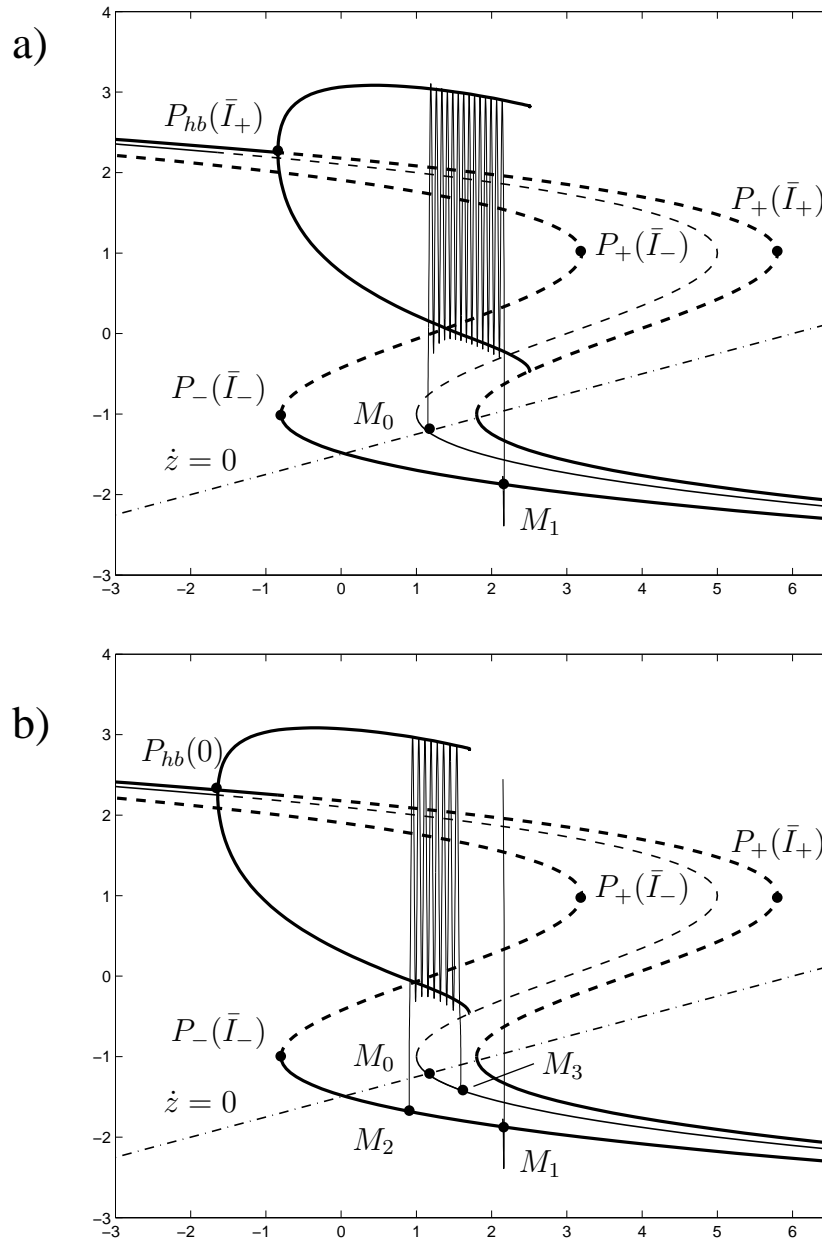


Figure 22. Shows a *Mixed* response solution of (FULL) projected onto the fast-subsystem diagrams for $\bar{I} = 0$ (thin), $\bar{I} = 0.8$ (thick, right most), and $\bar{I} = -1.8$ (thick, left most). Diagram a) shows the relevant transition points for the *On* part of the solution. In a) a rapid transition from the point M_0 to $\Omega_P(0.8)$ occurs at $t = t_0^+$. The solution then travels along the active phase until $t = (t_0 + T_1)^+$, where a rapid transition to the point M_1 occurs. In b) the continuation of the solution illustrated in a) is shown. The solution travels along $S_L(-1.8)$ from M_1 to M_2 . At $t = t_0 + T_1 + T_2$ the stimulus is turned off and a transition from M_2 to $\Omega_P(0)$ occurs. The solution will then travel right and will exit at the homoclinic point where a transition to the point M_3 occurs. This finishes the rebound burst, and the solution will travel along $S_L(0)$ until it reaches the equilibria at M_0 .

description of the *Off* response illustrated in Figure 18. For the times $(t_0 + T_1)^+ < t < (t_0 + T_1 + T_2)^-$, the solution travels along $S_L(-1.8)$ to the point M_2 . At $t = (t_0 + T_1 + T_2)^+$, a transition from M_2 to $\Omega_p(0)$ can occur so long as $z_2 < z_-(0)$ (which is the case in this example). Once in the active phase, $z(t)$ will increase slowly until it reaches $z_{hc}(0)$ giving rise to a PIR burst, where a transition back to $S_L(0)$ (i.e., the point M_3) then occurs. The solution will then tend back to the point M_0 , completing the *Mixed* response cycle.

The conditions which guarantee the *Off* part (or rebound burst) of the *Mixed* response will be different than those described in the previous section. To be specific, for the *Off* responses (not *Mixed*) the minimum duration T_S needed to guarantee a rebound burst is given on the left side of Figure 19, and only depends on \bar{I} . For a *Mixed* response, the minimum duration needed to guarantee a rebound burst will also depend on the amplitude and duration of the *On* part (\bar{I}_+ , and T_1). Specifically, the minimum duration needed to guarantee a rebound burst for a constant *On* and *Off* current pulse will depend on $z(t_0 + T_1)$. But this value is different for every (\bar{I}_+, T_1) pair and therefore depends on the *On* part of the stimulus. Nevertheless, we compute this minimum duration, to leading order, using (4.9) to be:

$$T_{SO} = T_{SO}(\bar{I}_+, \bar{I}_-, T_1) = \int_{z(t_0+T_1)}^{z_-(0)} \frac{dz}{h(u_{LB}(z - \bar{I}_-)) - z}. \quad (4.11)$$

Using the (AFS) of (FULL), $z^* = z(t_0 + T_1)$ is defined implicitly by

$$T_1 = \int_{z(0)}^{z^*} \frac{d\gamma}{h(\hat{u}(\gamma)) - (\gamma + \bar{I}_+)} \quad (4.12)$$

so that, in principle, z^* depends on \bar{I}_+ and T_1 , i.e., $z^* = z^*(\bar{I}_+, T_1)$. With this observation,

we can rewrite (4.11) to more clearly delineate the dependence of T_{SO} on $(\bar{I}_+, \bar{I}_-, T_1)$ as

$$T_{SO}(\bar{I}_+, \bar{I}_-, T_1) = \int_{z^*(\bar{I}_+, T_1)}^{z^-(0)} \frac{dz}{h(u_{LB}(z - \bar{I}_-)) - z}. \quad (4.13)$$

Unfortunately, explicit solutions of $z^*(\bar{I}_+, T_1)$ from (4.12) elude us. Numerical methods might be applied to determine $z^*(\bar{I}_+, T_1)$ but the approach taken here instead is to find explicit conditions which are sufficient (but not necessary) for a rebound burst to occur in the constant *On* and *Off* current pulse case.

We would like to obtain sufficient conditions that guarantee an *Off* response given (\bar{I}_+, T_1) . To do this, we first define different regions in the (\bar{I}_+, T_1) plane. These regions are illustrated as (c), (e), (f) and (g) in Figure 23. To define the sufficient conditions in these regions, we use three different definitions of durations.

First, define the active phase duration:

$$T_{AM} = T_{AM}(\bar{I}_+) = \int_{\bar{z}(0) - \bar{I}_+}^{\bar{z}(\bar{I}_+)} \frac{d\gamma}{h(\hat{u}(\gamma)) - (\gamma + \bar{I}_+)}. \quad (4.14)$$

This duration describes the leading-order time of a trajectory entering the active phase at $z = \bar{z}(0) - \bar{I}_+$ to reach a z -value $z = \bar{z}(\bar{I}_+)$ where $\bar{z}(\bar{I}_+)$ is the z -coordinate of the equilibria $\bar{X}(\bar{I}_+) = (\bar{u}(\bar{I}_+), \bar{w}(\bar{I}_+), \bar{z}(\bar{I}_+))$ of (FULL) with $I = \bar{I}_+$. This duration will be used to guarantee $\bar{z}(\bar{I}_+) < z(t_0 + T_1) < z_{hc}(\bar{I}_+)$ for particular choices of T_1 . A numerically computed graph of T_{AM} is illustrated in Figure 23.

Second, define the following two silent phase durations:

$$T_{SX} = T_{SX}(\bar{I}_+, \bar{I}_-) = \int_{\bar{z}(\bar{I}_+)}^{z^-(0)} \frac{dz}{h(u_{LB}(z - \bar{I}_-)) - z}, \quad (4.15)$$

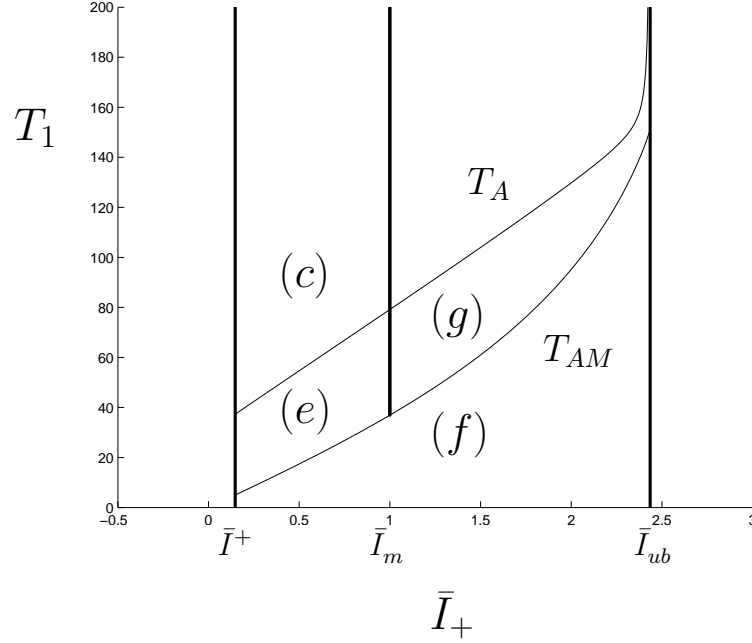


Figure 23. This figure shows the duration T_{AM} for each \bar{I}_+ in the threshold range. This curve gives the minimum duration for the *On* part that will guarantee $\bar{z}(\bar{I}_+) < z(t_0 + T_1) < z_{hc}(\bar{I}_+)$. Notice that this curve lies below the curve T_A for all \bar{I}_+ . For any pair (\bar{I}_+, T_1) in the regions (c), (e), and (g), lower and upper bound curves for the minimum duration T_{SO} needed to guarantee a rebound burst given an *On* part are given by (4.15), and (4.16) respectively. For any pair (\bar{I}_+, T_1) in the region (f), the upper bound curve for the minimum duration T_{SO} needed to guarantee a rebound burst given an *On* part is given by (4.15).

and

$$T_{SH} = T_{SH}(\bar{I}_+, \bar{I}_-) = \int_{z_{hc}(\bar{I}_+)}^{z_-(0)} \frac{dz}{h(u_{LB}(z - \bar{I}_-)) - z}. \quad (4.16)$$

Given the general definition of the silent phase durations (equation (3.18) in Chapter 3 for $T_{SP}(\gamma_{in}, \gamma_{out})$), these are the leading-order durations for trajectories to travel along $\mathbb{S}_L(\bar{I}_-)$ from $z = \bar{z}(\bar{I}_+)$ and $z = z_{hc}(\bar{I}_+)$ to $z = z_-(0)$, respectively. Now that the definitions of T_{AM} , T_{SX} , and T_{SH} have been established, a description of the leading-order dynamics for (\bar{I}_+, T_1) pairs in regions (c), (e), (g), and (f) of Figure 23 can be given.

The durations T_{SX} and T_{SH} will eventually be shown to be lower and upper bounds for the minimum duration T_{SO} needed to guarantee a rebound burst given an *On* part. We use the criteria $\bar{z}(\bar{I}_+) < z(t_0 + T_1) < z_{hc}(\bar{I}_+)$ (see Figure 22a) to see this is true in that simulation) to show that T_{SX} and T_{SH} are the lower and upper bound durations, respectively. The conditions that guarantee $\bar{z}(\bar{I}_+) < z(t_0 + T_1) < z_{hc}(\bar{I}_+)$ have been divided into the regions (c), (e), and (g), and are described in further detail below. Also, a summary of the bounds for T_{SO} in the subsequent discussions and the sufficient conditions (needed to guarantee a rebound burst) for the duration T_2 are summarized in Table 4 for each region of Figure 23.

Assume that $\bar{I}^+ < \bar{I}_+ < \bar{I}_m$, and $T_1 > T_A$. These conditions will guarantee that only a single burst in the *On* part of the solution can occur, and represent the region (c) in Figure 23. For the values of \bar{I}_+ and T_1 in this region, $\bar{z}(\bar{I}_+) < z(t_0 + T_1) < z_{hc}(\bar{I}_+)$. To see this more clearly, consider the maximum and minimum locations of the $z(t)$ -value in the *On* part of the solution of (FULL) for the duration T_1 . While the solution is in the active phase, the $z(t)$ -value will cross the $\bar{z}(\bar{I}_+)$ -value (at time $t = T_{AM}$) and will proceed to the right through the active phase towards the homoclinic value. Once this crossing occurs, the minimum value that $z(t_0 + T_1)$ can attain is $\bar{z}(\bar{I}_+)$. Since $T_1 > T_A$ the solution will undergo a rapid transition to $\mathbb{S}_L(\bar{I}_+)$ at z_{hc} and will continue to travel on $\mathbb{S}_L(\bar{I}_+)$ to the left towards $\bar{X}(\bar{I}_+)$. Thus, the maximum value that $z(t)$ attained is $z_{hc}(\bar{I}_+)$. Knowing that in this region $\bar{z}(\bar{I}_+) < z(t_0 + T_1) < z_{hc}(\bar{I}_+)$, lower and upper bound durations for the minimum duration (needed to guarantee a rebound burst given an *On* part) are given by

T_{SX} and T_{SH} , respectively.

In region (e), similar conditions will apply. In this region, $\bar{I}^+ < \bar{I}_+ < \bar{I}_m$, and $T_{AM} < T_1 < T_A$. Again, while the solution is in the active phase, the $z(t)$ -value will cross the $\bar{z}(\bar{I}_+)$ -value (at time $t = T_{AM}$) since $T_{AM} < T_1 < T_A$, but will not reach the homoclinic point $z_{hc}(\bar{I}_+)$ (since $T_1 < T_A$). Therefore in region (e), $\bar{z}(\bar{I}_+) < z(t_0 + T_1) < z_{hc}(\bar{I}_+)$ and lower and upper bound durations for the minimum duration (needed to guarantee a rebound burst given an *On* part) are once again given by T_{SX} and T_{SH} , respectively.

In region (g) of Figure 23, $\bar{I}_m < \bar{I}_+ < \bar{I}_{ub}$ and $T_{AM} < T_1 < T_A$. For this region, notice that the *On* part of the pulse T_1 terminates before the homoclinic point is reached by the solution. In this case, $\bar{z}(\bar{I}_+) < z(t_0 + T_1)$ (since $T_{AM} < T_1$) and $z(t_0 + T_1) < z_{hc}(\bar{I}_+)$ (since $T_1 < T_A$), and so the durations T_{SX} and T_{SH} can be used for lower and upper bounds in the region (g) as well.

In region (f) of Figure 23, $\bar{I}^+ < \bar{I}_+ < \bar{I}_{ub}$, and $T_1 < T_{AM}$. For these parameters it is certain that $z(t_0 + T_1) < \bar{z}(\bar{I}_+)$. Notice that since $z(t_0 + T_1) < \bar{z}(\bar{I}_+)$, an upper bound duration for the minimum duration needed to guarantee a rebound burst can be found. For the region (f) the upper bound for the minimum duration needed to guarantee a rebound burst given an *On* response is given by T_{SX} . Unfortunately, a useful lower bound value for $z(t_0 + T_1)$ cannot be determined since $z^* = z(t_0 + T_1)$ can have any value in the interval $(\bar{z}(0), \bar{z}(\bar{I}_+))$ for general durations $T_1 < T_{AM}$. Consequently we do not find a useful lower bound duration in this case.

Since the goal is to obtain sufficient conditions on T_2 to guarantee a rebound burst given

(\bar{I}_+, T_1) , the upper bound duration in each region gives such conditions. A summary of the preceding results for each region of Figure 23 can be found in Table 4. In this table the sufficient condition on T_2 is given in the last column for each corresponding region. Thus, given (\bar{I}_+, T_1) , by choosing T_2 appropriately a rebound burst is guaranteed (to leading order) to occur.

Region	Definition	Duration T_{SO} required for PIR	Sufficient Condition
(c)	$\bar{I}^+ < \bar{I}_+ < \bar{I}_m$ $T_1 > T_A$	$T_{SX} < T_{SO} < T_{SH}$	$T_2 > T_{SH}$
(e)	$\bar{I}^+ < \bar{I}_+ < \bar{I}_m$ $T_{AM} < T_1 < T_A$	$T_{SX} < T_{SO} < T_{SH}$	$T_2 > T_{SH}$
(g)	$\bar{I}_m < \bar{I}_+ < \bar{I}_{ub}$ $T_{AM} < T_1 < T_A$	$T_{SX} < T_{SO} < T_{SH}$	$T_2 > T_{SH}$
(f)	$\bar{I}^+ < \bar{I}_+ < \bar{I}_{ub}$ $T_1 < T_{AM}$	$T_{SO} < T_{SX}$	$T_2 > T_{SX}$

Table 4. A description of the sufficient conditions on the duration T_2 needed to guarantee a rebound burst (PIR) given an *On* response resulting from an amplitude \bar{I}_+ and duration T_1 .

Illustrated in Figure 24 are the lower (where appropriate) and upper bound durations for four different (\bar{I}_+, T_1) pairs corresponding to the different regions of Figure 23. For Figures 24a), b), and c), $T_{AM} < T_1$. In a) the value $\bar{I}_+ = 0.5$ was used, while b) shows the bounds when $\bar{I}_+ = 0.8$, and c) shows them when $\bar{I}_+ = 1.5$. In figure c), these bounds are

only valid when $T_{AM} < T_1 < T_A$. For every value of \bar{I}_+ the minimum duration T_2 needed for an *Off* response given an *On* part will lie between these curves. Thus to guarantee a rebound burst when a constant *On* and *Off* current pulse is used, for values of $T_{AM} < T_1$ one can simply choose the duration $T_{SH}(\bar{I}_+)$. In Figure 24d), the upper bound curve T_{SX} is shown for $\bar{I}_+ = 1.5$ when $T_1 < T_{AM}$. In this case, to guarantee a rebound burst when a constant *On* and *Off* current pulse is used, for values of $T_1 < T_{AM}$ one can simply choose the duration $T_2 > T_{SX}(\bar{I}_+)$.

Even though *Mixed* responses can be generated using a constant *On* and *Off* current pulse, they still can be difficult to analyze. Unfortunately, this type of synaptic input may not be very realistic. In the next chapter, a similar *Mixed* response is produced by using a net synaptic input which incorporates some of the shapes from Table 1 and models a more natural synaptic input than the constant *On* and *Off* current pulse.

To summarize this chapter, first we described the numerical solutions of (FULL) which reproduced each response illustrated in Figure 1. For a constant current pulse, certain threshold conditions and durations were needed to guarantee *On* and *Off* responses. Using a similar constant *On* and *Off* current pulse, much of the same analysis was used to deduce certain bounds to guarantee that both an *On* and an *Off* part occur for the *Mixed* response.

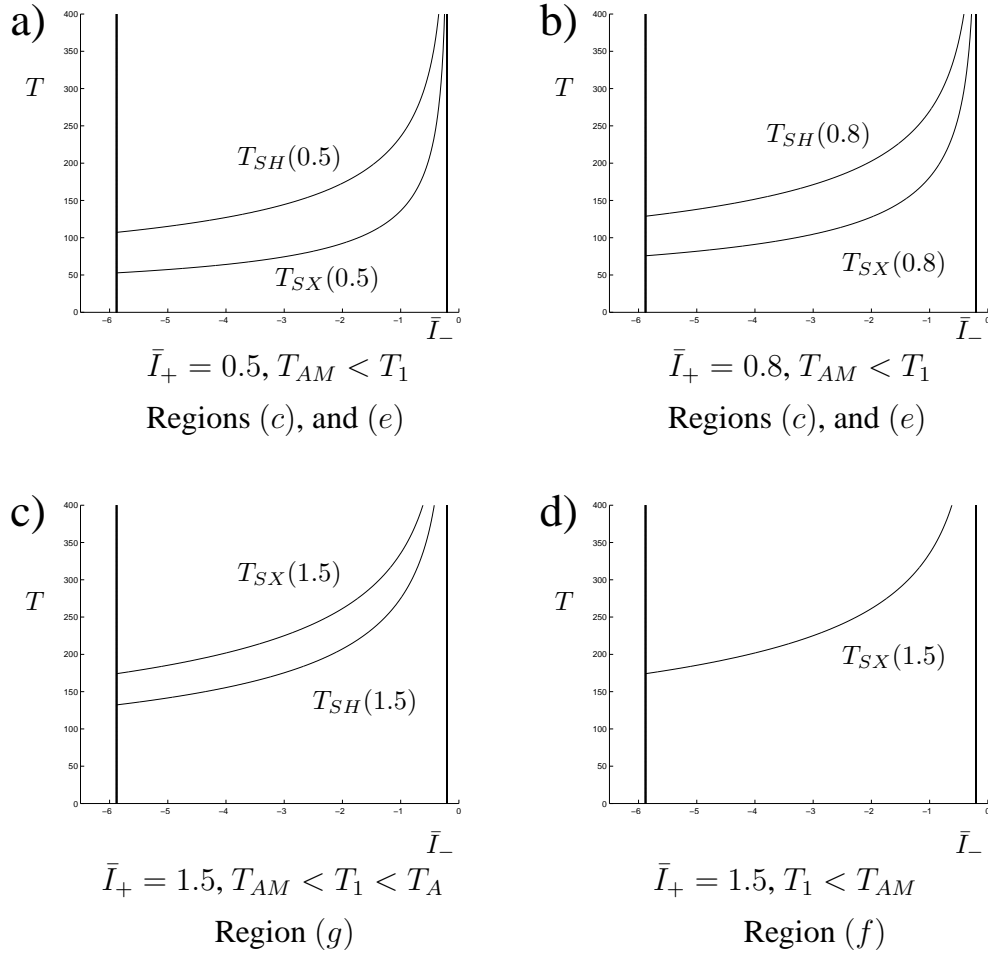


Figure 24. Shows the appropriate lower and upper bound curves T_{SX} and T_{SH} for three different values of \bar{I}_+ . In a) the curves were generated for the value $\bar{I}_+ = 0.5$ and $T_{AM} < T_1$. In b) the curves were generated for the value $\bar{I}_+ = 0.8$ and $T_{AM} < T_1$. In c) the curves were generated for the value $\bar{I}_+ = 1.5$. In each of the figures a), b), the bounds are valid only when $T_{AM} < T_1$. In c) these bounds are valid only when $T_{AM} < T_1 < T_A$. In each a), b), and c) the minimum duration for an *Off* response must lie between the two curves. Figure d) shows the upper bound curve T_{SX} when $\bar{I}_+ = 1.5$ and $T_1 < T_{AM}$.

CHAPTER 5

MONOTONE SLOWLY DECREASING INPUTS

Introduction to *Mixed* Response

The goal of this chapter is to understand and predict the responses of (FULL) when the synaptic input is taken to have monotone slowly decreasing forms similar to those illustrated in Table 1. Since this can be in general very complicated, we will analyze (FULL) only for a certain class of inputs $I(t)$. The development of this theory leads directly to a mathematical formulation for analyzing the class of non-autonomous bursting models presented in (1.1)-(1.2).

First, we give a numerical example of the solutions of (FULL) as a consequence of monotone slowly decreasing inputs. This example shows that (FULL) can reproduce both the *Off* and the *Mixed* responses with synaptic inputs of the forms found in Table 1. To understand these responses, the class of “smooth monotone slowly decreasing” inputs will be defined. In this chapter, the analysis is limited to the effects of synaptic inputs which fall into this class. When inputs from this class are incorporated, we will show that (FULL) (non-autonomous) can be augmented to an autonomous system of four equations. In this study, it is assumed that the augmented system will have two fast-variables and two slow-variables. To analyze the augmented system, and as a result describe the responses of (FULL) under monotone slowly decreasing inputs, we redefine the slow-subsystem and

the averaged-fast-subsystem. These subsystems will then be pieced together to explain the solutions of (FULL) and the dynamics behind each response.

Numerical Example

In this section, we give a numerical example of how (FULL) can reproduce the *Mixed* response. For this example, assume that the stimulus $I(t)$ incorporates the input from both excitatory and inhibitory synapses. In addition, we assume that the cell's receptive field is given two stimuli simultaneously resulting in excitatory and inhibitory synaptic inputs which activate quickly and slowly, respectively. To model this, assume that for the stimulus $I(t) = I_+(t) + I_-(t)$ (compare with (2.3)),

$$I_+(t) = \bar{I}_+(H(t - t_0) - H(t - t_0 - T)) \quad (5.1)$$

$$I_-(t) = \bar{I}_-(H(t - t_0) - H(t - t_0 - T))\left(\frac{\alpha}{e^{-\lambda T} - 1}(e^{-\lambda(t-t_0)} - 1)\right). \quad (5.2)$$

As in the model development described in Chapter 2, $I_+(t)$ defined in (5.1) models excitatory input ($\bar{I}_+ > 0$) to a neuron which activates and inactivates very quickly. In a similar fashion, $I_-(t)$ defined in (5.2) models an inhibitory input (using $\bar{I}_- < 0$ and the form given by equation (2.10)) to a neuron which is slow to activate but quick to inactivate (at $t = t_0 + T$). As a reference, the shapes for $I_+(t)$ and $I_-(t)$ described here correspond to the shapes in rows 1 and 3 of Table 1, respectively. Temporal traces for these inputs are illustrated in Figure 25a) and b). Illustrated in Figure 25c) is the synaptic input given by $I(t) = I_+(t) + I_-(t)$. Notice that when synaptic inputs of the forms illustrated in Figure 25b) and c) are used, (FULL) is a non-autonomous bursting model with a monotone

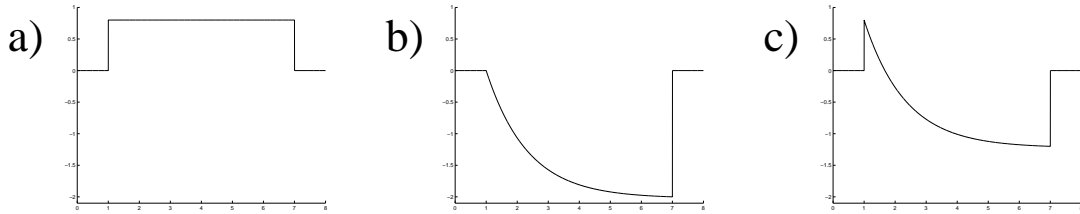


Figure 25. In this figure, a) shows the general behavior for a “Fast” *On* “Fast” *Off* synaptic input as in (5.1). b) shows the “Slow” *On* “Fast” *Off* behavior described in (5.2). c) shows the sum of the inputs from a) and b) $I(t) = I_+(t) + I_-(t)$.

slowly decreasing input.

In all simulations and analyses (in this chapter), the initial conditions are assumed to be on \mathbb{S}_L at the equilibrium value $\bar{X}(0)$. When modeling neurons, recall that this condition assures the cell is at rest before the effects of the input $I(t)$ are taken into account. By using the stimulus $I(t) = I_+(t) + I_-(t)$ defined by (5.1) and (5.2) we can reproduce the *Mixed* response. Figure 26 shows the solution of (FULL) for the inputs represented in Figure 25. Figure 26a) shows the *On* response corresponding to a constant ($\bar{I} = 0.8$) stimulus idealizing a “fast” to activate “fast” to inactivate input. Figure 26b) shows that an *Off* response still occurs when the stimulus is “slow” to activate and “fast” to inactivate. The stimulus input in this case is given by (5.2). Illustrated in Figure 26c) is a *Mixed* response. Notice that the *Mixed* response is similar to the one illustrated in Figure 21 even though a monotone slowly decreasing input was used instead of a constant *On* and *Off* current pulse.

To motivate the analysis needed to describe the responses in Figure 26, a crude description of the cycles in Figures 26b) and c) is given here. Notice that the response illustrated in Figure 26a) has already been analyzed in Chapter 4. In Figure 26b), the synaptic input

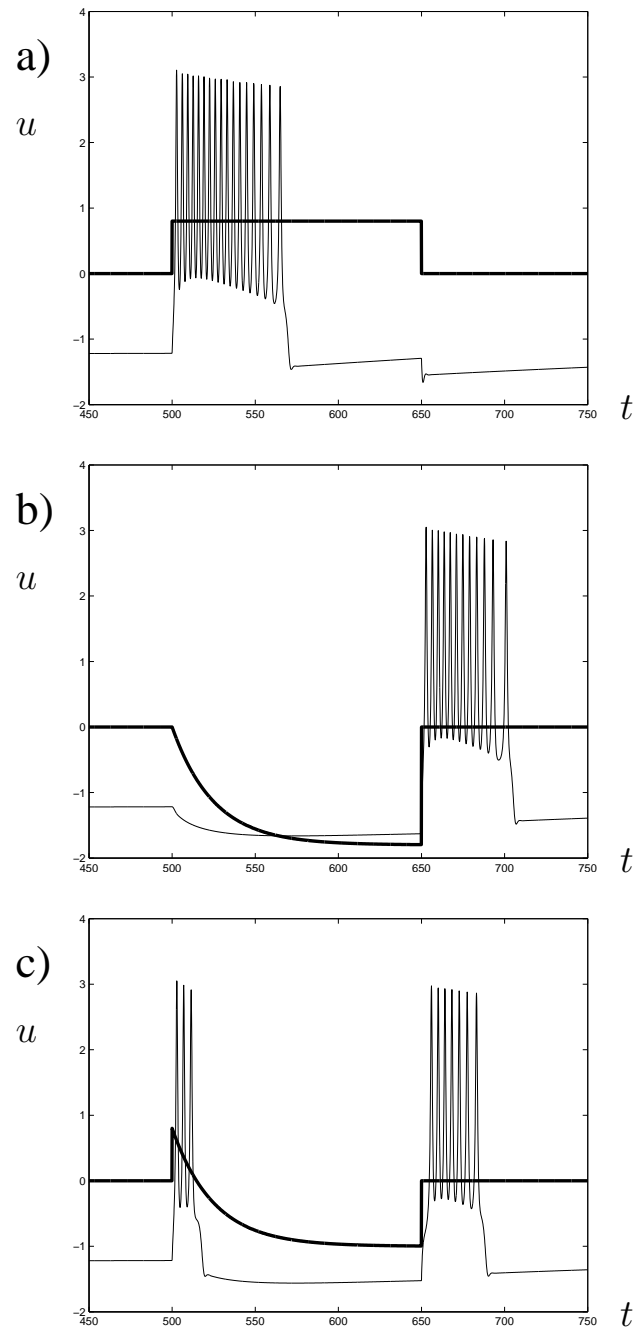


Figure 26. This figure shows that each response in Figure 1 can be reproduced using (FULL). In each figure the thick line represents the net synaptic input. In a), an *On* response is shown. By assuming a “slow” to activate and “fast” to inactivate inhibitory synaptic input, b) shows that (FULL) can reproduce the PIR response. In c), the *Mixed* response is reproduced using a synaptic input which is a combination of the excitatory input from a) and the inhibitory input from b).

is inhibitory and at $t = t_0$ a transition to the slowly varying lower branch occurs. For the entire duration T , the solution travels near the lower branch in the “silent phase” of the cycle. Then, at $t = t_0 + T$ the synaptic input inactivates quickly and a rapid transition to the “active phase” occurs. Even though the *Off* response is similar to that when a constant current pulse is used, the description of the cycle is different due to the slowly activating inhibitory input. Here again, the threshold conditions and durations needed to guarantee an *Off* response will be determined for a monotone slowly decreasing input. To describe these, we define and analyze the slow-subsystem of the non-autonomous system.

The cycle for Figure 26c) is in general similar to the one described for the constant *On* and *Off* current pulse. In this case, a rapid transition to the active phase occurs at $t = t_0$. This transition will occur so long as the threshold conditions for the *On* response (as illustrated in Figure 19) are satisfied. Under certain threshold conditions and input durations, a transition from the active phase to the silent phase will occur at some time \bar{T}_a with $t_0 < \bar{T}_a < t_0 + T$ (which is the case in this example). When this transition occurs, the solution then travels near the lower branch in the silent phase portion of the solution until $t = t_0 + T$. If T is large enough then a rapid transition back to the active phase occurs and the PIR part of the *Mixed* response is manifested. To analyze this type of solution, we use an averaged-fast-subsystem to describe the solution in the active phase and a slow-subsystem to describe the solutions in the silent phase.

Given the responses illustrated in Figure 26, one of the goals of this chapter is to find

certain conditions on the type of inputs that can cause these responses. The numerical example is meant to provide motivation for the possibility that different rates of activation can have an effect on the types of responses seen in neurons. Thus, we will examine questions such as “how do solutions change when different rates of activation (of the synaptic input) are considered?”. To do this, we first give a description of the types of inputs that will be used for the remainder of this study.

Class of Inputs

In this section, we define a different class of inputs that will be used in analyzing (FULL). The objective in this section is to find an initial value problem whose solution is the given synaptic input. This will allow (FULL) (non-autonomous) to be rewritten as an augmented system of autonomous equations. To do this, we first define a class of smooth monotone slowly decreasing inputs. We also assume that the evolution of the input occurs on the slow time scale and can be written as $I(\tau)$ where $\tau = \epsilon t$. Thus, we make the following definition:

Definition 1 *The class of functions \mathbb{C} consists of all those functions $I : \mathbb{R} \rightarrow \mathbb{R}$ such that*

$$I(\tau) = 0 \text{ for all } \tau < t_0 \text{ and for all } \tau > t_0 + T \quad (5.3)$$

$$I(\tau) \in \mathcal{C}^1[t_0, t_0 + T] \quad (5.4)$$

$$I'(\tau) < 0 \text{ for all } \tau \in [t_0, t_0 + T]. \quad (5.5)$$

If we define $I_0 = I(t_0)$ and $I_T = I(t_0 + T)$, then given any $I(\tau) \in \mathbb{C}$ there exists a

function $H_2(I)$, $H_2 : [I_0, I_T] \rightarrow \mathbb{R}$, such that $I(\tau)$ is the solution to

$$\frac{dI}{d\tau} = H_2(I), \quad I(t_0) = I_0 \quad (5.6)$$

for $\tau \in [t_0, t_0 + T]$. Indeed, notice that $I(\tau) \in \mathbb{C}$ implies $I_T < I(\tau) < I_0$ for all $\tau \in [t_0, t_0 + T]$. Moreover, for $I \in \mathbb{C}$, $I'(\tau) < 0$ for all $\tau \in [t_0, t_0 + T]$ implies there exists a function $\Psi(I)$, $\Psi : [I_T, I_0] \rightarrow \mathbb{R}$ with $\Psi'(I) < 0$ and $\tau = \Psi(I(\tau))$ for all $\tau \in [t_0, t_0 + T]$.

Given this, consider $\tau = \Psi(I)$ and differentiate with respect to τ to get

$$1 = \Psi'(I) \frac{dI}{d\tau}.$$

This implies that

$$\frac{dI}{d\tau} = \frac{1}{\Psi'(I)} \equiv H_2(I) \quad (5.7)$$

from which it follows that for $I \in \mathbb{C}$,

$$\frac{dI}{d\tau} = H_2(I), \text{ for all } \tau \in [t_0, t_0 + T]$$

for some $H_2(I)$ as is stated in (5.6). For example, suppose that $I(\tau) = (H(t_0) - H(t_0 + T))(-\tau + I_0)$. Then for $\tau \in (t_0, t_0 + T)$, $I(\tau) \in \mathbb{C}$ with $\Psi(I) = -I + I_0$. For this example $H_2(I) = -1 < 0$ for all $I_T < I < I_0$.

Note that the synaptic inputs $-|I(t)|$ generated in Table 1, rows 3-6, fall within this class. Illustrated in Figure 27 are two such generic examples of functions which are in the class \mathbb{C} . Notice that these shapes are similar to the ones generated by the synaptic model in Chapter 2 which are illustrated in Table 1 (as previously mentioned).

Biophysical inputs typically will have some saturation effects and $I(\tau)$ will have a uniform lower bound no matter how large T is. This implies that there may exist an I_{min}

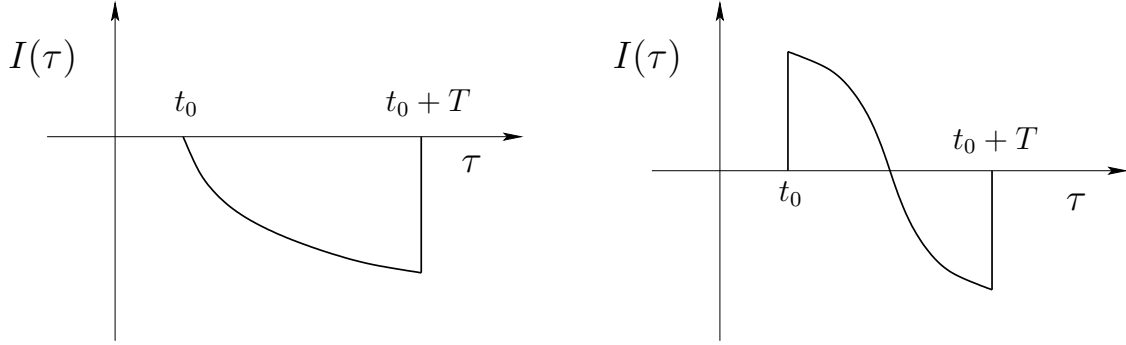


Figure 27. Two examples which illustrate the types of generic inputs that belong to the class \mathbb{C} .

such that $I(\tau) > I_{min}$ for all τ . To consider this issue, we define a sub-class of \mathbb{C} . There are many ways to describe a sub-class of inputs \mathbb{C}_s of \mathbb{C} having this property. What will be important is that they have a lower bound value for all T so that we may define a trapping region later. Here, we choose to make the definition of the sub-class as follows:

Definition 2 *The sub-class of functions, \mathbb{C}_s , consists of any function in \mathbb{C} such that*

$$\exists H_2 \in \mathcal{C}^1[\bar{I}_{lb}, \bar{I}_m] \ni \frac{dI}{d\tau} = H_2(I) \text{ with } I(t_0) = I_0 \text{ for all } \tau \in [t_0, t_0 + T], \quad (5.8)$$

$$\exists I_{min} \ni H_2(I_{min}) = 0, \text{ where } \bar{I}_{lb} < I_{min} < I_0 < \bar{I}_m. \quad (5.9)$$

The values \bar{I}_{lb} and \bar{I}_m are included in the definition since they are the lower bound value for an *Off* response and the value that guarantees only one burst cycle can occur for the *On* response, respectively. As a consequence of the discussion immediately following (5.6), for any $I \in \mathbb{C}_s$ the function H_2 is uniquely defined on $[I_T, I_0]$ where $I_T > I_{min}$. However, there are many \mathcal{C}^1 extensions of $(\Psi'(I))^{-1}$ defined on $[\bar{I}_{lb}, \bar{I}_m]$. The reason \mathbb{C}_s

is defined as it is in Definition 2 is so that I_{min} may be identified as a fixed point of (5.6) and we note the aforementioned (extension) nonuniqueness is not relevant for our goal of finding a trapping region. Rather, what is important is that for the duration $\tau \in [t_0, t_0 + T]$, $I(\tau) > I_{min}$ owing to the fact that $I \in \mathbb{C}_s$.

The restrictions (in the class \mathbb{C}_s) imposed on I , and as a consequence on $H_2(I)$, are designed to prevent solutions from having potentially unrealistic dynamics when modeling neurons. This sub-class of inputs will be referred to as “generic applicable” inputs. The term “generic applicable” is used to describe inputs that are realistic with respect to the membrane potential ranges in the model. Since in this class $\bar{I}_{lb} < I_{min} < I(\tau) < \bar{I}_m$ for all $\tau \in [t_0, t_0 + T]$, issues concerning the basins of attraction (of the periodic orbits as discussed in Chapter 3) will not arise under these restrictions. Furthermore, since $I(\tau) < \bar{I}_m$ the solution will not undergo multiple burst cycles (as discussed in Chapter 4). Therefore, responses similar to those illustrated in Figures 17a), c) and d) and Figure 20 will not occur as a result of a “generic applicable” input.

Now that the class \mathbb{C}_s of inputs has been defined, an example of a specific function $H_2 = H_2(I)$ is given. This example is given to bridge the modeling in Chapter 2 and the specific forms illustrated in Table 1 with a corresponding input from the class \mathbb{C}_s and its corresponding $H_2(I)$ function. Consider the synaptic input given by

$$I_1(\tau) = \frac{\tilde{b}}{a}(1 - e^{-\tilde{a}(\tau-t_0)}) + I_0 e^{-\tilde{a}(\tau-t_0)} \quad (5.10)$$

for $\tau \in (t_0, t_0 + T)$, where $\tilde{a} > 0$ and $\tilde{b} < 0$. Notice that $I_1(\tau) \in \mathbb{C}_s$ so long as

$$\frac{\tilde{b}}{\tilde{a}} < I_0 < \bar{I}_m.$$

When this is the case, $I_1(\tau)$ is the solution to the initial value problem given by;

$$\frac{dI}{d\tau} = H_2(I) = -\tilde{a}I + \tilde{b}, \text{ with } I(t_0) = I_0, \text{ and } \tilde{a} > 0, \tilde{b} < 0. \quad (5.11)$$

Notice that $H_2(I) < 0$ for all $I \in (\frac{\tilde{b}}{\tilde{a}}, I_0)$, and that for this example,

$$I_{min} = \frac{\tilde{b}}{\tilde{a}}. \quad (5.12)$$

The function $H_2(I)$ defined in (5.11) will be used as an example in the analysis of the solutions of (FULL). Illustrated in Figure 28 is the function $I_1(\tau)$ for $\tau \in (t_0, t_0 + T)$. Notice that the solution to (5.11) has the same form as the synaptic input illustrated in Figures 26b) and c) (for appropriate constants). Regardless, for all $I \in \mathbb{C}$, whenever $I(\tau)$ is the solution to the initial value problem (5.6), (FULL) can be augmented to a system of four equations. For the remainder of the chapter, we assume this is the case and that the net synaptic input felt by the cell as a result of a stimulus is the solution of the initial value problem (5.6). In the following section we describe and analyze this augmentation.

Augmentation of (FULL)

Recall for a monotone slowly decreasing input, (FULL) is a non-autonomous bursting

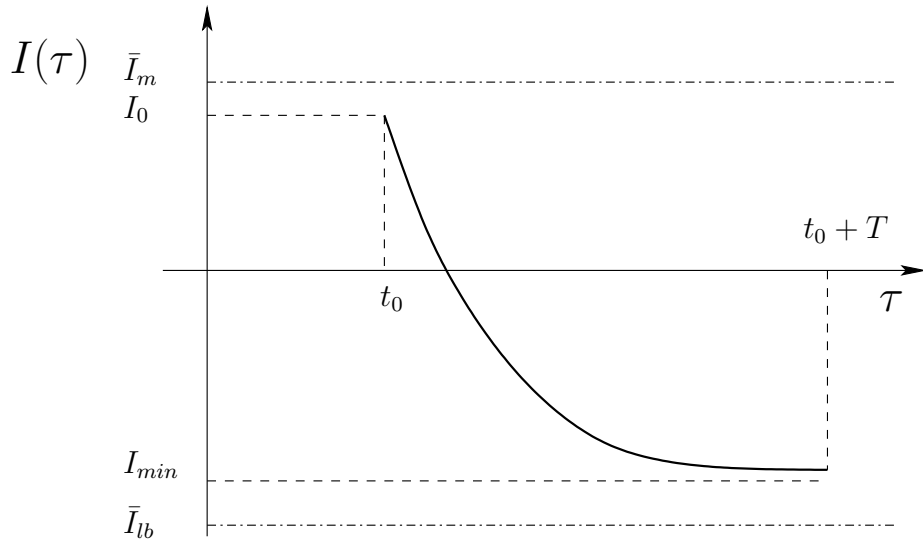


Figure 28. This figure shows a “generic applicable” input which is the solution to the initial value problem given by equation (5.11). In this case $\bar{I}_{lb} < I_{min} < I_0 < \bar{I}_m$. Also illustrated are the times $t = t_0$ and $t = t_0 + T$ along with the thresholds $I = \bar{I}_{lb}$ and $I = \bar{I}_m$ (as the dash-dot lines).

model with the form

$$\frac{du}{dt} = f(u) - w - z + I(\tau) \quad (5.13)$$

$$\frac{dw}{dt} = g(u) - w \quad (5.14)$$

$$\frac{dz}{dt} = \epsilon(h(u) - z), \quad 0 < \epsilon \ll 1 \quad (5.15)$$

By using synaptic inputs which belong to the class \mathbb{C} , this non-autonomous model can be augmented to the following autonomous system of four equations with two “fast” variables

and two “slow” variables;

$$\frac{du}{dt} = f(u) - w - z + I \quad (5.16)$$

$$\frac{dw}{dt} = g(u) - w \quad (5.17)$$

$$\frac{dz}{dt} = \epsilon(h(u) - z) \quad (5.18)$$

$$\frac{dI}{dt} = \epsilon H_2(I), \quad 0 < \epsilon \ll 1, \quad (5.19)$$

where $H_2(I) < 0$ for all $I_T < I < I_0$. Notice that the two systems above are equivalent under the assumption that $I(\tau) \in \mathbb{C}$ (for the times $t = (t_0, t_0 + T)$). For purposes of reference the augmented system in (5.16)-(5.19) will be referred, to as (FULLa).

To recapitulate, given a “generic applicable” synaptic input in (FULL), we found an equivalent augmented system (FULLa). We will use the subsystems of (FULLa) when describing the *Mixed* response. First, a rapid transition from $I = 0$ to $I = I_0$ occurs at $t = t_0$. When this transition occurs, the leading order trajectories are given by (FS). Notice that when the variable $\gamma = z - I$ is introduced, the fast-subsystem of (FULLa) is identical to the fast-subsystem of (FULL). Therefore (FS), as defined in Chapter 3, describes the leading order trajectories of (FULLa) as well. Therefore, the solution will be attracted to the periodic orbits for sufficiently large I_0 .

To describe how the solution travels along the active phase, we analyze the averaged-fast-subsystem of (FULLa). Once this has been done, assuming a transition from the active phase to the silent phase occurs at some time \bar{T}_a , where $t_0 < \bar{T}_a < t_0 + T$, the solution will then travel along the silent phase. Once this transition occurs, the leading order trajectories

will be given by the slow-subsystem of (FULLa). Recall that for the *Mixed* response, a PIR component must also occur. To assure that PIR occurs, we will find conditions which guarantee that the solution will enter the PIR region. The PIR region is a region in the (z, I) plane where upon release of the stimulus (or in this case a transition from $I = I(t_0 + T)$ back to $I = 0$) a transition to the active phase occurs. The goal is then to piece together the active phase analysis with the silent phase analysis and to find conditions which causes either an *Off* or a *Mixed* response. In the following sections we define and analyze each subsystem individually, followed by a section where they are combined together.

Averaged-Fast-Subsystem (AFSa)

In this section, the averaged-fast-subsystem (AFSa) associated with (FULLa) is defined. Here, (AFSa) describes the leading order approximation for the z and I components of (FULLa) for slow times $\tau = \mathcal{O}(1)$. Once we define (AFSa), we give sufficient conditions that guarantee a transition of solutions from the active phase to the silent phase at the homoclinic point.

The details of the assumptions, expansions, and multiple scales procedure used to derive (AFSa) can be found in [32]. By applying these procedures to (FULLa), (AFSa) is derived to be:

$$\frac{dz}{d\tau} = \hat{H}_1(z, I) = h(\hat{u}(z - I)) - z, \quad (5.20)$$

$$\frac{dI}{d\tau} = \hat{H}_2(I) = H_2(I), \quad (5.21)$$

where \hat{u} is defined by equation (3.25). Notice that in this form, the average \hat{u} of u depends

on both z and I . Since one of the goals is to understand and analyze the solutions of (FULLa), it will be useful to investigate (FULLa) in terms of the variable γ instead of z .

Then, (FULLa) can be rewritten in terms of γ as follows:

$$\frac{du}{dt} = f(u) - w - \gamma \quad (5.22)$$

$$\frac{dw}{dt} = g(u) - w \quad (5.23)$$

$$\frac{d\gamma}{dt} = \epsilon(h(u) - (\gamma + I) - H_2(I)) \quad (5.24)$$

$$\frac{dI}{dt} = \epsilon H_2(I), \quad 0 < \epsilon \ll 1. \quad (5.25)$$

Now, let equations (5.22)-(5.25) be referred to as (FULLa) $_{\gamma}$ with associated averaged-fast-subsystem (AFSa) $_{\gamma}$ defined by

$$\frac{d\gamma}{d\tau} = \widehat{\mathcal{H}}_1(\gamma, I) = h(\hat{u}(\gamma)) - (\gamma + I) - H_2(I), \quad (5.26)$$

$$\frac{dI}{d\tau} = \widehat{H}_2(I) = H_2(I). \quad (5.27)$$

For initial conditions sufficiently close to the fast-subsystem periodic orbits Ω_p , solutions of (AFSa) $_{\gamma}$ are the leading order asymptotic approximations of (γ, I) in (FULLa) $_{\gamma}$ for times $\tau = \mathcal{O}(1)$ so long as $(\gamma(\tau), I(\tau)) \in \mathbb{S}_A$ where

$$\mathbb{S}_A = \{(\gamma, I) : \gamma_{hb} < \gamma < \gamma_{hc}\}.$$

With the solution illustrated in Figure 26c) in mind, the goal of this section is to find conditions that guarantee a transition from the active phase entry point to the homoclinic point in finite time. This will guarantee that the solution travels along the active phase and that a transition to the silent phase occurs for some time \bar{T}_a where $t_0 < t_0 + \bar{T}_a < t_0 + T$. When such a transition occurs, the solution will exhibit the *On* part of the *Mixed* response.

Given an $I(\tau) \in \mathbb{C}_s$, what conditions will guarantee a transition from the entry value γ_0 to the exit value γ_{hc} ? To answer this question, first recall that $H_2(I) < 0$ for all $I \in (I_{min}, I_0)$ and that $I_{min} < I(\tau) < I_0$ for all $\tau \in (t_0, t_0 + T)$. Under these assumptions

$$\frac{d\gamma}{d\tau} = h(\hat{u}(\gamma)) - \gamma - I - H_2(I) \quad (5.28)$$

$$> h(\hat{u}(\gamma)) - \gamma - I, \quad (5.29)$$

since $H_2(I) < 0$ as long as $I_{min} < I < I_0$. Also, since $\gamma_0 < \gamma < \gamma_{hc}$, it follows that

$$-\gamma_0 > -\gamma > -\gamma_{hc}. \quad (5.30)$$

Similarly, since $I_{min} < I(\tau) < I_0 < \bar{I}_m$ for all $\tau \in (t_0, t_0 + T)$, it follows that

$$-I_{min} > -I > -\bar{I}_m. \quad (5.31)$$

Using the inequality (5.29), with (5.30), and (5.31), it follows that

$$\frac{d\gamma}{d\tau} > h(\hat{u}(\gamma)) - \gamma_{hc} - \bar{I}_m. \quad (5.32)$$

Since the goal of this section is to find sufficient conditions that will guarantee a transition from γ_0 to γ_{hc} in the active phase, the objective is to show that $\frac{d\gamma}{d\tau} > r > 0$ for some r and all $\gamma \in (\gamma_0, \gamma_{hc})$. If such an r exists, then $\frac{d\gamma}{d\tau}$ will be uniformly bounded below and the solution must travel from γ_0 to γ_{hc} in finite time. In order to show that such an r exists, we use information about $\hat{u}(\gamma)$. Specifically, although it cannot be verified analytically, numerical confirmation that $u_{hb} > \hat{u}(\gamma) > u_{hc}$ for all $\gamma \in (\gamma_{hb}, \gamma_{hc})$ is shown in Figure 12. Thus, the numerical evidence supports the assertion that $\hat{u}(\gamma) > u_{hc}$ for all $\gamma \in (\gamma_{hb}, \gamma_{hc})$.

When the assumption $u_{hb} > \hat{u}(\gamma) > u_{hc}$ is valid, it follows that

$$\frac{d\gamma}{d\tau} > h(u_{hc}) - \gamma_{hc} - \bar{I}_m \quad (5.33)$$

for all $\gamma \in (\gamma_{hb}, \gamma_{hc})$. Thus, it remains to be shown that there exists an r such that $h(u_{hc}) - \gamma_{hc} - \bar{I}_m > r > 0$. When the parameter values $\beta = 4$, $\alpha = -1.5$ are used,

$$h(u_{hc}) - \gamma_{hc} - \bar{I}_m = r = 1.4352 > 0, \quad (5.34)$$

and a uniform positive lower bound on $\frac{d\gamma}{d\tau}$ exists. Notice that (5.34) was calculated for the “standard” parameter values $\beta = 4$ and $\alpha = -1.5$. Therefore, r depends on these slow parameter values. When these parameters are considered generally, the following inequality must be satisfied:

$$\beta(u_{hc} - \alpha) - \gamma_{hc} - \bar{I}_m > 0. \quad (5.35)$$

Notice that the left hand side of this inequality is simply a lower bound for $\frac{d\gamma}{d\tau}$ and that many different (β, α) -pairs will satisfy (5.35). For this study all simulations and analyses are done with the “standard” choice $(\beta, \alpha) = (4, -1.5)$.

Given the discussion above, the following Lemma has been proven:

Lemma 3 *If $H_2(I) < 0$ for all $I \in (I_{min}, I_0)$ and $\beta(u_{hc} - \alpha) - \gamma_{hc} - \bar{I}_m > 0$, as long as $\hat{u}(\gamma) > u_{hc}$ then there exists an r independent of I and γ such that*

$$\frac{d\gamma}{d\tau} = \hat{\mathcal{H}}_1(\gamma, I) > r > 0 \text{ for all } \gamma \in (\gamma_0, \gamma_{hc}). \quad (5.36)$$

As a consequence, since $\hat{\mathcal{H}}_1$ is uniformly bounded away from 0, there exists a $\bar{T}_a < \infty$ such that $\gamma(\bar{T}_a) = \gamma_{hc}$ (i.e., an escape from the active phase to the silent phase must occur

in finite time). Notice that such a transition will occur regardless of the form of $H_2(I)$ (as long as $H_2(I) < 0$). After this transition occurs, the leading order analysis is no longer given by (AFSa) but is given by the slow-subsystem of (FULLa) (defined in a later section).

To recap, in Lemma 3, $(\text{FULLa})_\gamma$ was used to “prove” that a transition from the entry point γ_0 to the exit point γ_{hc} must occur in finite time. Since $(\text{FULLa})_\gamma$ and (FULLa) represent the same system (with different choice of variables), it will be useful to visualize such transitions in the (z, I) -plane. To do this, first a description of the projection, in the (z, I) -plane, of the trajectories of (FULLa) in the active phase is given. To illustrate the solutions of (FULLa) along the active phase, Figure 29 shows a caricature of the projected trajectories in the active phase. Shown in this figure are the two curves Γ_0 and Γ_{hc} representing $\gamma_0 = z_0 - I$ and $\gamma_{hc} = z_{hc} - I$, respectively. Also shown is a trajectory $\hat{\gamma}_X$ of (AFSa) showing a transition from the entry point \mathbf{X}_0 to the exit point \mathbf{X}_{hc} . In order to be precise when describing the trajectories of (AFSa), we define the map $\hat{\Phi}$ relating these entry and exit points. Given that the hypotheses of Lemma 3 are satisfied, a trajectory of (AFSa) that starts at $\mathbf{X}_0 = (z, I)$, on the curve

$$\Gamma_0 = \{(z, I) : z - I = \gamma_0\}, \quad (5.37)$$

must terminate at \mathbf{X}_{hc} , on the curve

$$\Gamma_{hc} = \{(z, I) : z - I = \gamma_{hc}\}. \quad (5.38)$$

This defines a map $\hat{\Phi} : \mathbb{R}^2 \rightarrow \mathbb{R}^2$, such that $\mathbf{X}_{hc} = \hat{\Phi}(\mathbf{X}_0)$.

Now that the definitions for the transitions have been defined above, the goal is to show

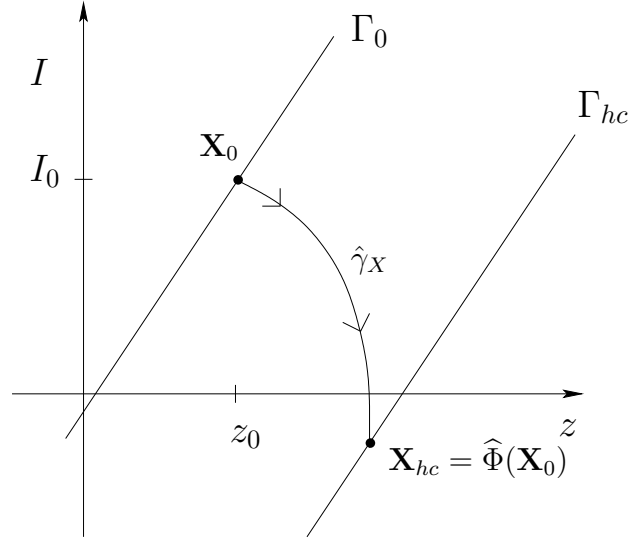


Figure 29. This figure shows a caricature of a typical trajectory of (FULLa) projected in the (z, I) -plane. The map $\hat{\Phi}$ describes an active phase transition from an initial point \mathbf{X}_0 to the terminating point \mathbf{X}_{hc} .

that the active phase duration \bar{T}_a can be computed for certain functions $H_2(I)$. Consider the function $H_2(I) = -\tilde{a}I + \tilde{b}$ introduced in (5.11). When this function is used in (FULLa), (AFSa) is

$$\frac{dz}{d\tau} = \hat{H}_1(z, I) = h(\hat{u}(z - I)) - z, \quad (5.39)$$

$$\frac{dI}{d\tau} = \hat{H}_2(I) = -\tilde{a}I + \tilde{b}. \quad (5.40)$$

Before the active phase duration is computed for this example, a comparison of the true solution and the leading order solution is given. First, to demonstrate how (AFSa) approximates the solutions of (FULLa) in the active phase, both solutions are illustrated in Figure 30. This figure shows an active phase trajectory of (FULLa) projected onto the (z, I) -plane along with the (AFSa) approximation. These solutions have been generated

for the function $H_2(I) = -\tilde{a}I + \tilde{b}$ with $\tilde{a} = 1$ and $\tilde{b} = -1$. In Figure 30a), $\epsilon = 0.0025$ has been used. Notice that when $\epsilon = 0.0005$ is used, the projection of (FULLa) is asymptotically converging to (AFSa). Note that in both Figure 30a) and b), the initial conditions for both trajectories were chosen to lie on Γ_0 with $(z_0, I_0) = (\bar{z}(0), 0.8)$. In each figure the oscillatory curve is the projection of (FULLa) while the smooth curve is (AFSa).

Having established that (AFSa) well approximates (FULLa), the active phase duration can now be calculated. When the function $H_2(I) = -\tilde{a}I + \tilde{b}$ is considered, the active phase duration \bar{T}_a will depend on \tilde{a} , \tilde{b} , and I_0 , and as such $\bar{T}_a = \bar{T}_a(I_0, \tilde{a}, \tilde{b})$. The (leading order) active phase duration is found by using (5.39)-(5.40) to determine the time needed for the solution to travel from Γ_0 to Γ_{hc} . Even though equation (5.40) is decoupled and can be solved explicitly for $I(\tau)$, an analytic formulation for the active phase duration cannot be given since \hat{u} in (5.39) can only be computed numerically. If $\mathbf{X}_{hc} = (z_{hc}, I_{hc})$ were known, then the active phase duration can be explicitly computed using the solution to (5.40) and by solving

$$I_{hc} = \frac{\tilde{b}}{\tilde{a}}(1 - e^{-\tilde{a}(\tau-t_0)}) + I_0 e^{-\tilde{a}(\tau-t_0)} \quad (5.41)$$

for τ . Similarly, if the active phase duration were known, then the values of the point $X_{hc} = (z_{hc}, I_{hc})$ can also be calculated using the same equation. Unfortunately, a general theory for analytically computing either X_{hc} or \bar{T}_a eludes us. Instead, we give a numerical computation of \bar{T}_a for all $I_0 \in (\bar{I}^+, \bar{I}_m)$ with two different parameter sets (\tilde{a}, \tilde{b}) . Once \bar{T}_a has been computed, (5.41) can be used to find the location of \mathbf{X}_{hc} .

To obtain these durations, we solved (AFSa) using an explicit one step Runge-Kutta

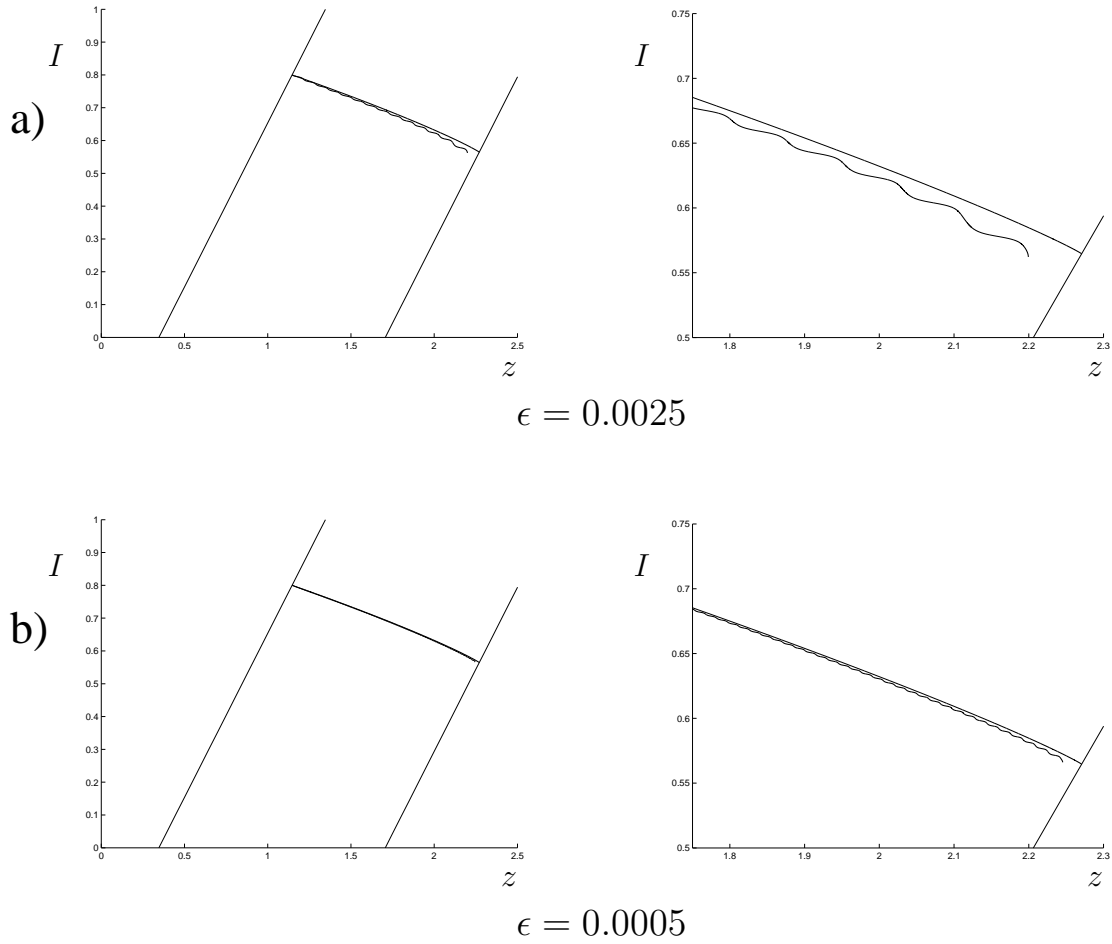


Figure 30. Figure a) shows the active phase trajectory of (FULLa) projected on the (z, I) -plane (oscillatory curve) and the trajectory generated by (AFSa) (smooth curve) when $H_2(I) = -\tilde{a}I + \tilde{b}$. Both figures show the same trajectories on two different intervals. In a), $\epsilon = 0.0025$ with $\tilde{a} = 1$, and $\tilde{b} = 1$. Figure b) shows the active phase trajectory of (FULLa) projected on the (z, I) -plane and the trajectory generated by (AFSa) when $\epsilon = 0.0005$ (with $\tilde{a} = 1$, and $\tilde{b} = 1$) is used. Notice that when a smaller ϵ is used, (AFSa) is a “very good” approximation of the projected active phase trajectory.

solver in Matlab (*ode45*) until the solution was sufficiently close to Γ_{hc} . Notice that at each timestep, the $\hat{u}(z - I)$ -value was needed. Recall that AUTO was used to compute $\hat{u}(\gamma)$ for the range $(\gamma_{hb}, \gamma_{hc})$. In this latter computation, the range $(\gamma_{hb}, \gamma_{hc})$ was discretized to find the \hat{u} -values at each appropriate mesh point. To approximate \hat{u} at non-mesh points, a

‘spline’ interpolation was used in Matlab (*interp1*). The \hat{u} -values of the interpolation were then used for the right hand side of (AFSa). Once the solution of (AFSa) was computed ($z(\tau)$, and $I(\tau)$), the time needed to travel from the initial value \mathbf{X}_0 to the homoclinic point \mathbf{X}_{hc} (or close to) could be calculated.

Illustrated in Figure 31 is the active phase duration as a function of I_0 with the values $(\tilde{a}, \tilde{b})_1 = (1, -1.3)$ and $(\tilde{a}, \tilde{b})_2 = (5, -6.5)$. The smaller the value of \tilde{a} , the slower the rate of decay of the input, and thus the longer the active phase duration will be. Although Figure 31 shows that this difference is small, the active phase duration will change in accordance to the parameter \tilde{a} . For the examples illustrated in Figure 31, the ratio $\frac{\tilde{b}}{\tilde{a}}$ was chosen to be the same for each pair. This guarantees that the equilibrium of the equation (5.40), or I_{min} , is the same in both examples.

In this section it was shown that under certain assumptions, an active phase trajectory (in the (z, I) -plane) travels from Γ_0 to Γ_{hc} in finite time and that the active phase duration can be calculated using the averaged-fast-subsystem. Recall that in this study one of the goals was to find sufficient conditions that will guarantee a *Mixed* response. With this goal in mind, (AFSa) describes the *On* part of a mixed response. When an active phase transition from Γ_0 to Γ_{hc} occurs, the solution to (FULLa) travels near the periodic orbits and proceeds towards the homoclinic point where a rapid transition to the silent phase then occurs. When such a transition occurs, the trajectories will then be described by the slow-subsystem of (FULLa). As such, the slow-subsystem for (FULLa) is described and sufficient conditions that will guarantee a PIR response are given in the next section.

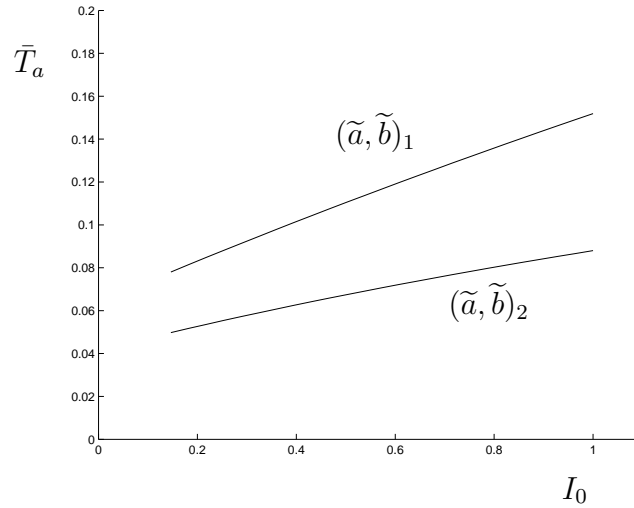


Figure 31. This figure shows the active phase duration \bar{T}_a as a function of the initial value I_0 . The duration was computed for two parameter sets: $(\tilde{a}, \tilde{b})_1 = (1, -1.3)$ and $(\tilde{a}, \tilde{b})_2 = (5, -6.5)$. Since the value \tilde{a} corresponds to the decay rate of the input, notice that when \tilde{a} is smaller, the active phase duration is longer.

Slow-Subsystem (SSa)

In this section, the slow-subsystem (SSa) associated with (FULLa) is defined. The slow-subsystem (SSa) describes the slow flow of the trajectories of (FULLa) along the silent phase. Using a slow time transformation $\tau = \epsilon t$ in (FULLa) and then setting $\epsilon = 0$, the slow-subsystem (SSa) for the augmented system is given by:

$$z - I = f(u) - w, \quad (5.42)$$

$$w = g(u), \quad (5.43)$$

$$\frac{dz}{d\tau} = h(u) - z, \quad (5.44)$$

$$\frac{dI}{d\tau} = H_2(I). \quad (5.45)$$

Here (SSa) is defined as (5.42)-(5.45) for $u < u_-$.

Using the fact that equations (5.42) and (5.43) combine to give the same algebraic condition as described by (3.15), notice that the lower branch manifold for (SSa) is given by

$$\mathbb{S}a_L = \{(u, w, z, I) : z - I = G(u), w = g(u), u < u_-\} \quad (5.46)$$

where $G(u)$ is described by (3.3). To leading order, the silent phase trajectories of (FULLa) are close to $\mathbb{S}a_L$, and recall, if $\mathbf{X} = (u, w, z, I) \in \mathbb{S}a_L$, then the u component is given by u_{LB} (to leading order) defined in (3.16) for $\gamma = z - I$. Using this condition in equation (5.44), (SSa) becomes:

$$\frac{dz}{d\tau} = H_1(z, I) = h(u_{LB}(z - I)) - z, \quad (5.47)$$

$$\frac{dI}{d\tau} = H_2(I). \quad (5.48)$$

Notice that $u_{LB}(z - I)$ is smooth for all $z - I > z_- = 1$.

Given the system defined by (5.47) and (5.48) with the fact that $H_2(I_{min}) = 0$, an equilibria for (SSa) will exist if $H_1(z, I_{min}) = 0$ (for some z). Although (SSa) may have an equilibria, solutions to (SSa) will never reach that equilibria since for $I_{min} < I(\tau) < I_0$ for all $\tau \in (t_0, t_0 + T)$. This fact will play an important role in describing the flow in the silent phase. Before a description of the flow for (SSa) is given, we derive an expression for the z -nullcline of (SSa) in the (z, I) -plane. Setting the right hand side of (5.47) equal to zero gives:

$$h(u_{LB}(z - I)) - z = 0$$

from which it follows

$$u_{LB}(z - I) = h^{-1}(z) = \frac{z}{\beta} + \alpha.$$

Since u_{LB} is the lower branch solution of

$$(z - I) = G(u) = -u^3 + 3u + 3,$$

it follows that

$$u_{LB}(z - I) = G^{-1}(z - I),$$

and thus

$$I = z - G(h^{-1}(z)) \equiv \Theta(z), \quad (5.49)$$

where $\Theta(z) = z - (-\frac{z}{\beta} + \alpha)^3 + 3((\frac{z}{\beta} + \alpha) + 1)$. Equation (5.49) describes the z -nullcline in the (z, I) -plane valid for $z - I > z_-$, and has a form similar to (4.8). This curve will be referred to as the z -null curve. Illustrated in Figure 32 is z -null curve along with the Γ_- and the Γ_{hc} curves as references. In this figure, for any (z, I) -pairs on the right of z -null, $\frac{dz}{d\tau} < 0$ and the flow is towards the left. For any (z, I) -pairs on the left of z -null, $\frac{dz}{d\tau} > 0$ and the flow is towards the right. Also illustrated in this figure is the equilibria of (SSa) labeled \bar{X} . Notice that the location of \bar{X} occurs where I_{min} and $I = \Theta(z)$ intersect.

PIR Region

Now that the appropriate curves have been defined, we give a description of the conditions that will guarantee PIR for both the *Off* and the *Mixed* responses. The conditions which guarantee PIR upon the release of a stimulus depend on the duration of the stimulus and on certain amplitude thresholds of the input. When investigating monotone slowly

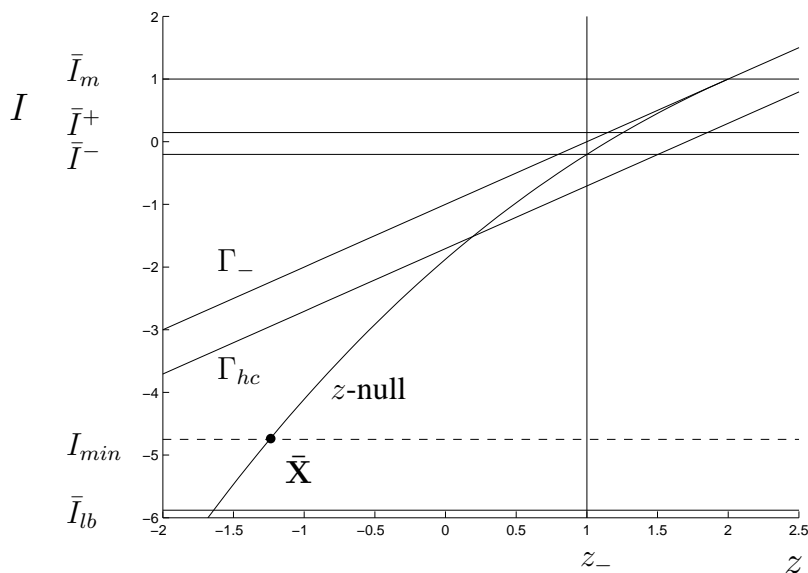


Figure 32. This figure shows the z -null curve for (SSa) along with the Γ_- and the Γ_{hc} curves. Also shown is the $z_- = 1$ curve (vertical curve) and the threshold values; \bar{I}_m , \bar{I}^+ , \bar{I}^- , I_{min} , and \bar{I}_{lb} . Also labeled is the position of the equilibria of (SSa). These curves will play an important role when describing the trajectories of (SSa).

decreasing inputs, these conditions are in general difficult to track. With this in mind, the goal in this section is to find sufficient conditions which guarantee PIR.

To do this, the values $z_T = z(t_0 + T)^-$ and $I_T = I(t_0 + T)^-$ will play an important role in a PIR response. These values are the location of solutions of (FULLa) in the (z, I) -plane just before the effects of the synaptic inputs (or stimuli) are turned off. When this occurs, the input I undergoes a rapid transition from $I_T = I(t_0 + T)^-$ to $I(t_0 + T)^+ = 0$. Thus when describing conditions for PIR, the stability of (FS) for each z -value when $I = 0$ must be determined. Recall (from Chapter 3) that when

$$z_{hb} < z < z_-,$$

the leading-order trajectories of (FULLa) will be attracted to the periodic orbits Ω_p . Thus,

to guarantee PIR, $z_T = z(t_0 + T)^-$ must satisfy

$$z_{hb}(0) < z_T < z_-(0). \quad (5.50)$$

In addition to these threshold conditions on z_T , there are conditions on $I_T = I(t_0 + T)^-$ that must also be satisfied. Recall (from Chapter 4) that to guarantee PIR, the conditions of (4.7) must be satisfied. These conditions were found as a result of a constant current pulse, but for PIR what really matters is that at $t = (t_0 + T)^-$, $I_T = I(t_0 + T)^-$ satisfies

$$\bar{I}_{lb} < I_T < \bar{I}^-. \quad (5.51)$$

Conditions (5.50) and (5.51) are necessary conditions for PIR and they create a region in the (z, I) plane defined as

$$\Omega_{PIR} = \{(z, I) : z_{hb}(0) < z < z_-(0), \bar{I}_{lb} < I < \bar{I}^-\}. \quad (5.52)$$

Whenever $(z_T, I_T) \in \Omega_{PIR}$, then a rapid transition to Ω_p will occur upon release of an input.

Illustrated in Figure 33 is a sketch of the region Ω_{PIR} along with the z -nullcline, the curve Γ_- , and three different paths, labeled (a), (b), and (c). These paths represent “typical” projections of solutions of (FULLa) on the slow subsystem manifold. Each of the projections have the end point P_i labeled, for $i = a, b, c$, to help describe the different scenarios when seeking a PIR response. Notice that since the z -nullcline intersects Ω_{PIR} , any path starting on the right of this curve will remain on the right for all $\tau \in (t_0, t_0 + T)$.

Path (a) in Figure 33 shows the path of a solution when $I(\tau) > \bar{I}^-$ for all $\tau \in (t_0, t_0 + T)$. Notice that in this case, upon release of the input, the point $P_a = (z_T, I_T)_a$ does not lie

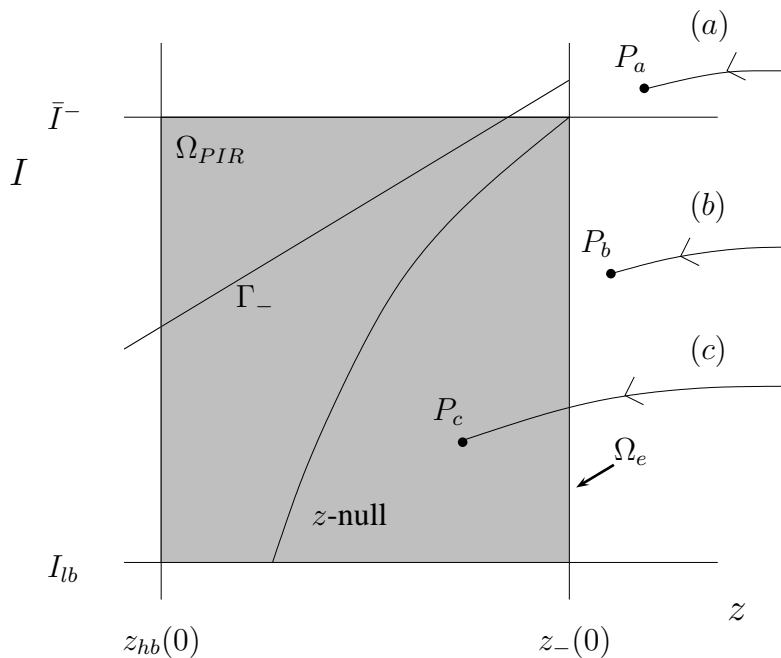


Figure 33. This figure shows a sketch of the region Ω_{PIR} defined by $z_{hb}(0) < z < z_-(0)$ and $\bar{I}_{lb} < I < \bar{I}^-$. Also illustrated in this figure are the z -nullcline for (SSa) along with the Γ_- curve. Three different paths are labeled (a), (b), and (c) with the terminal point labeled by P_a , P_b , and P_c respectively. Of these, only P_c will exhibit PIR. The exit set Ω_e is also illustrated.

in Ω_{PIR} . Therefore, no rebound burst will occur since neither conditions (5.50) nor (5.51) have been satisfied ($z_T > z_-(0)$ and $I_T > \bar{I}^-$). Path (b) on the other hand shows a path for which the threshold conditions (5.51) have been satisfied but the conditions (5.50) have not. Thus again, upon release no rebound burst will occur since the point $P_b = (z_T, I_T)_b$ does not lie in Ω_{PIR} . For the examples illustrated by the paths (a) and (b), the input was turned off before z_T crossed $z_-(0)$. Thus, when the input is turned off, a rapid transition to the lower branch $\mathbb{S}_{aL}(0)$ occurs instead of a transition to the periodic orbits Ω_p . Path (c) on the other hand, shows a path which has the point $P_c = (z_T, I_T)_c \in \Omega_{PIR}$. In this case, since

both conditions (5.50) and (5.51) have been satisfied, the solution will exhibit PIR upon the release of the input. Also notice that no path will ever reach Γ_- due to the location of the z -nullcline. This prevents any possible transitions to Ω_p before the stimulus is turned off.

In order to describe the conditions which guarantee PIR, it will be easier to refer to the exit set Ω_e defined as

$$\Omega_e = \{(z_-(0), I) : \bar{I}_{min} < I < \bar{I}^-\}, \quad (5.53)$$

instead of the region Ω_{PIR} . For example, if for some $t = \bar{T}_s$, $(z(\bar{T}_s), I(\bar{T}_s)) \in \Omega_e$, then for sufficiently large $T > \bar{T}_s$, a PIR burst is guaranteed to occur (to leading order). This set is also illustrated in Figure 33. Therefore, given the goal of finding conditions which guarantee PIR, what can be determined about the duration \bar{T}_s for an initial condition (z_s, I_s) in the (z, I) -plane? To answer this question, we give a general description of a trapping region in the (z, I) -plane and relate it to the different types of paths that are plausible (as are illustrated in Figure 33).

Trapping Regions

Now that Ω_e (see Figure 33) has been defined and threshold conditions have been established, we introduce a general theory for determining the conditions when such a duration \bar{T}_s exists. Then, as a consequence of finding conditions that guarantee a *Mixed* response, conditions for the *Off* response illustrated in Figure 25b) can also be established. To find these conditions recall that we assume that only inputs from the class \mathbb{C}_s will be considered.

First, because of the threshold conditions described in the previous section, recall that inputs from the class \mathbb{C}_s satisfy the conditions $\bar{I}_{lb} < I_{min} < I(\tau) < \bar{I}_m$ for all $\tau \in (t_0, t_0 + T)$. Furthermore, since $H_2(I) < 0$ for $I > I_{min}$ and $I_{min} < \bar{I}^-$, then there exist a $t^- \in (t_0, t_0 + T)$ such that $I_T < \bar{I}^-$ if T is sufficiently large. Thus, if T is sufficiently large, a path such as example (a) in Figure 33 will not occur and will not be investigated here.

In addition, it has been established for inputs from class \mathbb{C}_s that $\bar{I}_{lb} < I_{min}$. This will be used to guarantee that the flow of solutions in the I direction will not cross below the \bar{I}_{lb} -value and will in fact never cross the I_{min} -value. Now that these conditions have been discussed, define the trapping region Ω_{SSa} (illustrated in Figure 34) by

$$\Omega_{SSa} = \{(z, I) : z_-(0) < z < z_{max}, I_{min} < I < \bar{I}_m, I < \Theta(z)\}, \quad (5.54)$$

where z_{max} is defined as the maximum value that z can attain given an input in \mathbb{C}_s . This value corresponds to the homoclinic value when $I = \bar{I}_m = 1$, and thus can be calculated using Γ_{hc} to be

$$z_{max} = z_{hc}(0) + 1. \quad (5.55)$$

We will use the direction field of (SSa) in this region to guarantee that certain transitions must occur. Also, as defined, Ω_{SSa} contains the exit set Ω_e for Ω_{PIR} on one of its edges.

Notice that in the region Ω_{SSa} , $\frac{dz}{d\tau} < 0$ and $\frac{dI}{d\tau} < 0$. Thus, the region Ω_{SSa} has no fixed points and the only flow out of this region occurs at the exit set Ω_e since I cannot cross the lower bound value I_{min} (which may be as small as \bar{I}_{lb}). The region Ω_{SSa} , with

the appropriate direction field components, is illustrated in Figure 34. Also illustrated in Figure 34 is a “typical” trajectory $\tilde{\gamma}_X$ of (SSa) showing a transition from the initial starting point $\mathbf{X}_s = (z_s, I_s)$ to the terminating point $\mathbf{X}_T = (z_T, I_T)$. Also shown on this trajectory is the point $P^- = (z(t^-), I(t^-))$. For the illustrated trajectory, since \mathbf{X}_T is not in Ω_{PIR} , a PIR response would not occur.

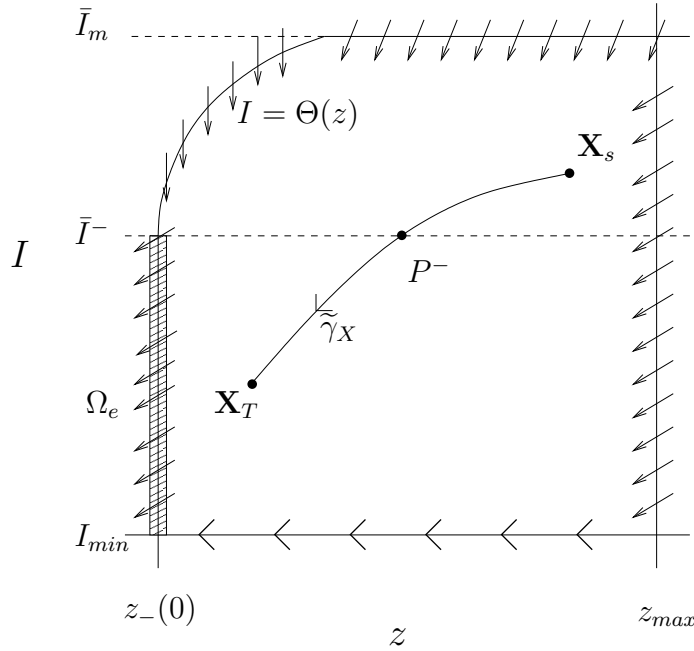


Figure 34. This figure shows a sketch of the trapping region Ω_{SSa} . Shown as the thin striped box is the exit set Ω_e . The small arrows show the direction field along each edge of Ω_{SSa} . Note that no trajectories can cross the I_{min} line at the bottom. Also shown in this figure is a trajectory $\tilde{\gamma}_X$ with starting and terminating points \mathbf{X}_s and \mathbf{X}_T , respectively. The point P^- is also shown where the trajectory crosses the threshold value \bar{I}^- .

Second, as for (AFSa), a trajectory of (SSa) that starts at \mathbf{X}_s and terminates at \mathbf{X}_T defines a map $\tilde{\Phi} : \mathbb{R}^2 \rightarrow \mathbb{R}^2$, such that $\mathbf{X}_T = \tilde{\Phi}(\mathbf{X}_s)$. Furthermore, define the flow function generated by (SSa) to be $\phi_{SSa}(\tau, \mathbf{X}_s) = \phi_{SSa}(\tau, (z_s, I_s))$. This function describes the flow

of (SSa) given the initial condition \mathbf{X}_s . With the descriptions of Ω_{SSa} and the exit set Ω_e , for any initial condition $\mathbf{X}_s \in \Omega_{SSa}$ an exit along Ω_e must occur for sufficiently large T . Therefore, there must exist a \bar{T}_s such that $\phi_{SSa}(\bar{T}_s, \mathbf{X}_s) \in \Omega_e$. With this in mind, the following Lemma has been established:

Lemma 4 *For all $\mathbf{X}_s \in \Omega_{SSa}$, there exists a \bar{T}_s such that*

$$\phi_{SSa}(\bar{T}_s, \mathbf{X}_s) \in \Omega_e. \quad (5.56)$$

This Lemma states that under the restrictions that define the class of inputs \mathbb{C}_s (with the appropriate threshold conditions) and the region Ω_{SSa} , there exists a time \bar{T}_s , such that if $T > \bar{T}_s$, then $\mathbf{X}_T \in \Omega_{PIR}$ and a PIR response is guaranteed to occur.

Having stated Lemma 4, a description of the silent phase of the *Mixed* response can now be given. First, to describe the *Mixed* response illustrated in Figure 25c), notice that the silent phase of the solution begins at time $t = (t_0 + \bar{T}_a)^+$, where \bar{T}_a is the active phase duration of the *Mixed* response. Recall that a rapid transition from the active phase to the silent phase occurs along Γ_{hc} . Thus, initial conditions for the silent phase, to leading order, are located on the Γ_{hc} curve. With this in mind, the curve Γ_{hc} becomes a boundary for a new region, Ω_{Ts} , inside of Ω_{SSa} . Illustrated in Figure 35a) is the region Ω_{Ts} , along with the Γ_{hc} curve (as a boundary). Notice that the Γ_{hc} curve intersects Ω_e at the value

$$I_\gamma = z_-(0) - \gamma_{hc}. \quad (5.57)$$

One special case to consider is when $I_{min} > I_\gamma$ (see Figure 35b)). In this case, knowing that a transition from the active phase to the silent phase must occur along Γ_{hc} , the initial

condition for the silent phase will still be located along the Γ_{hc} curve, and a transition to Ω_e will occur provided the duration is sufficiently large. Recall that when $H_2(I) = -\tilde{a}I + \tilde{b}$ is considered, $I_{min} = \frac{\tilde{b}}{\tilde{a}}$. For both the parameter pairs $(\tilde{a}, \tilde{b})_1$ and $(\tilde{a}, \tilde{b})_2$ used in Figure 31 for (AFSa), $I_{min} = -1.3$ (and $I_\gamma = -0.70613$), so that $I_{min} < I_\gamma$.

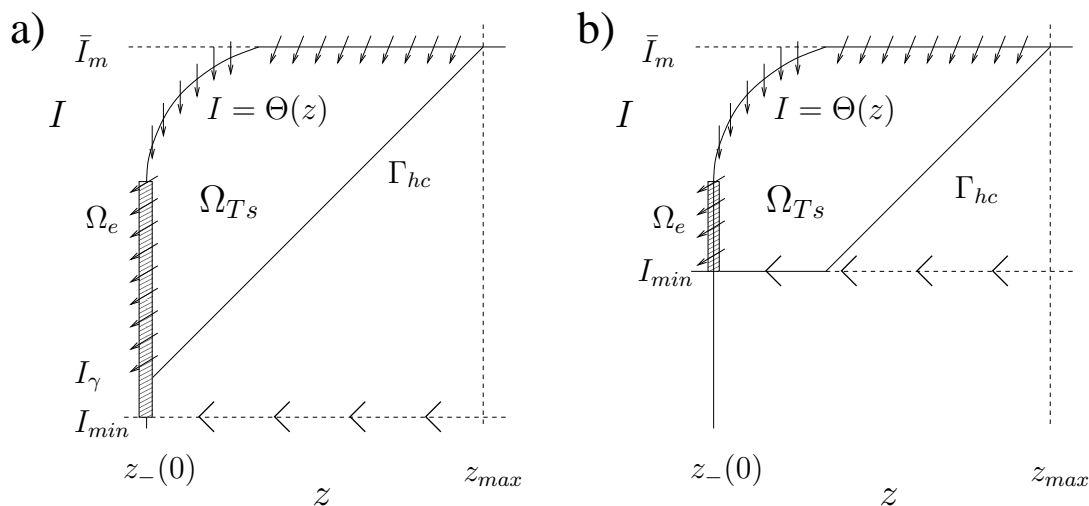


Figure 35. This figure shows a sketch of the trapping region Ω_{T_s} for two cases. In a), $I_{min} < I_\gamma$, and in b), $I_\gamma < I_{min}$. Shown in each figure as the thin striped box is the exit set Ω_e and the Γ_{hc} curve. Initial conditions for the silent phase portion of the *Mixed* response will lie on Γ_{hc} in both cases. For the parameter pairs $(\tilde{a}, \tilde{b})_1$ and $(\tilde{a}, \tilde{b})_2$ used in Figure 31, case a) applies.

The goal now is to compute the minimum duration \bar{T}_s needed to guarantee a PIR response given an initial condition along Γ_{hc} of the silent phase. Thus, \bar{T}_s is the time it takes for a silent phase transition from $\mathbf{X}_s = \mathbf{X}_{hc} \in \Gamma_{hc}$ to $\mathbf{X}_T \in \Omega_e$. First, note that Lemma 4 implies trajectories which enter Ω_{SSa} along $z = z_{max}$ must eventually exit along Ω_e . For the cases illustrated in Figure 35, this further implies trajectories starting on Γ_{hc} (with $I < \bar{I}_m$) must exit through Ω_e in finite time (again $H_2(I_{min}) = 0$ so trajectories cannot exit along the

line $I = I_{min}$). The difference between figures a) and b) is the location of I_{min} with respect to I_γ . Although trajectories are guaranteed to exit along Ω_e , can a lower bound value for the I component at the exit point be determined in these two cases? A lower bound value for $H_2(I) = -\tilde{a}I + \tilde{b}$ will depend on both (\tilde{a}, \tilde{b}) and the location of I_{min} . For the case illustrated in Figure 35b), $I_\gamma < I_{min}$, and so I_{min} is a lower bound on the I component at the exit point. In Figure 35a) on the other hand, $I_{min} < I_\gamma$ and a tighter lower bound may be found by imposing restrictions on the parameter pair (\tilde{a}, \tilde{b}) (even though I_{min} is still a lower bound in this case). In the following section, we determine conditions on (\tilde{a}, \tilde{b}) which will guarantee that I_γ is the lower bound value for the I component of the exit point.

Towards this end, define $\vec{N} = (-1, 1)$. This defines a normal vector on the Γ_{hc} curve pointing into the region Ω_{Ts} . To guarantee flow on Γ_{hc} is into Ω_{Ts} one needs

$$\vec{H} \cdot \vec{N} \Big|_{\Gamma_{hc}} > 0, \text{ for all } \mathbf{X}_{hc} \in \Gamma_{hc}, I \in (I_{min}, \bar{I}_m), \quad (5.58)$$

where

$$\vec{H} = \begin{bmatrix} H_1(z, I) \\ H_2(I) \end{bmatrix}.$$

To be precise, illustrated in Figure 36 is the direction field under such conditions. Notice that this condition guarantees that the only exit from Ω_{Ts} occurs at Ω_e . Were this not the case, a trajectory starting along Γ_{hc} could drop below Γ_{hc} and proceed outside the region Ω_{Ts} . With this in mind, what conditions exist on $H_2(I)$ so that condition (5.58) is satisfied?

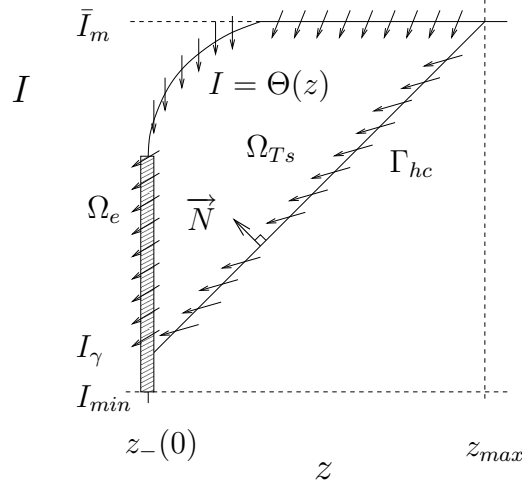


Figure 36. This figure shows a sketch of the trapping region Ω_{Ts} (for the case in Figure 35a)) with the normal vector and the appropriate direction field along Γ_{hc} .

To find such conditions, for $H_2(I) = -\tilde{a}I + \tilde{b}$ with $\tilde{a} > 0$, and $\tilde{b} < 0$, it follows that

$$\vec{H} \cdot \vec{N} = -H_1(z, I) + H_2(I) \quad (5.59)$$

$$= -h(u_{LB}(z - I)) + z - \tilde{a}I + \tilde{b} \quad (5.60)$$

Now evaluating (5.60) for values along Γ_{hc} gives:

$$\vec{H} \cdot \vec{N} \Big|_{\Gamma_{hc}} = -h(u_{LB}(\gamma_{hc})) + z_* - \tilde{a}(z_* - \gamma_{hc}) + \tilde{b}, \quad (5.61)$$

where z_* corresponds to each z -value in $(z_-(0), z_{max})$. The following Lemma gives the appropriate conditions on \tilde{a} and \tilde{b} which guarantee condition (5.58).

Lemma 5 *If $H_2(I) = -\tilde{a}I + \tilde{b}$, with $\tilde{a} > 0$ and $\tilde{b} < 0$, then equation (5.58) is satisfied if*

$$\tilde{b} > \tilde{a}(z_-(0) - \gamma_{hc}) + k - z_-(0) \text{ whenever } \tilde{a} < 1, \quad (5.62)$$

and

$$\tilde{b} > \tilde{a}(z_{max} - \gamma_{hc}) + k - z_{max} \text{ whenever } \tilde{a} > 1, \quad (5.63)$$

where $k = h(u_{LB}(\gamma_{hc}))$.

Proof. Define the right hand side of (5.61) as

$$C(z_*) = -k + z_* - \tilde{a}(z_* - \gamma_{hc}) + \tilde{b}. \quad (5.64)$$

In order to guarantee condition (5.58), the condition

$$C(z_*) > 0 \text{ for all } z_-(0) < z_* < z_{max}, \quad (5.65)$$

must be satisfied, or equivalently the condition

$$\tilde{b} > \tilde{a}(z_* - \gamma_{hc}) + k - z_* \quad (5.66)$$

must hold for all $z_* \in (z_-(0), z_{max})$.

First notice that for all $z_* \in (z_-(0), z_{max})$, $(z_-(0) - z_*) < 0$ and suppose that $\tilde{a} < 1$.

It then follows that

$$\tilde{a}(z_-(0) - z_*) > (z_-(0) - z_*), \quad (5.67)$$

and

$$\tilde{a}(z_-(0) - \gamma_{hc}) - \tilde{a}(z_* - \gamma_{hc}) > k - z_* - (k - z_-(0)). \quad (5.68)$$

Rewriting (5.68), we get

$$\tilde{a}(z_-(0) - \gamma_{hc}) + k - z_-(0) > \tilde{a}(z_* - \gamma_{hc}) + k - z_*. \quad (5.69)$$

Using inequality (5.69) with (5.66) gives the sufficient condition (5.62) on \tilde{b} in Lemma 5.

Second, notice that for all $z_* \in (z_-(0), z_{max})$, $(z_{max} - z_*) > 0$ and suppose that $\tilde{a} > 1$.

It then follows that

$$\tilde{a}(z_{max} - z_*) > (z_{max} - z_*), \quad (5.70)$$

and

$$\tilde{a}(z_{max} - \gamma_{hc}) - \tilde{a}(z_* - \gamma_{hc}) > k - z_* - (k - z_{max}). \quad (5.71)$$

Rewriting (5.71), the following inequality is given:

$$\tilde{a}(z_{max} - \gamma_{hc}) + k - z_{max} > \tilde{a}(z_* - \gamma_{hc}) + k - z_*. \quad (5.72)$$

Using inequality (5.72) with (5.66) gives the sufficient conditions (5.63) for \tilde{b} in Lemma 5.

This completes the proof. \square

The conditions described in Lemma 5 define a region $\Omega_{(\tilde{a}, \tilde{b})}$ in the (\tilde{a}, \tilde{b}) -plane which guarantees (5.58) is satisfied. Illustrated in Figure 37 is the region $\Omega_{(\tilde{a}, \tilde{b})}$. Notice that $(\tilde{a}, \tilde{b})_1 = (1, -1.3)$ is a pair in $\Omega_{(\tilde{a}, \tilde{b})}$. Recall that these values were used to describe the active phase durations for a *Mixed* response. Furthermore, although the active phase duration was not computed for the pair $(\tilde{a}, \tilde{b})_3 = (1, -1)$, it is also in $\Omega_{(\tilde{a}, \tilde{b})}$. Here, we will use the values $(\tilde{a}, \tilde{b})_1 = (1, -1.3)$ and $(\tilde{a}, \tilde{b})_2 = (5, 6.5)$ (one of which is in $\Omega_{(\tilde{a}, \tilde{b})}$ and one which is not) to determine the minimum duration \bar{T}_s in the silent phase for the special example $H_2(I) = -\tilde{a}I + \tilde{b}$, as described in \mathbb{C}_s .

Before this duration \bar{T}_s is calculated, illustrated in Figure 38 are examples of the trajectories of (SSa) when the parameter values $(\tilde{a}, \tilde{b})_1$ and $(\tilde{a}, \tilde{b})_2$ are used. As in (AFSa), the corresponding projections of (FULLa) have also been illustrated to show how well (SSa) approximates (FULLa) (they are almost indistinguishable). In this example $\epsilon = 0.0005$. Figure 38a) shows both the projection of (FULLa) and the solution of (SSa), z -null, and the Γ_{hc} curve, for $(\tilde{a}, \tilde{b})_1 = (1, -1.3)$. Notice that $\mathbf{X}_s \in \Gamma_{hc}$ and that for these parameters

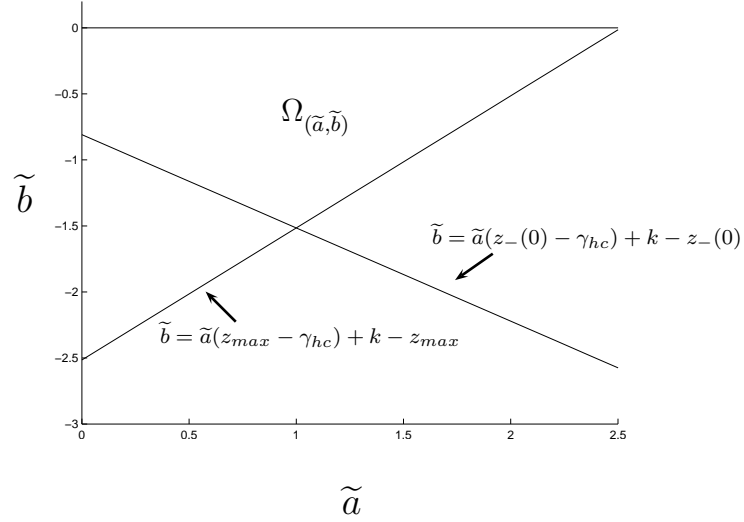


Figure 37. This figure shows the region $\Omega_{(\tilde{a}, \tilde{b})}$.

the conditions of Lemma 5 are satisfied. Figure 38b) shows the trajectory and the same curves for $(\tilde{a}, \tilde{b})_2 = (5, -6.5)$. In b), $(\tilde{a}, \tilde{b})_2 \notin \Omega_{(\tilde{a}, \tilde{b})}$, and the trajectory travels below Γ_{hc} . Figure 38 shows the silent phase portion of a *Mixed* response with the parameters $(\tilde{a}, \tilde{b})_1$ and $(\tilde{a}, \tilde{b})_2$. In both examples, $\mathbf{X}_T \in \Omega_{PIR}$ and a PIR response will occur. In this figure the initial condition was chosen to lie on \mathbb{S}_{a_L} defined in (5.46) at the appropriate location corresponding to $\mathbf{X}_s = \mathbf{X}_{hc} = \hat{\Phi}(\mathbf{X}_0)$.

Having established that (SSa) well approximates the silent phase duration, the minimum duration \bar{T}_s needed to guarantee PIR can now be calculated. Again, \bar{T}_s will depend on \tilde{a}, \tilde{b} , but more generally will depend on the location of \mathbf{X}_s . In a *Mixed* response, the location of \mathbf{X}_s depends on the active phase duration $\bar{T}_a(I_0, \tilde{a}, \tilde{b})$. Thus, for a *Mixed* response, $\bar{T}_s = \bar{T}_s(\tilde{a}, \tilde{b}, \mathbf{X}_s; I_0)$. Similar to finding the active phase duration, the silent phase duration \bar{T}_s is found by solving (5.47) and (5.48) to determine the time needed for the solution to

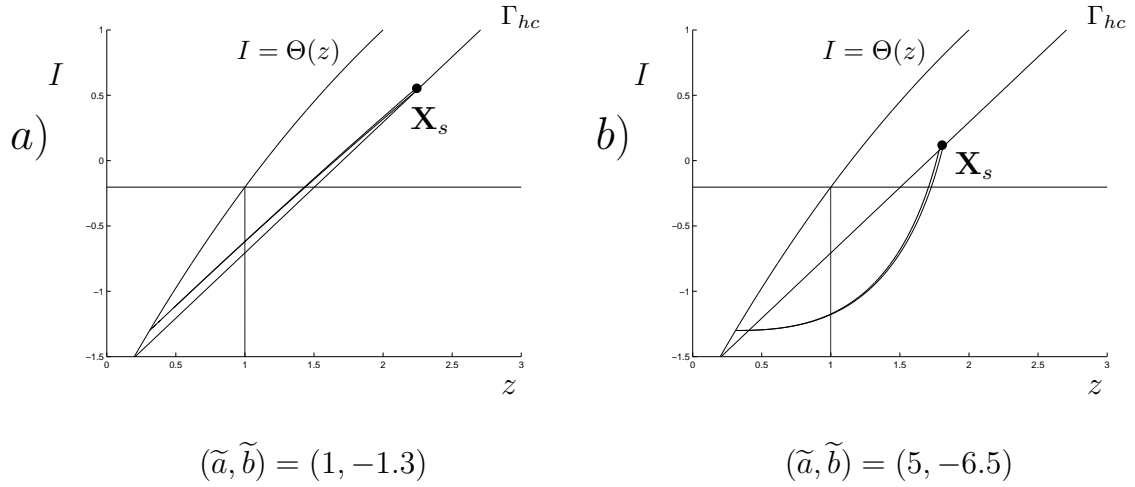


Figure 38. This figure shows the silent phase trajectory of (FULLa) projected on the (z, I) -plane and the trajectory generated by (SSa) (curve which starts at $\mathbf{X}_s \in \Gamma_{hc}$) when $H_2(I) = -\tilde{a}I + \tilde{b}$. In both figures $\epsilon = 0.0005$ was chosen to show how well (SSa) approximates the projection of (FULLa) in the silent phase in the limit $\epsilon \rightarrow 0^+$. Figure a) shows a trajectory when $(\tilde{a}, \tilde{b})_1 = (1, -1.3)$ is used. Notice that this trajectory satisfies the conditions of Lemma 5 and the trajectory does not cross Γ_{hc} . Figure b) shows the trajectory when $(\tilde{a}, \tilde{b})_2 = (5, -6.5)$ is used. When this pair is used, the conditions of Lemma 5 are not satisfied and the trajectory proceeds below Γ_{hc} . Also notice that in this case, a transition to Ω_{PIR} still occurs due to Lemma 4. In both cases the point $\mathbf{X}_T \in \Omega_{PIR}$ (not labeled in figure).

travel from \mathbf{X}_s to the exit set Ω_e . Even though (5.48) is decoupled and can be solved explicitly for $I(\tau)$ (as was shown in the previous section to attain (5.41)), an analytic formulation for the silent phase duration is difficult because of the form of u_{LB} in (5.47). Instead, we give a numerical computation of the time needed for solutions to travel from each starting point on Γ_{hc} to the exit set Ω_e (or to the z -value $z_-(0)$). This duration defines \bar{T}_s for each starting point $\mathbf{X}_s = \mathbf{X}_{hc}$ on Γ_{hc} .

Illustrated in Figure 39 are the durations \bar{T}_s needed to guarantee PIR as a function of

z_s , corresponding to the z -coordinate of the point $\mathbf{X}_s = (z_s, I_s)$. In this figure the durations \bar{T}_s are given for the two parameter pairs $(\tilde{a}, \tilde{b})_1 = (1, -1.3)$ and $(\tilde{a}, \tilde{b})_2 = (5, -6.5)$. Similar to the active phase duration, the smaller \tilde{a} is, the longer \bar{T}_s is. This will play an important role when describing *Mixed* responses. To obtain the durations \bar{T}_s , (SSa) was also solved using an explicit one step Runge-Kutta method similar to the one used for the active phase duration (*ode45* in Matlab). The lower branch u_{LB} -values were computed by solving equation (3.15) at each appropriate discretization point ($\gamma = z - I$) and choosing the appropriate root. Once the solution of (SSa) was computed, we obtained the time needed to travel from the initial value \mathbf{X}_s to the exit set Ω_e .

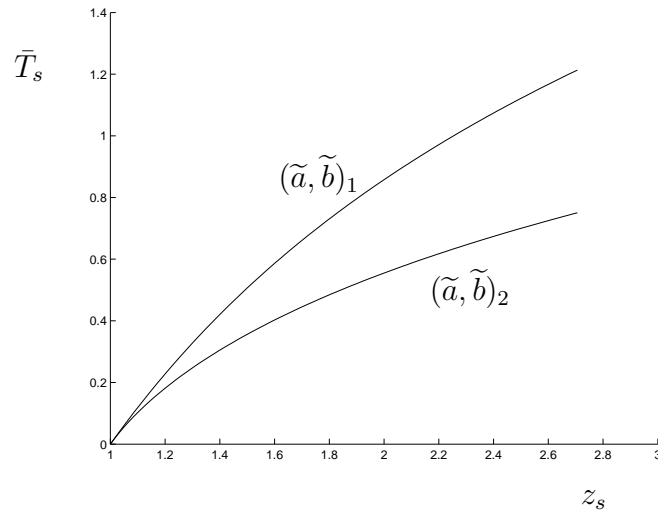


Figure 39. This figure shows the minimum duration \bar{T}_s needed in the silent phase to guarantee PIR as a function of the initial value $z_s \in \Gamma_{hc}$ for the two parameter pairs $(\tilde{a}, \tilde{b})_1$ and $(\tilde{a}, \tilde{b})_2$.

Now that these durations have been defined, we can also give a description of the *Off*

response. When using an input from the class \mathbb{C}_s to simulate an *Off* response, notice that it has the initial value $I_0 = 0$. The starting point for such an input does not lie on Γ_{hc} , but does lie in Ω_{SSa} . With that said, to describe the *Off* response illustrated in Figure 25b), the initial condition is $\mathbf{X}_s = (\bar{z}(0), 0)$. For such an initial condition, Lemma 4 guarantees that a PIR response can occur since the initial condition $\mathbf{X}_s = (\bar{z}(0), 0) \in \Omega_{SSa}$.

Illustrated in Figure 40 are two trajectories of (SSa) which correspond to two different *Off* responses. Notice that in both figures the initial condition lies on the $I = 0$ line at the equilibrium value $z = \bar{z}(0)$. Also shown in each figure are z -null, Γ_{hc} , $z_-(0) = 1$, and the point $(z(\bar{T}_s), I(\bar{T}_s))$ with the time \bar{T}_s . Illustrated in a) is the trajectory corresponding to $(\tilde{a}, \tilde{b})_1 = (1, -1.3)$. Illustrated in b) is the trajectory corresponding to $(\tilde{a}, \tilde{b})_2 = (5, -6.5)$. In each case, \bar{T}_s is computed by solving (5.47) and (5.48) (again, using an explicit Runge-Kutta formula) with the initial condition $\mathbf{X}_s = (\bar{z}(0), 0)$ and the appropriate constants.

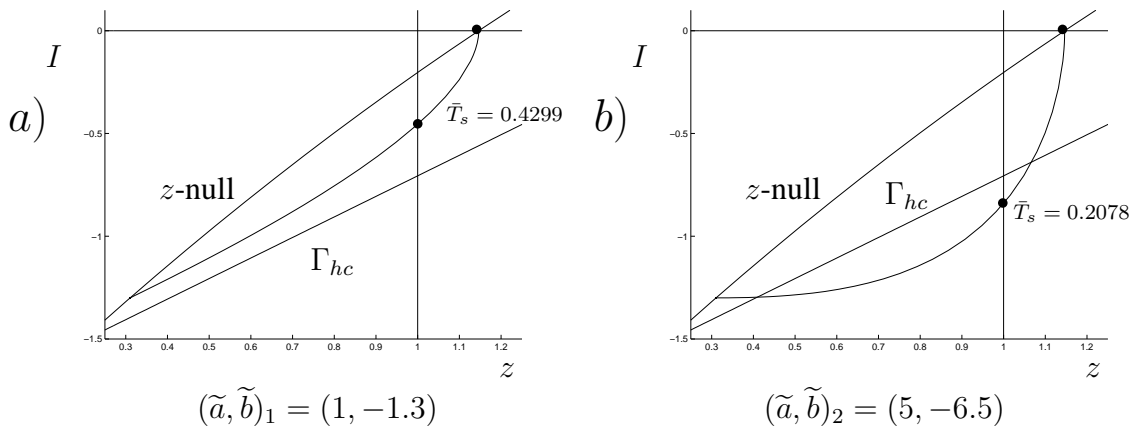
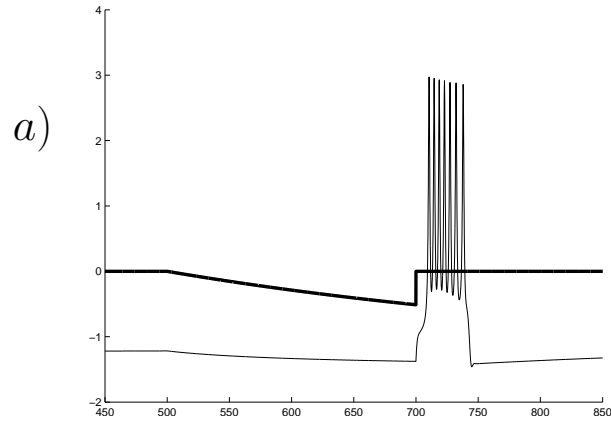


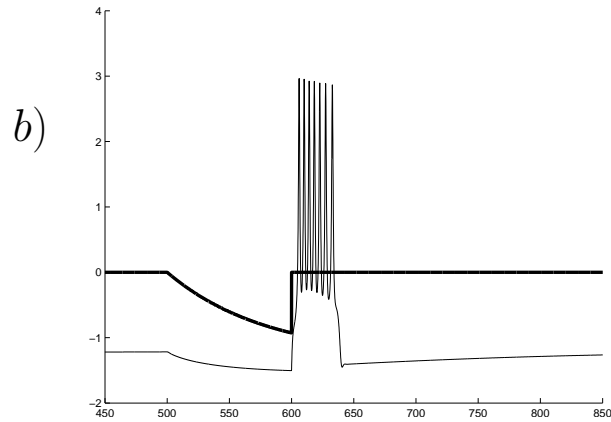
Figure 40. This figure shows the *Off* response silent phase trajectory of (SSa) for two different pairs (\tilde{a}, \tilde{b}) . In both figures the initial condition is $\mathbf{X}_s = (\bar{z}(0), 0)$. In a), $(\tilde{a}, \tilde{b})_1 = (1, -1.3)$ and in b) $(\tilde{a}, \tilde{b})_2 = (5, -6.5)$. Notice that in both figures, the duration \bar{T}_s has been given, and that a PIR response is guaranteed to occur since the point $\mathbf{X}_T \in \Omega_{PIR}$.

Figure 41 shows the responses when $I_0 = 0$, representing an *Off* response for the same (\tilde{a}, \tilde{b}) -pairs as in Figure 40. For figure a), $(\tilde{a}, \tilde{b})_1 = (1, -1.3)$, and the minimum duration which guarantees PIR was computed to be $T_0 = \frac{\bar{T}_s}{\epsilon} = 171.96$. The duration of the input for this figure is $T = 200$, and as a result PIR occurs. Similarly, for figure b), $(\tilde{a}, \tilde{b})_2 = (5, -6.5)$. The minimum duration which guarantees PIR for these parameters was computed to be $T_0 = \frac{\bar{T}_s}{\epsilon} = 83.12$. Notice that these durations were computed for a specific function $H_2(I)$ as defined by the class \mathbb{C}_s . The theory presented in this section gives a procedure for determining \bar{T}_s and can be extended for other functions $H_2(I)$.

In this section we used (SSa) to describe the solutions of (FULLa) in the silent phase. Since one of the goals is to find conditions that will guarantee a *Mixed* response, (SSa) was used to describe the conditions needed to guarantee PIR. With this goal in mind, we developed a description of the PIR region, in the (z, I) -plane. In this description, we found that certain threshold conditions must occur in order to elicit a PIR response, and these were used to define Ω_{PIR} . When the restrictions of the input class \mathbb{C}_s were incorporated, we defined the exit set Ω_e . We showed that for any initial condition in the region Ω_{SSa} , a transition to Ω_e can occur. Recall that when such a transition occurs, it defines a silent phase duration \bar{T}_s (minimum time needed to guarantee PIR). This duration was computed for two different parameter pairs (\tilde{a}, \tilde{b}) . To completely understand a *Mixed* response, both (AFSa) and (SSa) play an important role in the dynamics of (FULLa). As such, in the following section, (AFSa) and (SSa) are pieced together to describe the solution cycle for a *Mixed* response.



$$(\tilde{a}, \tilde{b})_1 = (1, -1.3) \text{ with } T = 200$$



$$(\tilde{a}, \tilde{b})_2 = (5, -6.5) \text{ with } T = 100$$

Figure 41. This figure shows two *Off* responses for two different (\tilde{a}, \tilde{b}) -pairs. In each, the initial condition was chosen to be $(z_0, I_0) = (\bar{z}(0), 0)$. In *a*), $(\tilde{a}, \tilde{b})_1 = (1, -1.3)$ are used with a duration T large enough to elicit PIR. Figure *b*) shows the same experiment for $(\tilde{a}, \tilde{b})_2 = (5, -6.5)$.

Map Composition

Now that both the active phase and the silent phase have been defined, we summarize a description of the solution cycle. Since the goal is to describe the conditions on the input which will guarantee a *Mixed* response, the solution of (FULLa) must travel through

both phases for a certain time to elicit each part, *On* and PIR. As such, both the active phase duration and the silent phase duration play an important role in the type of response (FULLa) will exhibit. Recall that (AFSa) and (SSa) provide the leading order asymptotic approximations of (FULLa) for the active phase duration and the silent phase duration, respectively. In this section, (AFSa) and (SSa) are pieced together and used to describe *Mixed* responses. To do this, we define the PIR map and illustrate how (AFSa) and (SSa) are used to describe the transitions of the initial condition \mathbf{X}_0 to the terminating point \mathbf{X}_T . In addition, we summarize the conditions which guarantee that \mathbf{X}_T reaches the target region Ω_{PIR} .

First, the PIR map is defined as $\Phi : \mathbb{R}^2 \rightarrow \mathbb{R}^2$, such that

$$\Phi(\mathbf{X}_0) = (\tilde{\Phi} \circ \hat{\Phi})(\mathbf{X}_0) \quad (5.73)$$

where $\mathbf{X}_0 = (z_0, I_0) \in \Gamma_0$. Notice that the PIR map is well defined as the composition of $\hat{\Phi}$ and $\tilde{\Phi}$ since $\mathbf{X}_s = \mathbf{X}_{hc} = \hat{\Phi}(\mathbf{X}_0)$ and $\mathbf{X}_T = \tilde{\Phi}(\mathbf{X}_s)$, and so $\mathbf{X}_T = \Phi(\mathbf{X}_0)$ if T is sufficiently large.

To generate the *On* part in a *Mixed* response, the solution must first travel through the active phase. The active phase portion of the solution is constructed from a trajectory $\hat{\gamma}_X$ of (AFSa) which starts at the initial condition \mathbf{X}_0 and terminates on Γ_{hc} at the point \mathbf{X}_{hc} . Recall that Lemma 3 guarantees that such a transition must occur in finite time (under certain threshold constraints). Once the trajectory reaches the homoclinic point \mathbf{X}_{hc} , (AFSa) is no longer valid since the solution has drifted into the monostable region. At this point, a transition to the silent phase occurs. As such, when piecing these subsystems together,

(SSa) now governs the leading order approximation of (FULLa) in the silent phase. The silent phase portion of the solution is constructed from a trajectory $\tilde{\gamma}_X$ of (SSa) which starts at the initial condition $\mathbf{X}_s = \mathbf{X}_{hc}$ and terminates at the point \mathbf{X}_T .

To describe a *Mixed* response, recall that \mathbf{X}_0 must satisfy certain threshold conditions to guarantee that an *On* part occurs. In addition, to guarantee PIR, or $\mathbf{X}_T \in \Omega_{PIR}$, the input must also satisfy certain threshold conditions and the duration must be of sufficient length. When these conditions are satisfied, the PIR map defines the transitions of solutions in the active phase and in the silent phase which result in a *Mixed* response.

To help understand and visualize the solutions of (FULLa), both the active phase and the silent phase are illustrated on two different (z, I) -planes with rapid transitions (of FS) connecting them. Illustrated in Figure 42 is a sketch of a PIR map. Recall the cell is assumed to be at rest labeled by \bar{X} . At $t = t_0$ a rapid transition to the point \mathbf{X}_0 on Γ_0 occurs (for the proper choice of thresholds). The PIR map then starts at \mathbf{X}_0 on Γ_0 and terminates at \mathbf{X}_T . Notice that at Γ_{hc} a rapid transition governed by (FS) from the active phase (shown at the top) to the silent phase (shown at the bottom) occurs. Also illustrated in the bottom plane of this figure are the z -null and the $z_-(0)$ curves. Shown in this figure is a projection of a solution where $\mathbf{X}_T \in \Omega_{PIR}$, and thus a PIR response is guaranteed to occur upon release. Figure 42 shows a silent phase trajectory which does not satisfy condition (5.58), and proceeds below Γ_{hc} . This type of trajectory is representative of the trajectory illustrated in Figure 38b).

The diagram presented in Figure 42 shows a transition through the active phase (*On*

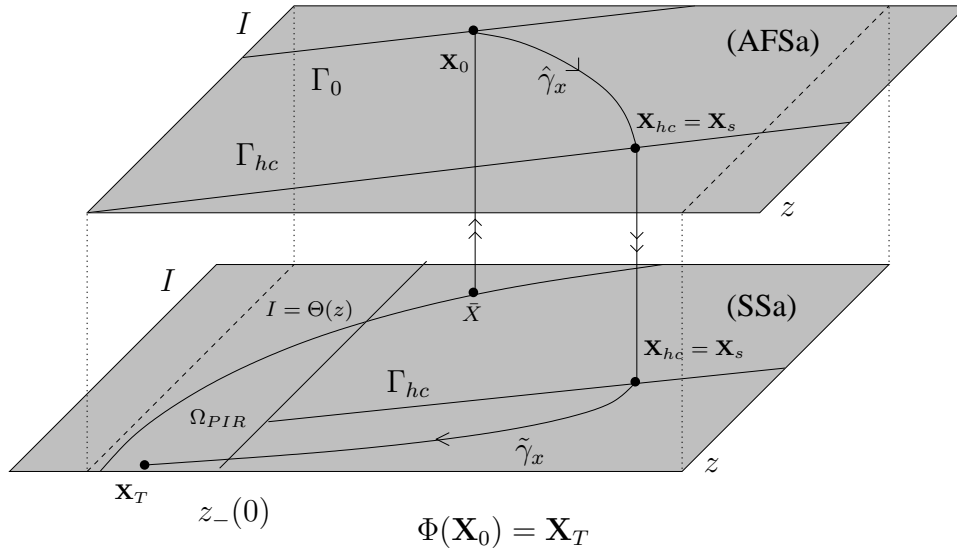


Figure 42. This figure shows the *On* burst cycle in the *Mixed* response along with the silent phase transition.

part of a *Mixed* response) and a transition in the silent phase along (SSa) terminating at \mathbf{X}_T . In order to have a complete picture of a *Mixed* response, Figure 43 shows the remaining PIR part of the solution. There, the transition from $\mathbf{X}_T = (z_T, I_T)$ to $(z_T, 0)$ is rapid, and since $\mathbf{X}_T \in \Omega_{PIR}$, a rapid transition to the active phase occurs (vertical). Once in the active phase, a transition from $(z_T, 0)$ to $(z_{hc}, 0)$ occurs (horizontal line in the (AFSa) portion of Figure 43). Once the trajectory reaches Γ_{hc} , a rapid transition to the silent phase occurs and then the solution travels back towards the equilibrium at \bar{X} . By combining Figures 42 and 43, a complete picture for a mixed response is illustrated.

The diagrams presented in Figures 42 and 43 are meant to give the essence of the role that both (AFSa) and (SSa) play in the solution cycle. Given an initial condition $\mathbf{X}_0 = (\bar{z}(0), I_0)$, the conditions that will guarantee $\Phi(\mathbf{X}_0) \in \Omega_{PIR}$ have been established

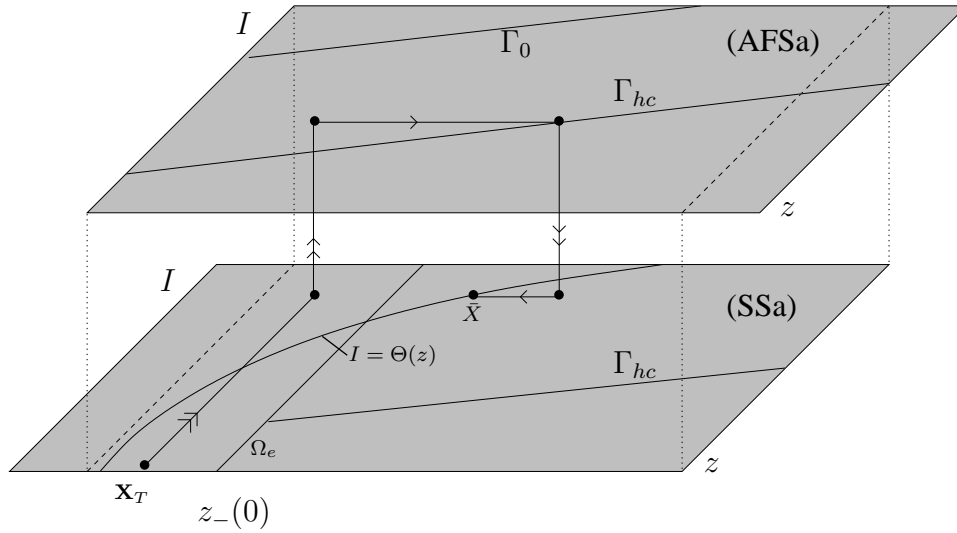


Figure 43. This figure shows the PIR burst cycle in the *Mixed* response.

for a certain class of inputs, namely those in \mathbb{C}_s . First recall that to guarantee an *On* part, $\bar{I}^+ < I_0$. This condition was established in Chapter 4. Whenever a transition to the active phase occurs, the active phase duration can be approximated using (AFSa). As such, given an input in the class \mathbb{C}_s the active phase duration can be computed for each $I_0 \in (\bar{I}^+, \bar{I}_m)$ using (AFSa). In this study, the active phase durations were computed for $H_2(I) = -\tilde{a}I + \tilde{b}$ with the two different pairs $(\tilde{a}, \tilde{b})_1$ and $(\tilde{a}, \tilde{b})_2$.

In addition to the active phase conditions, recall that certain threshold conditions on the input must also be satisfied to elicit PIR. For inputs in the class \mathbb{C}_s , these conditions were found to be $\bar{I}_{lb} < I_{min} < \bar{I}^-$ and that T be sufficiently large. A sufficiently large duration guarantees that upon release, $\mathbf{X}_T \in \Omega_{PIR}$. For $H_2(I) = -\tilde{a}I + \tilde{b}$, the silent phase duration \bar{T}_s was computed for each z -value on Γ_{hc} . For a *Mixed* response, the location of \mathbf{X}_s plays

an important role in determining \bar{T}_s . In describing the PIR map, \mathbf{X}_s can be determined from the active phase duration and (5.41). As a result, the silent phase duration can be calculated as well and the minimum duration needed to guarantee a *Mixed* response can be found.

In this section, different examples are given to show the role that \bar{T}_a and \bar{T}_s play on the solutions of (FULLa). These examples are also meant to provide verification for the durations computed in the previous sections. In each of these, the input's initial condition was chosen so that $\bar{I}_m > I_0 > \bar{I}^+$ (and is in fact $I_0 = 0.8$). Thus, it satisfies the conditions for an *On* part in a *Mixed* response. Illustrated in Figures 44a) and b) are two different responses for two different choices of parameters (\tilde{a}, \tilde{b}) . In both a) and b), notice that an *On* part occurs but no PIR response is attained since the duration of the input is not of sufficient length. To describe the duration needed for a *Mixed* response, both \bar{T}_a and \bar{T}_s are important. The minimum duration needed to guarantee a *Mixed* response is defined as:

$$T_m = \frac{1}{\epsilon} (\bar{T}_a(\mathbf{X}_0) + \bar{T}_s(\hat{\Phi}(\mathbf{X}_0))), \quad (5.74)$$

and depends on the initial condition \mathbf{X}_0 .

For the computations illustrated in the previous sections, recall that $H_2(I) = -\tilde{a}I + \tilde{b}$. As such, for $(\tilde{a}, \tilde{b})_1 = (1, -1.3)$, $T_m = 451.32$. For $(\tilde{a}, \tilde{b})_2 = (5, -6.5)$, $T_m = 227.6$. Both of these durations were calculated for $\epsilon = 0.0025$, but can be adjusted for each ϵ . For the examples illustrated in Figure 44, the durations for a) and b) are $T_1 = 300$ and $T_2 = 175$, respectively. Therefore, the conditions for a *Mixed* response are not satisfied and no PIR occurs.

Illustrated in Figure 45 are the same two examples (as in Figure 44) for longer stimulus

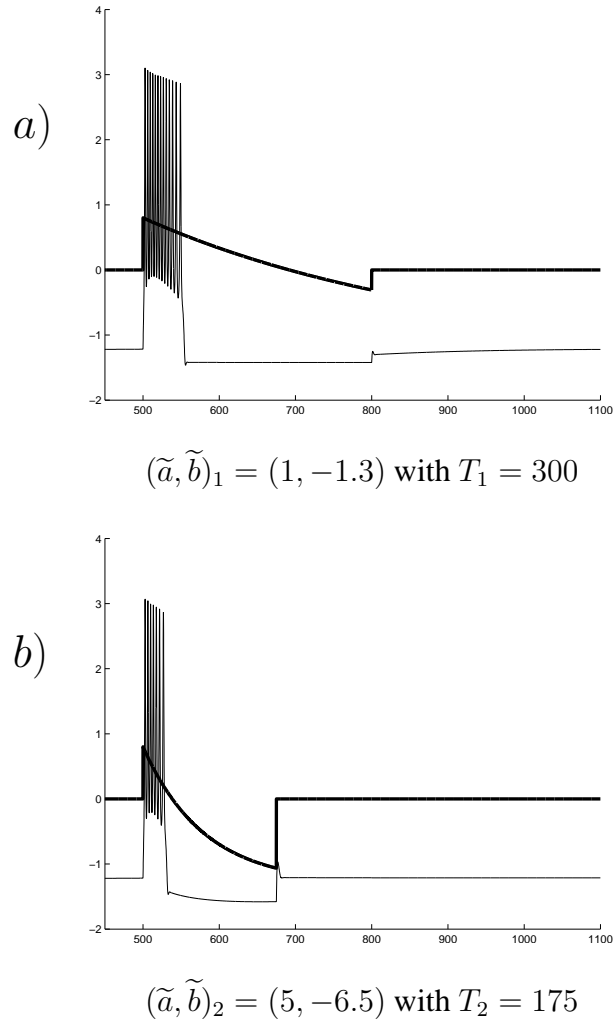


Figure 44. This figure shows the dependence of the response on the input duration. In *a*), $(\tilde{a}, \tilde{b})_1 = (1, -1.3)$ are used with an insufficient duration T to elicit PIR. Figure *b*) shows the same simulation for $(\tilde{a}, \tilde{b})_2 = (5, -6.5)$.

durations. Recall that to attain a *Mixed* response the minimum input durations were computed to be $T_m = 451.32$ for $(\tilde{a}, \tilde{b})_1 = (1, -1.3)$, and $T_m = 227.6$ for $(\tilde{a}, \tilde{b})_2 = (5, -6.5)$. Notice that PIR was attained in these examples since the durations, $T_1 = 475$ and $T_2 = 250$ were chosen to be sufficiently large.

In this section the active phase trajectories for $(\tilde{a}, \tilde{b})_1$ and $(\tilde{a}, \tilde{b})_2$ are shown along with

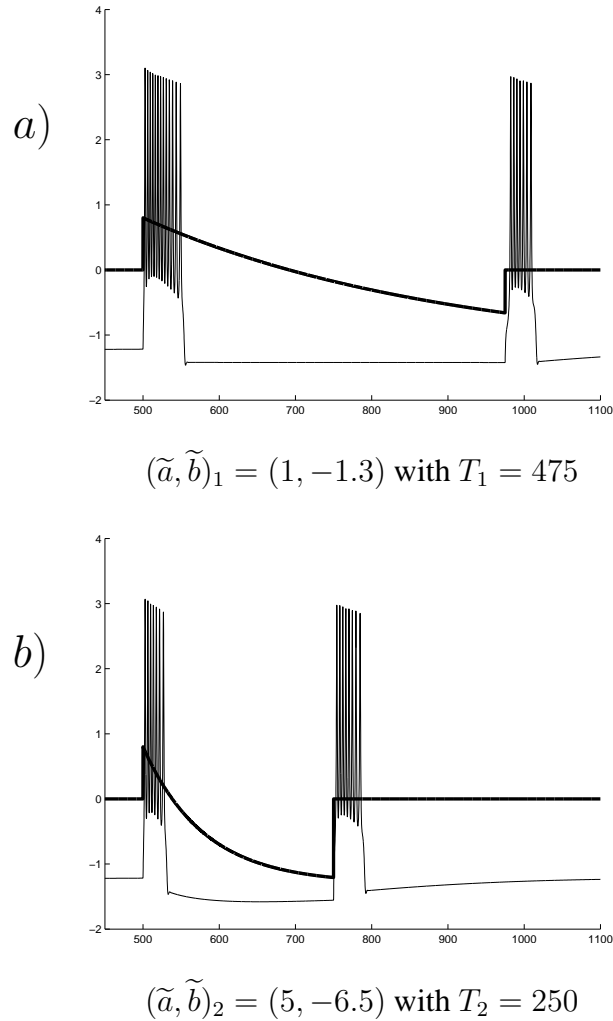


Figure 45. This figure shows *Mixed* responses for two different (\tilde{a}, \tilde{b}) -pairs. In *a*), $(\tilde{a}, \tilde{b})_1 = (1, -1.3)$ are used with a duration T large enough to elicit PIR. Figure *b*) shows the same experiment for $(\tilde{a}, \tilde{b})_2 = (5, -6.5)$.

the silent phase trajectories to illustrate a complete solution cycle in the (z, I) -plane. Illustrated in Figure 46 are the projections of (FULLa) and of (AFSa) composed with (SSa). In this figure $\epsilon = 0.0025$ (being larger than the previously used value, $\epsilon = 0.0005$, in Figure 38), and as a result, the difference between the projections of (FULLa) and the approximations given by the subsystems is more noticeable. Illustrated in Figure 46a) is the

complete solution cycle for the parameters $(\tilde{a}, \tilde{b})_1$ while Figure 46b) shows the cycle for $(\tilde{a}, \tilde{b})_2$. In both cases, the minimum durations needed to guarantee PIR have already been computed and are included in each figure.

To summarize, given $H_2(I) = -\tilde{a}I + \tilde{b}$, the conditions which guarantee a *Mixed* response are:

$$\{\bar{I}^+ < I_0 < \bar{I}_m, \bar{I}_{lb} < I_{min} < \bar{I}^-, T > T_m = \bar{T}_a + \bar{T}_s\}, \quad (5.75)$$

where, I_0 is given, $I_{min} = \frac{\tilde{b}}{\tilde{a}}$, \bar{T}_a is computed from (AFSa), and \bar{T}_s is computed from (SSa).

One interesting issue which has not been addressed but may be important in the description of solutions, is the decay rate of the input. With this in mind, for $H_2(I) = -\tilde{a}I + \tilde{b}$, it may be helpful to investigate the role that \tilde{a} plays on the durations. For example, the responses shown in Figure 44 and Figure 45 show that the durations \bar{T}_a and \bar{T}_s may depend on \tilde{a} . Notice that when \tilde{a} is smaller ($\tilde{a} = 1$), a longer active phase duration occurs and the *On* part of the response is longer than when a larger \tilde{a} value ($\tilde{a} = 5$) is used. As a consequence, the value of \tilde{a} will also affect the silent phase duration \bar{T}_s . The smaller \tilde{a} is, the longer the silent phase duration must be to guarantee PIR. Therefore, for inputs of the form $H_2(I) = -\tilde{a}I + \tilde{b}$ a longer active phase duration will also require a longer silent phase duration to attain PIR.

In Figure 47 we illustrate the active phase and the silent phase durations as a function of \tilde{a} . In the calculations of these durations, certain parameters were kept constant so that the role of \tilde{a} could be investigated. In Figure 47a), the durations were computed for $I_0 = 0.8$ and $I_{min} = 1$. Requiring I_{min} to be constant gives the appropriate \tilde{b} value (and as

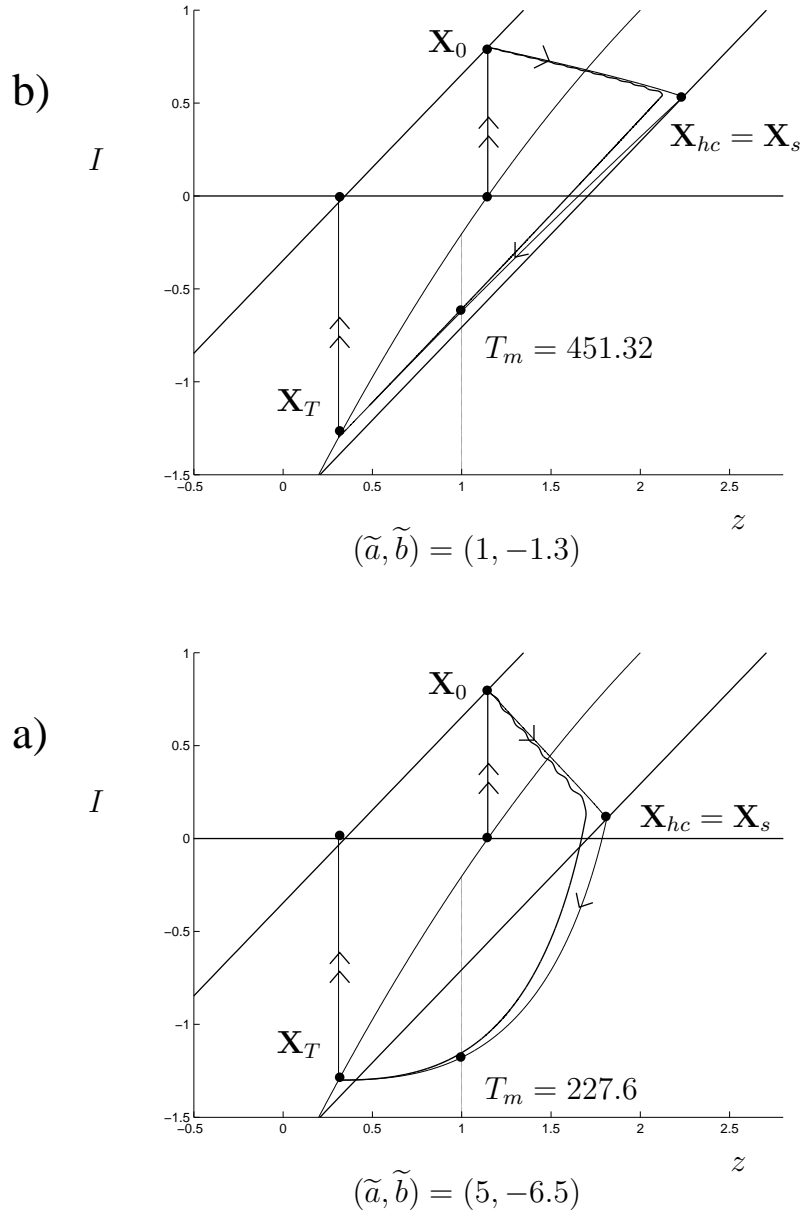


Figure 46. This figure shows the trajectory of (FULLa) projected on the (z, I) -plane and the trajectory generated by the subsystems (AFSa) and (SSa) when $H_2(I) = -\tilde{a}I + \tilde{b}$. In both figures $\epsilon = 0.0025$ and as a result a visual difference between the projected solution and the leading order solutions exists. Figure a) shows a trajectory when $(\tilde{a}, \tilde{b})_1 = (1, -1.3)$ is used. Notice that this trajectory satisfies the conditions of Lemma 5 and the trajectory does not cross Γ_{hc} . Figure b) shows the trajectory when $(\tilde{a}, \tilde{b})_2 = (5, -6.5)$ is used. When this pair is used, the conditions of Lemma 5 are not satisfied and the trajectory proceeds below Γ_{hc} . In both cases the duration $T > \bar{T}_m$ and the point $\mathbf{X}_T \in \Omega_{PIR}$, and as such a *Mixed* response is produced.

such \tilde{b} is not kept constant) for each \tilde{a} . Thus, under these restrictions $\bar{T}_a = \bar{T}_a(\tilde{a})$. In Figure 47b) a similar computation was conducted for the silent phase duration \bar{T}_s . In this case, the appropriate starting point $\mathbf{X}_s \in \Gamma_{hc}$ was computed from (AFSa) and used in (SSa). Under these restrictions, $\bar{T}_s = \bar{T}_s(\tilde{a})$. Notice that the minimum duration, T_m , needed to guarantee a *Mixed* response can be calculated from these two durations. Thus, given an initial condition $\mathbf{X}_0 = (\bar{z}(0), 0.8)$ and the ratio $\frac{\tilde{b}}{\tilde{a}} = 1$, $T_m = \frac{1}{\epsilon}(\bar{T}_a(\mathbf{X}_0) + \bar{T}_s(\hat{\Phi}(\mathbf{X}_0)))$. Notice that the smaller \tilde{a} is the longer the respective durations are. Although this implies that there is a fine balance between the choice of \tilde{a} and the subsystem durations, this may also depend on the value I_0 and \tilde{b} . Since all cases cannot be examined in this study, only the effects of \tilde{a} are investigated.

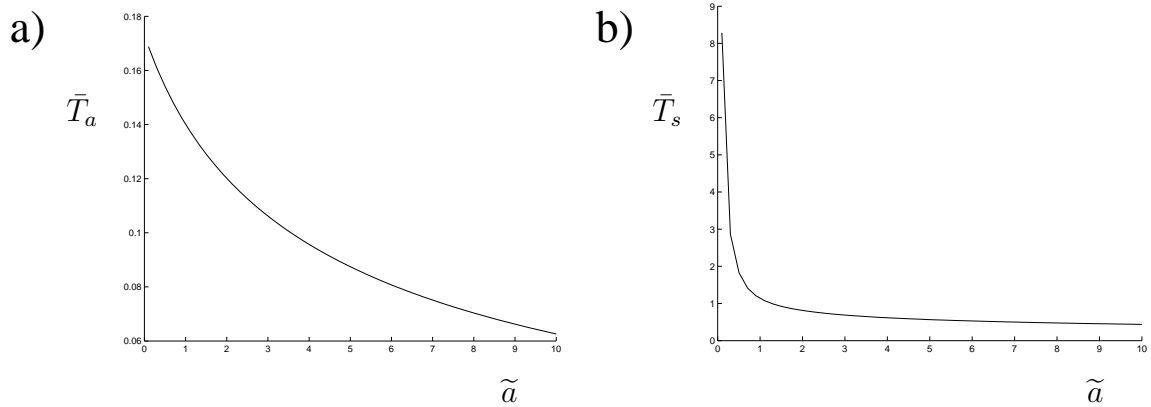


Figure 47. This figure shows the role of \tilde{a} on both the active phase and silent phase durations. In a), the active phase duration \bar{T}_a plotted as a function of \tilde{a} , for $\tilde{a} \in (0.1, 10)$. In b) the silent phase duration \bar{T}_s is plotted against \tilde{a} . Notice that when \tilde{a} is smaller, both the active phase and the silent phase durations are longer.

Presented in this chapter was a general theory for dealing with a non-autonomous bursting model. First, the class of monotone slowly decreasing inputs, \mathbb{C} , was defined and used to illustrate an *Off* and a *Mixed* response. The shapes of these inputs were motivated by the synaptic model solutions shown in Chapter 2. When inputs from the class \mathbb{C} were incorporated in the model, (FULL) was able to be augmented to an autonomous system. The augmented system was defined as (FULLa) and was the basis for all analyses in the chapter. Because of the definition of \mathbb{C} , (FULLa) has two-fast variables and two-slow variables. In this chapter, the goal was to use (AFSa) and (SSa) to find conditions to predict when (FULLa) can reproduce a *Mixed* response.

To describe the *On* part of a *Mixed* response, (AFSa) was analyzed for a sub-class of inputs \mathbb{C}_s . It was shown that for inputs of this type and the appropriate threshold conditions, an active phase transition must occur in finite time. Then, the active phase durations were computed for different parameter pairs (\tilde{a}, \tilde{b}) corresponding to the class of functions $H_2(I) = -\tilde{a}I + \tilde{b}$. Furthermore, (SSa) was defined and also analyzed for inputs in \mathbb{C}_s . In these analyses, the goal was to find conditions which would guarantee PIR. The PIR region Ω_{PIR} was defined and was used as a target region for the trajectories of (SSa). For the class of inputs in \mathbb{C}_s , we have shown that a silent phase transition to Ω_{PIR} is guaranteed to occur if the duration of the input is of sufficient length. This was achieved by defining the trapping region Ω_{SSa} and determining the silent phase duration \bar{T}_s . Again, this duration was computed for different parameter pairs (\tilde{a}, \tilde{b}) . Although $H_2(I) = -\tilde{a}I + \tilde{b}$ is only a sub-class of functions of \mathbb{C}_s examined, the procedures used to compute the active phase

and the silent phase durations can be extended to other functions.

Once the active phase and the silent phase durations were calculated, we defined T_m as the minimum duration needed to guarantee a *Mixed* response. This response was described as a composition of the solutions of (AFSa) and (SSa). To illustrate the solution cycle of (FULLa) for a *Mixed* response, the PIR map was defined and used to find the conditions needed for such a response. When the function $H_2(I) = -\tilde{a}I + \tilde{b}$ is used, it was also shown that the response of (FULLa) depends on \tilde{a} . Recall that \tilde{a} corresponds to the decay rate of the input. With the solution of the synaptic model illustrated in Table 1 in mind, different decay rates may play an important role in the responses of neurons. We found that the smaller \tilde{a} , the longer the active phase duration, and as a consequence, the silent phase duration must also be longer to guarantee PIR. In conclusion, the analyses conducted in this chapter describe the conditions needed for both the *Off* and the *Mixed* responses, and can be used to predict when such responses occur.

CHAPTER 6

CONCLUSIONS AND SUMMARY

Summary

The goal of this dissertation was to develop and analyze a non-autonomous bursting model which can reproduce each of the responses found in Figure 1. The model presented in this study, (FULL), is a system of nonlinear equations having one equation analogous to a current balance equation. First, we described and incorporated synaptic dynamics into a simple synapse model. Since the membrane potential of a neuron is directly affected by the synaptic input, we incorporated the solutions to the synaptic model into (FULL) as a time dependent input $I(t)$. Under such inputs, we showed that not only can (FULL) reproduce the *On*, *Off*, and *Mixed* responses observed experimentally in neurons, but we found the conditions which will guarantee these responses. We showed that these conditions depend on both the thresholds and the duration of the inputs.

Before we analyzed (FULL), the necessary subsystems needed to describe the solutions were defined. We defined and used the averaged-fast-subsystem to describe the flow of solutions along the active phase and to derive the active phase durations. Similarly, we defined and used the slow-subsystem to describe the flow of solutions along the silent phase and to derive the silent phase durations. For inputs which have rapid transitions, we found that the solutions of (FULL) depend on the basin of attraction of the periodic orbits

Ω_p . We generated a numerical description of the basin of attraction of Ω_p and showed that it caused dynamics which may not be realistic when modeling neurons. With these issues in mind, we chose initial conditions, input thresholds, and durations throughout the study so that only “realistic” solutions occurred.

When we considered a “constant current pulse”, the *On* and *Off* responses illustrated in Figures 1a)-b) were reproduced using (FULL). We used leading order analysis and averaging to determine regions in the (\bar{I}, T) parameter plane, including minimum and maximum threshold values, where the *On* and *Off* responses can occur. Even though in Figure 17 we demonstrated that different types of responses may be possible when using such an input, by choosing \bar{I} and T appropriately, the *On* and *Off* responses can be reproduced to leading order.

Furthermore, by including a monotone slowly decreasing input, conditions which guarantee an *Off* and a *Mixed* response were found for the special sub-class called “generic applicable” inputs. Under smooth slowly varying inputs, we augmented (FULL) to a system of autonomous equations. For the augmented system, we used the averaged-fast-subsystem to guarantee that a transition from an entry point in the active phase to the homoclinic point was possible. Although such transitions were guaranteed to occur for the general class of monotone slowly decreasing inputs, the examples presented resulted from generic applicable inputs. For these examples we established a procedure for computing the active phase durations.

In addition, we used the slow-subsystem to describe the slow flow along the silent

phase. Given an initial condition on the slow-subsystem manifold and in Ω_{SSa} , we showed that for generic applicable inputs, a transition in the silent phase to the target region called Ω_{PIR} can occur. Recall that reaching Ω_{PIR} guarantees a PIR response upon release of the input. This transition was shown to depend on certain amplitude thresholds and on the duration of the input. We also found the necessary conditions which guarantee such transitions in the silent phase for the class of generic applicable inputs (to leading order). Using both the averaged-fast-subsystem and the slow-subsystem, the minimum durations needed to guarantee a *Mixed* (or *Off*) response were computed (given a generic applicable input). We found that these durations depend on both certain threshold values and on the decay rate of the input.

Although the examples illustrated in Chapter 5 were for generic applicable inputs, the general approach and theory can be extended to the more general class of smooth slowly varying inputs. Also, it gives a starting point for dealing with models which have other non-autonomous inputs, and more specifically describes an approach for analyzing models given by (1.1)-(1.2).

Applications

The responses presented in this dissertation can be verified experimentally. Intracellular current injections and extracellular recordings with a visual stimulus are two examples of experiments used to record the responses of neurons. By varying the duration and the amplitude of the current used in intracellular current injections, one could verify the results

found in Figure 19. For example, Figure 4 of [14] shows the responses of an *in vitro* ferret visual neuron from different current injections. The response in part A) of this figure is very similar to the response illustrated in Figure 17d) where the duration of the stimulus was taken to be large enough to exhibit a bursting pattern (or chattering). For extracellular recordings similar to those found in [41] and [51] varying the duration and the intensity of the light stimulus may also help to verify the results found in Figure 19. In most experiments, the two simultaneous stimuli case has not been fully explored, but may be needed to explain more complex neural functions.

Regardless, individual cells must be able to reproduce the dynamics in Figure 1 for at least some kind of time dependent input. For example, Wang, Liets and Chalupa (2003) [80] showed that certain ganglion cells in ferrets exhibited all three types of responses due to both light stimulus and current injection. Experiments like these not only show that individual cells must reproduce these responses, but that the mechanism for such responses may in fact be given by the individual cell and not network properties. By including at least one slow somal and/or synaptic current, the results of the current study demonstrated that relatively simple time dependent inputs can reproduce all behaviors in Figure 1.

Recall that the time dependent input was considered to be the net synaptic input to the cell, but it may also be regarded as a light stimulus input to the receptive field of a visual neuron. By assuming $I(t)$ to be proportional to the light stimulus one can still verify the results of this dissertation. As previously discussed, by applying a stimulus in the appropriate part of a cell's receptive field and changing the duration of the stimulus, one can observe

whether or not the responses match the ones described in this study. Moreover, by changing the intensity of the stimulus, the threshold conditions might be confirmed. However, the assumption that the net synaptic input $I(t)$ and the light stimulus S be proportionally related presumes a 1-1 relationship between $S(x', t)$ over the receptive field and the synaptic input $i(x, t)$ over the synaptic field. It is possible that i and S may not even be functionally related. These issues additionally complicate modeling aspects but are nevertheless paramount for a more complete understanding of visual system responses.

Assuming $I(t)$ is the net synaptic input also helps to extend the results of this study to other sensory systems. For auditory neurons, the stimulus is sound intensity/frequency and relating a cell's receptive field with a particular response may not be as direct as in visual cells. On the other hand, [49] showed that the receptive field of sensory neurons in the weakly electric fish have a parallel structure to mammalian visual LGN cells with center surround receptive fields. For these types of neurons the connectivity properties may include feedback from higher processing stages and the exact correlation between electric field stimulus and synaptic input can be difficult to measure. Thus, by considering $I(t)$ to be the net synaptic input due to a stimulus, one does not have to substantiate a relationship between stimulus and synaptic input.

Numerical Results

Now that the model has been developed, discussed, and analyzed for both constant current pulses and monotone slowly decreasing inputs, various numerical examples of the

solutions of (FULL) for other inputs are presented. These simulations include various non-autonomous inputs such as those illustrated in Table 1. Also included in this section, the numerical solutions of (FULL) when different sinusoidal inputs are used. These types of inputs were applied experimentally in [21, 24, 49, 73], for example.

First, illustrated in Figure 48 are the numerical solutions of (FULL) when

$$I(\tau) = (H(\tau - t_0) - H(\tau - t_0 - T))\left(\frac{\tilde{b}}{\tilde{a}}(1 - e^{-\tilde{a}(\tau-t_0)}) + I_0 e^{-\tilde{a}(\tau-t_0)}\right), \quad (6.1)$$

with $I_0 = 0$, for two different (\tilde{a}, \tilde{b}) -pairs and $T = 350$. Illustrated in Figure 48a), $(\tilde{a}, \tilde{b}) = (5, 4)$ while in b) $(\tilde{a}, \tilde{b}) = (3, 4)$. This type of input corresponds to slowly activating excitatory synaptic input (with a fast inactivation). One thing to note here is that the *On* response has a small delay due to a slow excitatory synaptic input similar to the input illustrated in row 3 of Table 1. Illustrated in a), only a single burst occurs due to the fact that for this choice of parameters $\frac{\tilde{b}}{\tilde{a}} = \frac{4}{5} < \bar{I}_m$. In b) on the other hand, $\frac{\tilde{b}}{\tilde{a}} = \frac{4}{3} > \bar{I}_m$ and multiple bursts can occur (as was illustrated in Figure 19). Both of these patterns of responses, including the delays have been illustrated in [14] and [49], for example.

When synaptic plasticity is incorporated, (FULL) can reproduce both an *On* and an *Off* response and these are illustrated in Figure 49. Illustrated in this figure are the solutions of (FULL) when

$$I(t) = (H(\tau - t_0) - H(\tau - t_0 - T))(I_1(e^{-\tilde{c}(\tau-t_0)} - e^{-\tilde{d}(\tau-t_0)})) \quad (6.2)$$

is used with $\tilde{c} = 4$, $\tilde{d} = 8$, and $T = 250$ for two different values of I_1 . Illustrated in Figure 49a), $I_1 = 4$, and an *On* response occurs. In Figure 49b), $I_1 = -4$, and an *Off*

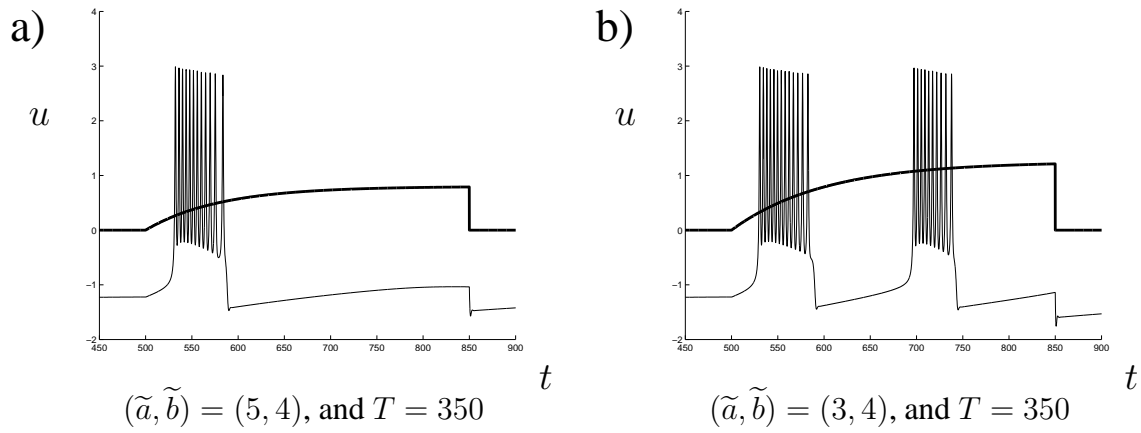


Figure 48. This figure shows two different delayed *On* responses for synaptic inputs with slowly activating excitatory inputs. In a) a single burst is shown while b) shows multiple bursts.

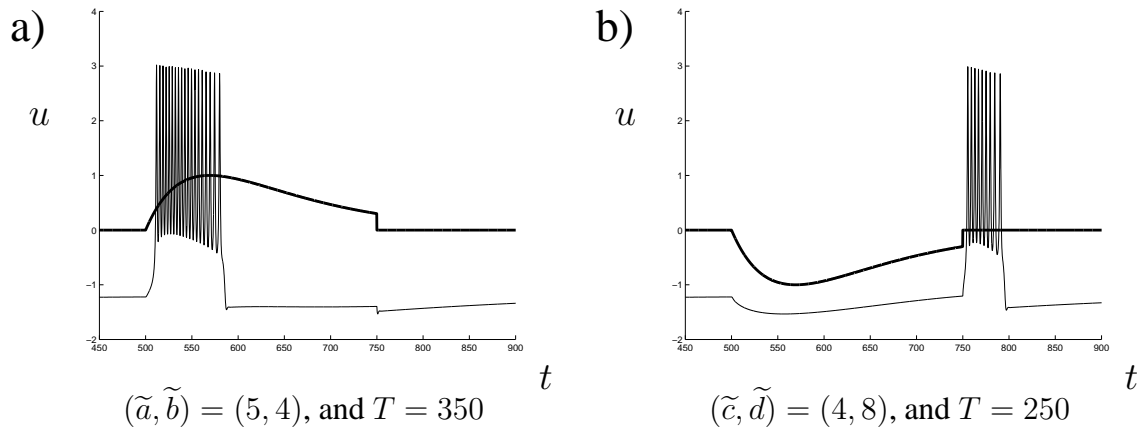


Figure 49. This figure shows the *Off* response silent phase trajectory of (SSa) for two different pairs (\tilde{a}, \tilde{b}) . In both figures the initial condition is $\mathbf{X}_s = (\bar{z}(0), 0)$. In a), $(\tilde{a}, \tilde{b})_1 = (1, -1.3)$ and in b) $(\tilde{a}, \tilde{b})_2 = (5, -6.5)$.

response occurs. These types of inputs correspond to synaptic inputs which incorporate the effects of depression and are similar to those illustrated in row 8 of Table 1. This type of synaptic plasticity has been shown in [50] and [79].

As previously mentioned, in many experiments a sinusoidal stimulus input has been

used to stimulate certain cells. For example, in visual system neurons, a sine wave grating of various spatial drifting frequencies or contrast reversal stimuli has been used. Experimental data has been recorded in [21, 49, 73] for these types of stimuli in visual system cells. In auditory neurons, similar sinusoidal inputs have also been used to study the responses of neurons. For example, in [24], auditory neurons' responses were recorded as a consequence of sinusoidal frequency tone modulations. In general, the experiments mentioned above have been used to detail how the input/output properties of certain cells are affected by the spatial and temporal frequency of the stimulus.

To simulate (FULL) with a sinusoidal input, consider

$$I(t) = I_1 \sin\left(\frac{\pi}{N}(t - t_0)\right) \quad (6.3)$$

with different amplitudes I_1 and of various periods represented by the value N . In the following examples, the duration of the input was considered large enough for the steady-state of (FULL) to be established. Illustrated in Figure 50a) is the solution of (FULL) when $I_1 = 0.5$, and $N = 100$. Notice that for this type of input, the majority of the burst patterns occur after the peaks of the sinusoidal input. This type of response is similar to those illustrated in Figure 9(f) of [24] and in Figure 2(a) (OFF relay cell) of [49]. Illustrated in Figure 50b) is the solution of (FULL) when $I_1 = 1$, and $N = 100$. In this example the bursts occur just before and at the peaks of the input. This type of response matches those shown in Figure 1(c) of [21], Figure 11 of [81], and in Figure 2(a) (ON relay cell) of [49].

It is interesting to note the responses of (FULL) illustrated in Figure 51. There, three different responses are shown for three similar sinusoidal inputs. In a), $I_1 = 0.23$ and

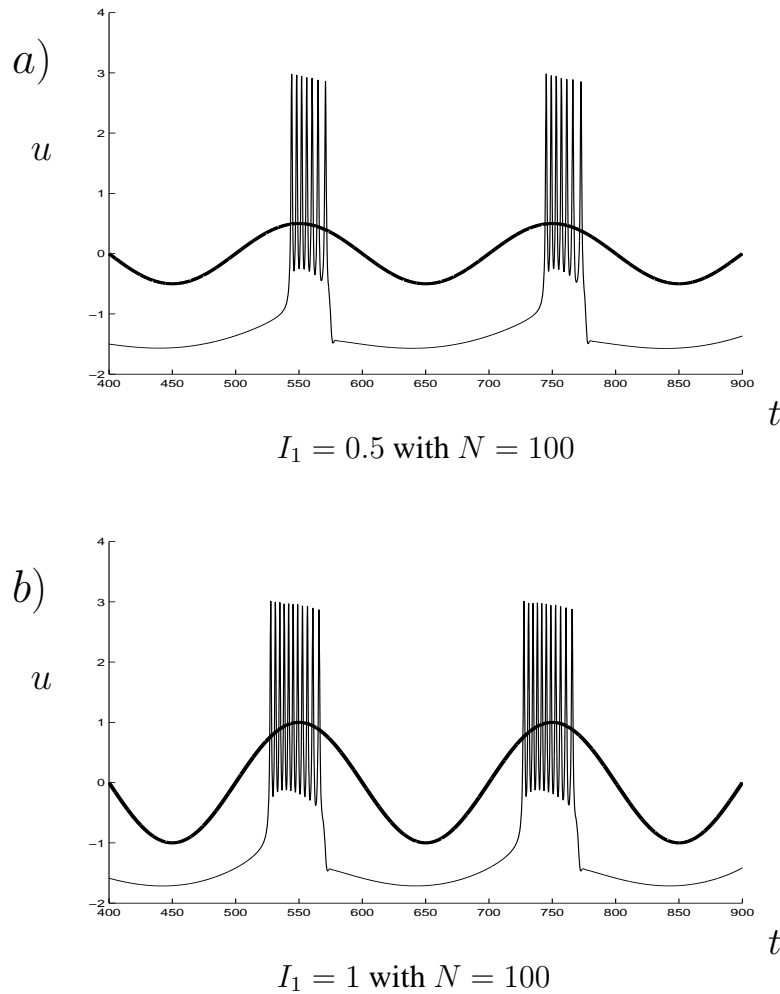


Figure 50. This figure shows the response of (FULL) when a sinusoidal input is used. In a) the amplitude $I_1 = 0.5$ and in b) $I_1 = 1$. Notice that the location of the burst cycles occur at slightly different locations relating to the peaks of the inputs.

$N = 85$; in b) $I_1 = 0.26$ and $N = 85$; and in c) $I_1 = 0.29$ and $N = 85$. For each of these I_1 -values, the bursts occur at different locations with respect to the input. First, the response illustrated in Figure 51a) is very similar to the one illustrated in Figure 2(A) in [73]. There, whole cell recordings of a single relay neuron during a sinusoidal current injection over a range of modulation amplitudes is shown. It is interesting to note that

(FULL) can capture the qualitative behavior illustrated at the top of Figure 2(A) while the Integrate-and-Fire-or-Burst model presented in the same paper does not (for low amplitude modulations).

In general, for experimental results not represented by those in this study, it may be possible that a different (FS) could reproduce the results. In this dissertation (FS) was chosen so that (FULL) exhibits square wave bursting patterns. These patterns have been observed in many experiments. For example, results found in [14] and [81] showed similar bursting patterns (chattering). However, by applying results from [59], fast parameters can be chosen to alter the (FS) bifurcation diagram in such a way that (FULL) can reproduce other experimental results found in [14], [31], [76], and [81]. In Figure 52, fast parameters were chosen to match beating (fast spiking) patterns. Such patterns more closely resemble those found in Figure 1 in [31] for instance.

In contrast, in Figure 53 fast parameters were chosen to match the “Nearly Parabolic” fast subsystem discussed in [59]. These patterns well reproduce the experimental results presented in Figure 3a) of [14] and Figure 1 in [76]. Thus, experiments like those described above might be used to determine an appropriate (FS) for the specific cells at various levels within the visual system (i.e., retinal ganglion, LGN, V1, V3, etc.) or other sensory systems.

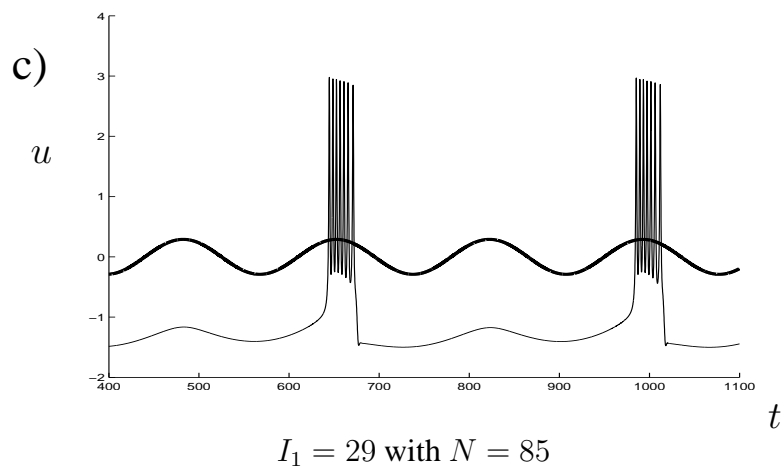
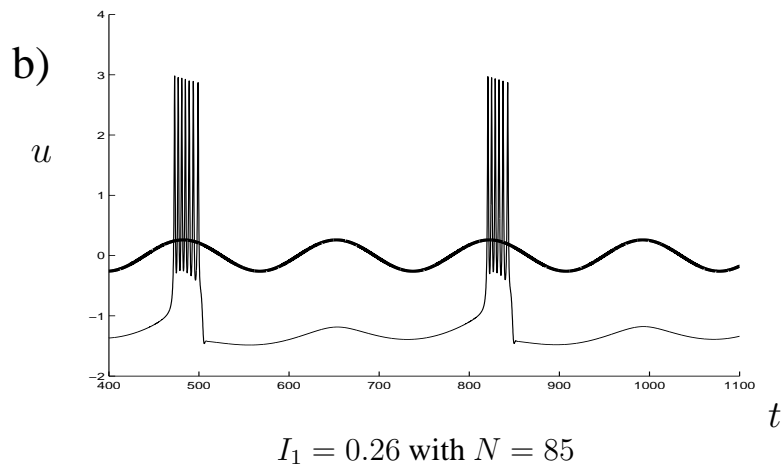
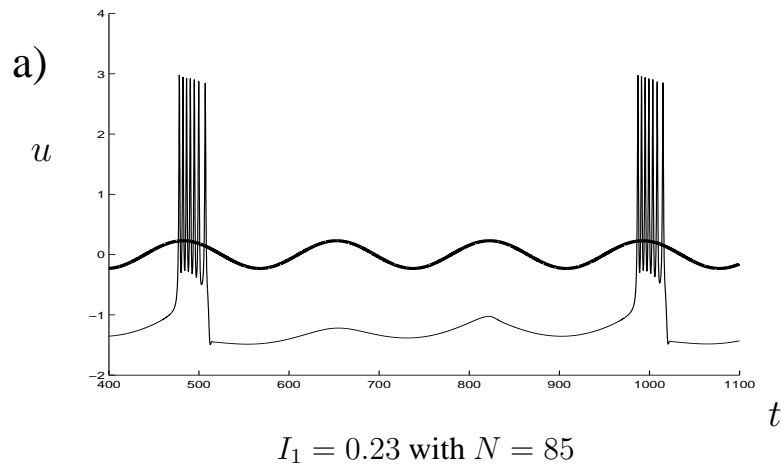


Figure 51. This figure shows three different bursting patterns when three different amplitudes are used.

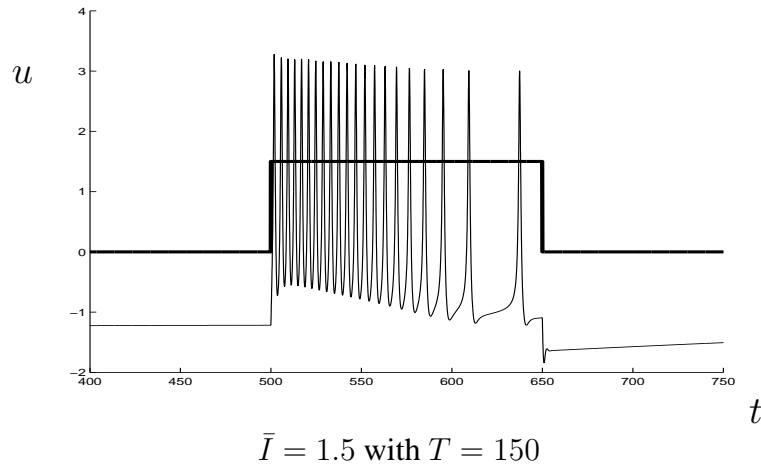


Figure 52. This figure shows the response of (FULL) when a constant current pulse is used but (FS) exhibits a “fast spiking” or beating behavior (instead of bursting).

Future Work

Although many issues in analyzing a non-autonomous bursting model have been resolved in this dissertation, a multitude of open questions remain. First, the class of inputs given by \mathbb{C} can be extended to include more physiologically relevant inputs. For example, one might use inputs generated by a synaptic model which were not discussed in this study, but are included in Table 1. Due to the physiological nature of the inputs, the more general class of inputs must be bounded. These ideas can then lead us to a more general classification of inputs and further analyses of (FULL).

More specifically, the net synaptic input to the cell will have many different shapes and forms, and being able to analyze (FULL) under such various inputs may foster new mathematical methods and could answer many modeling questions. Extending the analyses of Chapter 5 to include these different types of inputs may help to determine maximum

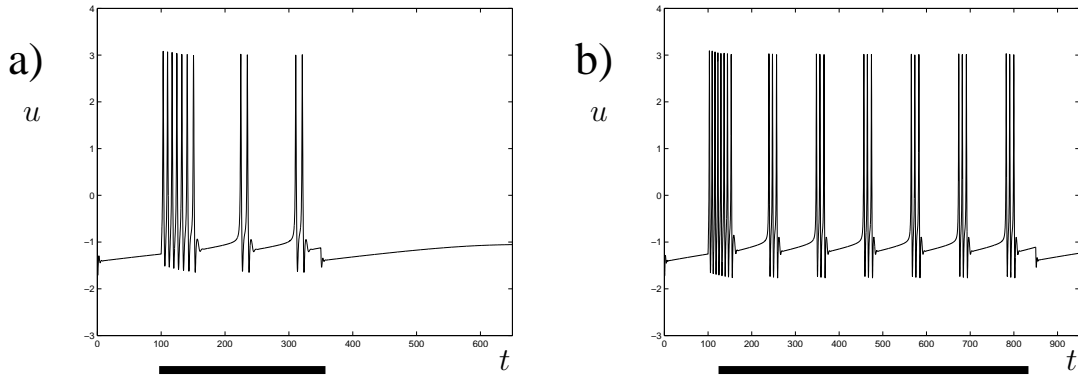


Figure 53. This figure shows the response of (FULL) when the parameters of (FS) are chosen to exhibit a “Nearly Parabolic” behavior [59]. In each figure the black line represents the time duration of the input. In a), the fast parameter set $\lambda_f = (0.25, 1.1, 1)$ was used with a stimulus intensity $\bar{I} = 0.5$ and a duration $T = 250$. These parameters were chosen to match experimental results found in [14]. In b) the fast parameter set $\lambda_f = (0.25, 1.15, 1)$ was used with a stimulus intensity $\bar{I} = 0.5$ and a duration $T = 750$. These parameters were chosen to match experimental results found in [76]. The difference between these responses and those in Figure 17 is that these patterns have action potential minima in the bursting patterns which are below their silent phase values. The patterns in Figure 17 have action potential minima which are elevated above the silent phase. Notice that these differences may occur not only in different cells in different layers of the visual system but in different animals (i.e. ferret vs. cat).

and minimum threshold values that such an input must have to generate different neuronal responses. One example is to extend Lemma 4 to a more general class of inputs. Recall that Lemma 4 stated that a transition from \mathbf{X}_0 to $\mathbf{X}_T \in \Omega_{PIR}$ in the silent phase was guaranteed to occur (for a sufficiently large duration) only for inputs in the class \mathbb{C}_s .

In the sinusoidal input case, the objective of describing the necessary conditions needed to guarantee a *Mixed* response no longer applies. In this case, perhaps a more appropriate approach would be to piece together the analysis of the decay portion of the input with an analysis of growth of the input to predict when rapid transitions to the active phase occur.

This may involve an approach similar to the one explored in [32] where the fixed points of a return map correspond to bursting solutions.

Even though extending the class of inputs may be appropriate, for many types of inputs, an augmentation to a higher dimensional autonomous system may not be plausible. Notice that the augmentation of (FULL) was a valid transformation for smooth monotone slowly decreasing inputs, but this may not always be the case. If the input $I(t)$ is the solution to an initial value problem, then an augmentation can occur. Unfortunately, this may not often be the case and dealing with such an input may require another mathematical approach. A question for future work is then “under what types of inputs can (FULL) be augmented to a higher dimensional system?”

Another project that could easily parallel the one in this study is to analyze (FULL) when different fast subsystem parameters are used. For example, in the previous section it was shown that (FULL) can reproduce other forms (other than bursting) of neuronal responses. By changing the fast parameters, (FS) can be altered easily and a similar analytical approach can be followed. This could lead to different synaptic input conditions which can be used to guarantee that certain responses occur.

Lastly, in Chapter 3 a numerical description of the basin of attraction of (FS) was given. This description could be extended analytically. For example, using the Liénard form of (FULL) and incorporating phase plane analysis, the existence of regions in the (u, v) -plane that are in the basin of attraction of Ω_p could be proved. This would then confirm the numerical results that illustrate improbable responses when modeling neurons, and would

help to explain the complete dynamics of (FULL).

REFERENCES CITED

- [1] L. Abbott and C. van Vreeswijk. Asynchronous states in networks of pulse-coupled oscillators. *Phys. Rev. E*, 48(2):1483–1490, 1993.
- [2] J. Alexander, E. Doedel, and H. Othmer. On the resonance structure in a forced excitable system. *SIAM J. Appl. Math.*, 50(5):1373–1418, 1990.
- [3] S. Amari. A mathematical theory of nerve nets. *Ad. biophys.*, 6:75–120, 1974.
- [4] E. Av-Ron, H. Parnas, and L. Segel. A basic biophysical model for bursting neurons. *Biol. Cybern.*, 69:87–95, 1993.
- [5] J. Bekkers, G. Richerson, and C. Stevens. Origin of variability in quantal size in cultured hippocampal neurons and hippocampal slices. *Proc. Natn. Acad. Sci. U.S.A.*, 87:5359–5362, 1990.
- [6] J. Bekkers and C. Stevens. Nmda and non-nmda receptors are co-localized at individual excitatory synapses in cultured rat hippocampus. *Nature*, 341:230–233, 1989.
- [7] G. Benison, J. Keizer, L. Chalupa, and D. Robinson. Modeling temporal behavior of postnatal cat retinal ganglion cells. *J. Theor. Biol.*, 210:187–199, 2001.
- [8] R. Bertram and A. Sherman. Population dynamics of synaptic release sites. *SIAM J. Appl. Math.*, 58(1):142–169, 1998.
- [9] R. Bertram, A. Sherman, and E. Stanley. Single-domain/bound calcium, hypothesis of transmitter release and facilitation. *J. Neurophysiol.*, 75:1919–1931, 1996.
- [10] R. Bertram, P. Smolen, A. Sherman, D. Mears, I. Atwater, and F. Martin. A role for calcium release-activated current (CRAC) in cholinergic modulation of electrical activity in pancreatic β -cells. *Biophys. J.*, 68:2323–2332, 1995.
- [11] A. Borisyuk, M. Semple, and J. Rinzel. Adaptation and inhibition underlie responses to time-varying interaural phase cues in a model of inferior colliculus neurons. *J. Neurophysiol.*, 88:2134–2146, 2002.

- [12] P. Bressloff and J. Cowan. Spontaneous pattern formation in primary visual cortex. In *Nonlinear dynamics: Where do we go from here?*, S. J. Hogan, A. Champneys, and B. Krauskopf, editors. Institute of Physics. In press, Bristol, 2002.
- [13] R. Brette and W. Gerstner. Adaptive exponential integrate-and-fire model as an effective description of neuronal activity. *J. Neurophysiol.*, 94:3637–3642, 2005.
- [14] J. Brumberg, L. Nowak, and D. M. McCormick. Ionic mechanisms underlying repetitive high-frequency burst firing in supragranular cortical neurons. *J. Neurosci.*, 20(13):4829–4843, 2000.
- [15] N. Brunel. Dynamics of sparsely connected networks of excitatory and inhibitory spiking neurons. *J. Comp. Neurosci.*, 8:183–208, 2000.
- [16] R. Butera. Multirhythmic bursting. *Chaos*, 8(1):274–284, March 1998.
- [17] R. Butera, J. Clark, C. Canavier, D. Baxter, and J. Byrne. Analysis of the effects of modulatory agents on a modeled bursting neuron: Dynamic interactions between voltage and calcium dependent systems. *J. Comp. Neurosci.*, 2:19–44, 1995.
- [18] M. Castro-Alamancos and B. Connors. Cellular mechanisms of the augmenting response: short-term plasticity in a thalamocortical pathway. *J. Neurosci.*, 16(23):7742–7756, 1996.
- [19] T. Chay and D. Cook. Endogenous bursting patterns in excitable cells. *Math. Biosci.*, 90:139–153, 1988.
- [20] G. de Vries. Multiple bifurcations in a polynomial model of bursting oscillations. *J. Nonlinear Sci.*, 8:281–316, 1998.
- [21] J. Demb, L. Haarsma, M. Freed, and P. Sterling. Functional circuitry of the retinal ganglion cell’s nonlinear receptive field. *J. Neurosci.*, 19(22):9756–9767, 1999.
- [22] E. J. Doedel. AUTO: A program for the automatic bifurcation analysis of autonomous systems. *Cong. Num.*, 30:265–284, 1981. Proc. 10th Manitoba Conf. on Num. Math. and Comp., Univ. of Manitoba, Winnipeg, Canada.
- [23] B. Ermentrout. *Simulating, Analyzing, and Animating Dynamical Systems: A Guide to XPPAUT for Researchers and Students*. SIAM, Philadelphia, 2002.
- [24] E. Evans. Auditory processing of complex sounds: An overview. *Philos. Trans. R. Soc. Lond. B Biol. Sci.*, 336(1278):295–306, 1992.

- [25] R. Fitzhugh. Impulses and physiological states in theoretical models of nerve membrane. *Biophys. Jour.*, 1:445–466, 1961.
- [26] K. Funke and F. Worgotter. On the significance of temporally structured activity in the dorsal lateral geniculate nucleus (LGN). *Prog. Neurobiol.*, 53:67–119, 1997.
- [27] W. Gerstner. Population dynamics of spiking neurons: Fast transients, asynchronous states, and locking. *Neural Computation*, 12:43–89, 2000.
- [28] W. Gerstner and J. van Hemmen. Coding and information processing in neural networks. In *Models of Neural Networks*, E. Domany, J. van Hemmen, and K. Schulten, editors, volume 2, pages 1–92. Springer-Verlag, New York, 1994.
- [29] R. Ghigliazza and P. Holmes. Minimal models of bursting neurons: How multiple currents, conductances, and timescales affect bifurcation diagrams. *SIAM J. Appl. Dyn. Sys.*, 3(4):636–670, 2004.
- [30] D. Golomb, X. Wang, and J. Rinzel. Propagation of spindle waves in a thalamic slice model. *J. Neurophysiol.*, 75(2):750–769, 1996.
- [31] C. Gray and D. McCormick. Chattering cells: Superficial pyramidal neurons contributing to the generation of synchronous oscillation in orientation columns of cat visual cortex. *Science*, 274:109–113, 1996.
- [32] R. Griffiths and M. Pernarowski. Return map characterizations of singular solutions for a model of bursting with two slow variables. *SIAM J. Appl. Math.*, 66:1917–1948, 2006.
- [33] J. Hartings, S. Temereanca, and D. Simons. High responsiveness and direction sensitivity of neurons in the rat thalamic reticular nucleus to vibrissa deflections. *J. Neurophysiol.*, 83:2791–2801, 2000.
- [34] J. He. Off responses in the auditory thalamus of the guinea pig. *J. Neurophysiol.*, 88:2377–2386, 2002.
- [35] Z. He, Y. Zhang, L. Yang, and Y. Shi. Control chaos in nonautonomous cellular neural networks using impulsive control methods. *Neural Networks, IJCNN '99. International Joint Conference on*, 1:262–267, 1999.
- [36] J. Hindmarsh and R. Rose. A model of the nerve impulse using two first order differential equations. *Nature*, 296:162–164, 1982.

- [37] J. Hindmarsh and R. Rose. A model of neuronal bursting using three coupled first order differential equations. *Proc. R. Soc. Lond. B*, 221:87–102, 1984.
- [38] J. Hindmarsh and R. Rose. A model for rebound bursting in mammalian neurons. *Philosophical Transactions: Biological Sciences*, 346(1316):129–150, 1994.
- [39] A. Hodgkin and A. Huxley. A quantitative description of membrane current and its application to conduction and excitation in nerve. *J. Physiol. (London)*, 117:500–544, 1952.
- [40] D. Hubel. *Eye, Brain, and Vision*. Scientific American Library, New York, 1995.
- [41] D. Hubel and T. Wiesel. Receptive fields of single neurones in the cat's striate cortex. *J. Physiol.*, 148:574–591, 1959.
- [42] D. Hubel and T. Wiesel. Receptive fields, binocular interaction and functional architecture in the cat's visual cortex. *J. Physiol.*, 160:106–154, 1962.
- [43] E. Izhikevich. Neural excitability, spiking and bursting. *Inter. J. of Bifurcation and Chaos*, 10:1171–1266, 2000.
- [44] E. Izhikevich, N. Desai, E. Walcott, and F. Hoppensteadt. Bursts as a unit of neural information: selective communication via resonance. *Trends in Neurosci.*, 26(3): 161–167, 2003.
- [45] J. Keener and J. Sneyd. *Mathematical Physiology*. Springer-Verlag, New York, 1998.
- [46] B. Knight. Dynamics of encoding in a population of neurons. *J. Gen. Physiol.*, 59: 734–766, 1972.
- [47] C. Koch. *Biophysics of Computation; Information Processing in Single Neurons*. Oxford University Press, New York, 2001.
- [48] H. Korn, D. Faber, and A. Triller. Probabilistic determination of synaptic strength. *J. Neurophysiol.*, 55:402–421, 1986.
- [49] R. Krahe and F. Gabbiani. Burst firing in sensory systems. *Nat. Rev. Neurosci.*, 5(1): 13–23, 2004.
- [50] A. Kriegstein and B. Connors. Cellular physiology of the turtle visual cortex: Synaptic properties and intrinsic circuitry. *J. Neurosci.*, 6(1):178–191, 1986.

- [51] S. Kuffler. Discharge patterns and functional organization of the mammalian retina. *J. Neurophysiol.*, 16(16):37–68, 1953.
- [52] W. Lytton and T. Sejnowski. Simulations of cortical pyramidal neurons synchronized by inhibitory interneurons. *J. Neurophysiol.*, 66(3):1059–1079, 1991.
- [53] A. Mallart and A. Martin. The relation between quantum content and facilitation at the neuromuscular junction of the frog. *J. Physiol.*, 196(3):593–604, 1968.
- [54] C. Morris and H. Lecar. Voltage oscillations in the barnacle giant muscle fiber. *Biophys. Jour.*, 35:193–213, 1981.
- [55] J. Nicholls, A. Martin, B. Wallace, and P. Fuchs. *From Neuron to Brain*. Sinauer Associates, Inc., Sunderland, MA, USA, fourth edition, 2001.
- [56] D. Nykamp and D. Tranchina. A population density approach that facilitates large-scale modeling of neural networks: Analysis and an application to orientation tuning. *J. Comp. Neurosci.*, 8:19–50, 2000.
- [57] A. Omurtag, B. Knight, and L. Sirovich. On the simulation of large populations of neurons. *J. Comp. Neurosci.*, 8:51–63, 2000.
- [58] H. Othmer and M. Watanabe. Resonance in excitable systems under step-function forcing I. Harmonic solutions. *Adv. in Math. Sci. Appl.*, 4(2):399–441, 1994.
- [59] M. Pernarowski. Fast subsystem bifurcations in a slowly varying Liénard system exhibiting bursting. *SIAM J. Appl. Math.*, 54(3):814–832, 1994.
- [60] M. Pernarowski. Fast and slow subsystems for a continuum model of bursting activity in the pancreatic islet. *SIAM J. Appl. Math.*, 58(5):1667–1687, 1998.
- [61] M. Pernarowski, R. Miura, and J. Kevorkian. Perturbation techniques for models of bursting electrical activity in the pancreatic β -cell. *SIAM J. Appl. Math.*, 52(6):1627–1650, 1992.
- [62] F. Pike, R. Meredith, A. Olding, and O. Paulsen. Postsynaptic bursting is essential for 'Hebbian' induction of associative long-term potentiation at excitatory synapses in rat hippocampus. *J. Physiol.*, 518(2):571–576, 1999.
- [63] R. Plant. Bifurcation and resonance in a model for bursting nerve cells. *J. Math. Biol.*, 11:15–32, 1981.

- [64] D. Purves, G. Augustine, D. Fitzpatrick, L. Katz, A. LaMantia, J. McNamara, and S. Williams, editors. *Neuroscience*. Sinauer Associates, Inc., Sunderland, MA, USA, second edition, 2001.
- [65] W. Rall. Time constants and electrotonic length of membrane cylinders and neurons. *Biophys. Jour.*, 9:1483–1508, 1969.
- [66] W. Rall. Cable theory for dendritic neurons. In *Methods in Neuronal Modeling: From Synapses to Networks*, C. Koch and I. Segev, editors, pages 9–92. MIT Press, Cambridge, MA, USA, 1989.
- [67] A. Rauch, G. La Camera, H. Lüscher, W. Senn, and S. Fusi. Neocortical pyramidal cells respond as integrate-and-fire neurons to in vivo-like input currents. *J. Neurophysiol.*, 90:1598–1612, 2003.
- [68] S. Redman. Quantal analysis of synaptic potentials in neurons of the central nervous system. *Physiol. Rev.*, 70(1):165–198, 1990.
- [69] J. Rinzel. A formal classification of bursting mechanisms in excitable systems. In *Mathematical Topics in Population Biology, Morphogenesis, and Neurosciences*, E. Teramato and M. Yamaguti, editors, volume 71 of *Lecture Notes in Biomathematics*, pages 267–281. Springer, Berlin, 1987.
- [70] J. Rinzel and Y. Lee. On different mechanisms for membrane potential bursting. In *Nonlinear Oscillations in Biology and Chemistry*, H. Othmer, editor, volume 66 of *Lecture Notes in Biomathematics*, pages 19–33. Springer-Verlag, Berlin, 1986.
- [71] J. Rinzel and Y. Lee. Dissection of a model for neuronal parabolic bursting. *J. Math. Biol.*, 25:653–675, 1987.
- [72] A. Sillito, H. Jones, G. Gerstein, and D. West. Feature-linked synchronization of thalamic relay cell firing induced by feedback from visual cortex. *Nature*, 369:479–482, 1994.
- [73] G. Smith, C. Cox, S. Sherman, and J. Rinzel. Fourier analysis of sinusoidal driven thalamocortical relay neurons and a minimal integrate-and-fire-or-burst model. *J. Neurophysiol.*, 83:588–610, 2000.
- [74] P. Smolen and J. Keizer. Slow voltage-inactivation of Ca^{2+} currents and bursting mechanisms for the mouse pancreatic β -cell. *J. Memb. Biol.*, 127:9–19, 1992.
- [75] P. Smolen, D. Terman, and J. Rinzel. Properties of a bursting model with two slow inhibitory variables. *SIAM J. Appl. Math.*, 53(3):861–892, June 1993.

- [76] M. Steriade. Synchronized activities of coupled oscillators in the cerebral cortex and thalamus at different levels of vigilance. *Cerebral Cortex*, 7:583–604, 1997.
- [77] D. Terman. Chaotic spikes arising from a model for bursting in excitable membranes. *SIAM J. Appl. Math.*, 51(5):1418–1450, 1991.
- [78] D. Terman, G. Ermentrout, and A. Yew. Propagating activity patterns in thalamic neuronal networks. *SIAM J. Appl. Math.*, 61(5):1578–1604, 2001.
- [79] J. Varela, S. Song, G. Turrigiano, and S. Nelson. Differential depression at excitatory and inhibitory synapses in visual cortex. *J. Neurosci.*, 19(11):4293–4304, 1999.
- [80] G. Wang, L. Liets, and L. Chalupa. Nitric oxide differentially modulates on and off responses of retinal ganglion cells. *J. Neurophysiol.*, 90:1304–1313, 2003.
- [81] X. Wang. Fast burst firing and short-term synaptic plasticity: A model of neocortical chattering neurons. *Neuroscience*, 89(2):347–362, 1999.
- [82] X. Wang and J. Rinzel. Oscillatory and bursting properties of neurons. In *Handbook of Brain Theory and Neuronal Networks*, M. Arbib, editor, pages 686–691. MIT Press, 1995.
- [83] M. Weliky and L. Katz. Correlational structure of spontaneous neuronal activity in the developing lateral geniculate nucleus in vivo. *Science*, 285(5427):599–604, 1999.
- [84] D. Wiesel, M. Shelley, D. McLaughlin, and R. Shapley. How simple cells are made in a nonlinear network model of the visual cortex. *J. Neurosci.*, 21(14):5203–5211, 2001.
- [85] H. Wilson and J. Cowan. Excitatory and inhibitory interactions in localized populations of model neurons. *Biophys. Jour.*, 12:1–24, 1972.
- [86] H. Wilson and J. Cowan. A mathematical theory of the functional dynamics of cortical and thalamic nervous tissue. *Kybernetik*, 13:55–80, 1973.
- [87] M. Xie, H. Othmer, and M. Watanabe. Resonance in excitable systems under step-function forcing II. Subharmonic solutions and persistence. *Physica D*, 98:75–110, 1996.